UNIVERSITY OF
GOTHENBURG

Thesis for the degree of doctor of philosophy

Multi-Electron and Multi-Ion Coincidence Spectroscopy of Single-Photon Ionization Processes in Molecules

Author:
Andreas Hult Roos

Main supervisor:
Prof. Raimund Feifel

Examiner:
Prof. Ann-Marie Pendrill

Opponent:
Prof. Eleanor Campbell

University of Gothenburg
Department of Physics

Doctoral Dissertation in Physics

Department of Physics
University of Gothenburg
412 96 Gothenburg, Sweden

April 29, 2019

ISBN: 978-91-7833-486-5 (printed)
ISBN: 978-91-7833-487-2 (pdf online)
URL: http://hdl.handle.net/2077/59861

Cover: Illustration of a three dimensional coincidence map created from krypton data measured at a photon energy of 110 eV. The intensity of the peaks is on a logarithmic scale, for better visualization of the weaker structures in the map.

Printed by BrandFactory, Kållered, 2019

Typseted using LaTeX

Multi-Electron and Multi-Ion Coincidence Spectroscopy of Single-Photon Ionization Processes in Molecules

Abstract

This thesis presents experimental investigations of multi-electron and multi-electron-multi-ion coincidence measurements of samples in the gas phase utilizing a versatile time-of-flight magnetic bottle spectrometer technique. These investigations of multiply ionized atomic and molecular species provide valuable information on, and understanding of, ionization processes and dissociation mechanisms highly relevant to the development of electronic structure theories.

Paper I investigated the double valence photoionization spectra of methyl halides. From this study, the lowest onset and vertical double ionization energies were obtained for CH_3F, CH_3Cl, and CH_3I, and used to test an empirical rule-of-thumb for the double ionization of molecules. The study concluded that the apparent inter-charge distance may be derived by applying the rule-of-thumb on molecules similar to the methyl halide structure group.

Paper II studied the dissociation of D_2O by photoelectron-photoion coincidence measurements. The experiments yielded ion mass-selected photoionization spectra, and dissociation breakdown diagrams, with improved statistics than previous studies of this kind. Minor fragments were detected and modulations in the yield of the fragments were observed of the B^2B_2 state, with the implication that the fragmented system retains memory of the vibrational structure before the dissociation pathway is irreversibly chosen. Measurements of the C^2A_1 state revealed high kinetic energy OD^+ fragments.

Paper III concerned the dissociation mechanisms of ICN upon core site-, and orbital-specific photoionization. The weights of the multiply charged fragmentation channels were obtained from the decay of initial core vacancies, and partial Auger spectra were obtained in coincidence with the doubly charged final products, which revealed the relative extent of the different fragmentation channels in the complete single Auger spectrum of ICN.

Papers IV and V investigated the relative abundance of double Auger decay in molecules upon core vacancy formation. The quantity of double compared to single Auger decay was found to surpass 20% in some of the heavier molecules, which is a significant amount and undoubtedly contradicts the past assumption that such processes are negligible. The amount of double Auger decay follows a linear trend with the number of available valence electrons on the nearest neighbouring atoms. It was also found that the 1s or 2p nature of the initial core vacancy had no significant effect on the amount of double Auger decay. The investigation of multiple Auger decay was expanded in Paper VI towards the amount of triple Auger decay in CO and CO_2. The quantity of triple compared to single Auger decay in CO and CO_2 upon an initial C 1s core vacancy was determined as 0.82% and 1.44%, respectively, and upon an O 1s vacancy as 0.89% and 1.0%, respectively. The percentage of triple Auger decay also follows a linear trend related to the number of available valence electrons.

Populärvetenskaplig sammanfattning

Denna avhandling handlar om atom- och molekylfysik, som mer specifikt kan beskrivas som interaktionen mellan elektronerna inne i atomer och molekyler. Denna interaktion bestämmer de fysikaliska och kemiska egenskaper som atomerna och molekylerna besitter. Exempel på dessa egenskaper kan vara hur de interagerar med infallande ljus eller vid kontakt med andra atomer och molekyler. Studier inom detta område bidrar med värdefull information som kan ligga till grund för, och stimulera, framtida teoretiska och experimentella studier av atomära och molekylära system.

Ljus betraktas inom fysiken som en elektromagnetisk våg som breder ut sig i tid och rum, och bär med sig energi i form av frekvensen med vilken vågen svänger. Den elektromagnetiska vågen har vanligtvis olika benämningar beroende på hur mycket energi som den bär på. Det elektromagnetiska spektrumet av energier går från låg energetiska radiovågor och mikrovågor, till infrarött och ultraviolett ljus, och sedan till högenergetisk röntgen- och gammastrålning. Det korta spannet av det synliga ljusets spektrum ligger mellan det infraröda och ultravioletta ljuset. Ljus kan interagera med de några av de minsta byggstenarna i materian runt omkring oss, som atomer och molekyler, vilket kan användas för att studera och öka kunskapen om materian. I den enklaste bilden av en atom, består den av negativt laddade elektroner som cirkulerar i bundna banor runt en positivt laddad kärna. Molekyler är i sin tur uppbyggda av flera atomer bundna till varandra genom att dela på de elektroner som cirkulerar runt atomernas kärnor.

Idag är interaktionen mellan ljus och materian runt omkring oss av stort intresse eftersom den används både vardagligt och inom många forskningsfält. Men anledningen till att vi idag kan undersöka denna interaktion är tack vare de banbrytande fysikerna som började studera detta fenomen i slutet av 1800-talet och början av 1900-talet. En av de första experimentella observationerna av interaktionen mellan ljus och materia gjordes år 1887 av den tyska fysikern Heinrich Hertz, när han genererade gnistor mellan elektroder genom att belysa dem med ultraviolett ljus. För att kunna förklara vissa fysikaliska processer föreslog fysikern Max Planck, år 1900, att ljus har karaktären av små energipaket, vilket kan räknas som den moderna fysikens födelsedag. Denna idé blev år 1905 konkretiserad när en ung forskare vid namn Albert Einstein publicerade sitt arbete, där han antog att elektromagnetisk strålning består av diskreta små kvantiserade paket av energi, idag kända som fotoner. Detta arbete förklarade i detalj hur ljus interagerar med materia, vilket förklarade Hertz observation av den *fotoelektriska effekten*. Arbetet öppnade också upp för bilden av

våg-partikel-dualiteten, där ljus betraktas som både vågor och partiklar, vilket Louis de Broglie föreslog år 1924 i sin doktorsavhandling. Alla de fysiker som arbetade med interaktionen mellan ljus och materia under början av 1900-talet inspirerade efterföljande generationer av fysiker och banade vägen för det breda och, i modern tid, väldigt framgångsrika kvantfysikaliska forskningsfältet. Kvantfysiken bygger på att några av de minsta objekten i vår värld, som elektroner och atomer, enbart kan anta specifika ("kvantiserade") energivärden. Detta är i motsatts till den vardagliga bilden av objekten runt omkring oss.

Elektroner inne i molekyler (och atomer) är bundna med specifika kvantiserade bindningsenergier beroende på bland annat hur nära de är atomens kärna. En elektron i en molekyl kan frigöras från sitt bundna tillstånd, via den fotoelektriska effekten, vilket lämnar molekylen i ett joniserat tillstånd med ett överskott av en positiv laddning (som en positiv jon). Elektronen som lämnar molekylen får då en viss rörelseenergi motsvarande energin på den infallande fotonen minus elektronens bindningsenergi. Genom att mäta rörelseenergin på elektronen går det därmed att ta reda på var ifrån i molekylen som den var frigjord. Experimentella metoder för att studera spektra, som till exempel elektroners energi, går vanligtvis under samlingsnamnet *spektroskopi*.

Under 1800- och 1900-talet utvecklades spektroskopi till ett mycket starkt och framgångsrikt forskningsfält i Sverige av internationellt välmeriterade forskare som Anders Jonas Ångström, Johannes "Janne" Rydberg, Manne Siegbahn, och Kai Siegbahn. De två sistnämnda fysikerna var med och lade grunden för och utvecklade röntgenfluorescens- respektive fotoelektron-spektroskopin, för viket de erhöll varsitt Nobelpris i fysik. Idag är i synnerhet fotoelektronspektroskopin ett stort forskningsfält vilket används inom fysiken, kemin, och biologin för att studera dynamiska processer och strukturer av materia i alla dess förekommande former.

Upptäckten av den fotoelektriska effekten banade väg för elektronspektroskopi som forskningsfält för studier av bland annat materien runt omkring oss vilket ger viktiga kunskaper om fysikaliska och kemiska fenomen. Fotoelektriska effekten förklarar hur elektroner bundna i atomer och molekyler kan frigöras om de får ett tillskott av energi från en infallande foton. När elektronen lämnar sitt bundna tillstånd tar den med sig information om vad som hände inne i atomen eller molekylen. För att en elektron ska lämna ett bundet tillstånd inne i en atom eller molekyl behöver den absorbera en foton inom spektrumet för ultraviolett ljus eller röntgenstrålning, vilken har tillräckligt mycket energi för att elektronen ska övervinna den attraherande kraften från kärnan i atomen.

Denna avhandling bygger på fotoelektronspektroskopin som mätmetod för att studera hur flera elektroner korrelerar i molekyler som befinner sig i gasfas. Elektroner som frigörs samtidigt från ett atomärt eller molekylärt system, efter inverkan av en foton, kommer att vara korrelerade med varandra. Genom att studera de frigjorda elektronerna kan viktig information om systemet erhållas, och bidra till att bygga upp en mer fullständig bild av fysiken och kemin. För att kunna studera flera elektroner samtidigt krävs så kallade korrelationsexperiment.

En mycket effektiv metod för korrelationsspektroskopi utvecklades av professor John H. D. Eland från universitetet i Oxford, som har varit en nära samarbetspartner till studierna i denna avhandling. Professor Eland är välkänd för utvecklingen

av experimentella metoder för att studera korrelerade joner och elektroner i form av så kallade flygtids- (“time-of-flight”) mätningar. Dessa experimentella metoder baseras på mätningar av tiden det tar för skapade joner eller frigjorda elektroner att flyga en sträcka av några meter i vakuum genom ett rör. Genom att mäta tiden det tar för jonerna eller elektronerna att färdas genom röret går det att beräkna deras rörelseenergi. I denna spektrometer fångas de frigjorda elektronerna upp av ett magnetfält format som halsen på en flaska (det går från ett smalt till ett mer utbrett magnetfält), vilket ger denna typ av spektrometer dess namn “magnetisk-flaskspektrometer”. Magnetfältet guidar elektronerna genom röret till en detektor som mäter flygtiden på alla frigjorda elektroner.

Eftersom elektronerna skapar de bindande krafterna mellan atomerna i en molekyl, kan en molekyl “förstöras” eller fragmenteras om en eller fler av elektronerna avlägsnas från sina banor inne i molekylen. Genom att mäta flygtiden på alla frigjorda elektroner och joner samtidigt går det att korrelera dem till specifika processer som avslöjar fysiken inne i atomernas och molekylernas kvantvärld. Denna helhetsbild av atomer eller molekyler kan sedan användas inom andra forskningsfält, som till exempel atmosfärsfysik och astrofysik, där ljus av hög energi vanligen infaller på molekyler.

Denna avhandling fokuserar på att förstå de olika processer som leder till fragmentering av olika molekyler, och till vilken utsträckning en molekyl fragmenterar efter att ha absorberat en foton med en viss mängd energi. Inom ramen av denna avhandling har en ny version av en tvådelad elektron- och jonspektrometer utvecklats för korrelationsmätningar på de joner och elektroner som frigörs i en fragmenteringsprocess. Med denna nya elektron-jon-spektrometer och en tidigare version har fragmenteringsstudier på bland annat tungt vatten (D_2O) och jodcyanid (ICN) utförts. Mätningarna på D_2O gav spektra med bättre precision än föregående studier, vilket gjorde det möjligt att observera att de enkeljoniserade fragmenten av D_2O har kvar ett slags “minne” av hur molekylen vibrerade före dess fragmentering. I den andra studien på fragmenteringen av jodcyanid, vilket är en molekyl som består av en jod, en kol och en kväve atom, fokuserade vi på beskrivningen av hur molekylen fragmenterar beroende på från vilken atom och hur långt in i atomen som en elektron frigörs från molekylen.

Det mest omfattande arbetet i denna avhandling berör så kallade *Auger sönderfall*, vilket är en specifik jonisationsprocess där elektroner interagerar med varandra genom att de byter mellan olika banor inne i en atom eller molekyl. Dessa byten frigör energi som en annan elektron sedan kan ta upp, i form av bland annat rörelseenergi, och därmed frigöras från sin egen bana. Denna process lämnar atomen eller molekylen i ett flerfaldigt joniserat tillstånd, med flera frigjorda korrelerade elektroner. I denna avhandling studerades mängden Auger sönderfall som skapas i olika molekyler efter att en första elektron fotojoniseras från banor djupt inne i molekylerna. Studien visade att mängden Auger elektroner som frigörs i vissa fall är mycket högre än vad som har antagits vara fallet i tidigare studier. Baserat på mätningarna togs en empirisk formel fram för att kunna uppskatta mängden Auger sönderfall i molekyler.

Studierna i denna avhandling bidrar med värdefull information inom området för atom- och molekylfysik. Arbetena som har utförts kan ligga till grund för och stimulera framtida teoretiska och experimentella studier av Auger sönderfall och fragmenteringar av molekylära system.

List of Papers

List of papers included in this thesis:

I Valence double ionization electron spectra of CH_3F, CH_3Cl and CH_3I
A. Hult Roos, J. H. D. Eland, D. Koulentianos, R. J. Squibb, L. Karlsson, and R. Feifel
Chemical Physics **491**, 42-47 (2017).
My contributions: Conducted the measurements, data analysis, and wrote the majority of the manuscript.

II Dissociations of water ions after valence and inner-valence ionization
A. Hult Roos, J. H. D. Eland, J. Andersson, R. J. Squibb, and R. Feifel
The Journal of Chemical Physics **149**, 204307 (2018).
My Contributions: Conducted the measurements, some of the data analysis, and wrote parts of the manuscript.

III Dissociation of multiply charged ICN by Coulomb explosion
J. H. D. Eland, R. Singh, J. D. Pickering, C. S. Slater, A. Hult Roos, J. Andersson, S. Zagorodskikh, R. J. Squibb, M. Brouard, and R. Feifel
The Journal of Chemical Physics **145**, 074303 (2016).
My contributions: Instrument development, conducted the measurements, and contributed to the manuscript.

IV Relative extent of double and single Auger decay in molecules containing C, N and O atoms
A. Hult Roos, J. H. D. Eland, J. Andersson, S. Zagorodskikh, R. Singh, R. J. Squibb, and R. Feifel
Physical Chemistry Chemical Physics **18**, 25705-25710 (2016).
My contributions: Conducted the measurements, data analysis, and wrote the majority of the manuscript.

V Abundance of molecular triple ionization by double Auger decay
A. Hult Roos, J. H. D. Eland, J. Andersson, R. J. Squibb, D. Koulentianos, O. Talaee, and R. Feifel
Scientific Reports **8**, 16405 (2018).
My contributions: Project planning, conducted the measurements, data analysis, and wrote the majority of the manuscript.

VI Relative extent of triple Auger decay in CO and CO_2
A. Hult Roos, J. H. D. Eland, J. Andersson, M. Wallner, R. J. Squibb, and R. Feifel
Physical Chemistry Chemical Physics, Accepted 16 April, 2019,
DOI: 10.1039/C9CP01415B.
My contributions: Project planning, conducted the measurements, data analysis, and wrote the majority of the manuscript.

List of papers related to, but not included in this thesis:

- **Ion charge-resolved branching in decay of inner shell holes in Xe up to 1200 eV**
  J. H. D. Eland, C. Slater, S. Zagorodskikh, R. Singh, J. Andersson, A. Hult-Roos, A. Lauer, R. J. Squibb, and R. Feifel
  Journal of Physics B: Atomic, Molecular and Optical Physics **48**, 205001 (2015).

- **Auger decay of $4d$ inner-shell holes in atomic Hg leading to triple ionization**
  J. Andersson, R. Beerwerth, A. Hult Roos, R. J. Squibb, R. Singh, S. Zagorodskikh, O. Talaee, D. Koulentianos, J. H. D. Eland, S. Fritzsche, and R. Feifel
  Physical Review A **96**, 012505 (2017).

- **Energy sharing distributions in direct double photoionization of He**
  J. Andersson, S. Zagorodskikh, A. Hult Roos, O. Talaee, R. J. Squibb, D. Koulentianos, M. Wallner, V. Zhaunerchyk, R. Singh, J. H. D. Eland, J. M. Rost, and R. Feifel
  Submitted to Scientific Reports (2019).

- **Coulomb explosion of CD_3I induced by single photon deep inner-shell ionisation**
  M. Wallner, J.H.D. Eland, R.J. Squibb, J. Andersson, A. Hult Roos, R. Singh, O. Talaee, D. Koulentianos, M.N. Piancastelli, M. Simon, and R. Feifel
  In manuscript.

- **Formation and relaxation of K^{-2} and $K^{-2}V$ double-core-hole states in C_4H_{10}**
  D. Koulentianos, R. Couto, J. Andersson, A. Hult Roos, R. J. Squibb, M. Wallner, J. H. D. Eland, M. N. Piancastelli, M. Simon, H. Ågren, and R. Feifel
  In manuscript.

Contents

Wish you were here

Chapter 1

Introduction

Physics models electromagnetic radiation as a wave that propagates through time and space, carrying energy in a spectrum raging from low energy radio waves up to highly energetic gamma rays, with visible light in the intermediate region. The interaction between electromagnetic radiation and matter is of considerable interest in almost every research field in the natural sciences, and was first experimentally observed by the physicist Heinrich Hertz in 1887 [1], when he generated electrical sparks by illuminating electrodes with ultraviolet light. Around 1900, Max Planck suggested that the nature of the energy in electromagnetic radiation is carried in form of small "packages". This idea was later advanced, in 1905, when Albert Einstein published his paper [2] on the hypothesis that electromagnetic radiation consists of discrete quantized energy packets, today known as photons, as part of his explanation of the photoelectric effect observed by Heinrich Hertz. This opened up the view that light can both be seen as waves and as particles, i.e. as a wave-particle duality that was later proposed by Louis de Broglie [3].

This thesis will focus on the light-matter interaction of ultraviolet and X-ray radiation with atoms and molecules, in the framework of multi-electron photoionization. Photoionization is the emission of an electron from atoms or molecules upon irradiation of electromagnetic radiation of sufficient energy to overcome the energy by which the electron is bound to the system. *Multi-electron* implies the involvement of more than one electron in the excitation or ionization mechanisms. The progression of these mechanisms, which often includes intermediate processes, is one of the foci of this thesis. Photoionization studies of atoms and molecules can reveal their chemical and bonding properties, and thus have direct relevance to many research fields in physics, chemistry and biology. The importance of studies on multi-ionization processes of electrons from their bond states is that they reveal electron-electron correlation mechanisms and information concerning the ionization processes leading to multiply charged ions. In nature, multiply charged ions are commonly created under conditions where of highly energetic photons or other particles are present, e.g. in the ionosphere and outer atmosphere of Earth, in astrophysical contexts, and in plasma physics. Experimental studies of processes where multiply charged ions are formed, theoretical atomic and molecular models can be tested and developed further.

In this thesis, the method of electron coincidence spectroscopy on molecules is utilized to study multielectron processes in molecules upon absorption of a single photon. The investigations involve the removal of electrons from deeply bound core

shells, close to the atomic nucleus, and more weakly bond electrons in the valence region. For studies of electrons over this large energy range, a magnetic bottle time-of-flight spectrometer has been used. This type of spectrometer is well suited for studies of this type, where a large amount of correlated and uncorrelated processes may take place during an ionization event.

In the remainder of this chapter, the basic theory of atoms and molecules will be recapitulated, and in the second chapter the relevant possible processes that may occur upon the absorption of a single photon initiating an ionization event in atoms and molecules will be presented. In chapters three and four, the experimental techniques and data analysis methods used in this thesis will be described as a background for understanding the results which are presented in chapter five. Lastly, the main conclusions and possible future directions of this research are discussed in the final chapter of this thesis.

1.1 Atoms

Every solid object, body of liquid, and gas around us is comprised of atoms, which are the smallest entity of every chemical element. The idea of discrete units of matter and the name, atom, may be traced back to the ancient Greeks, which originated the word "atomo" (Greek: ἄτομο), meaning "uncuttable". They had the idea that all objects are built from atoms which are the fundamental building blocks in nature, something that we today know is true. The atoms themselves consist of even smaller particles; negatively charged electrons and a compact nucleus of positive protons and neutral neutrons. The atomic structure has been modelled in many ways throughout the history of science, based on experimental observations.

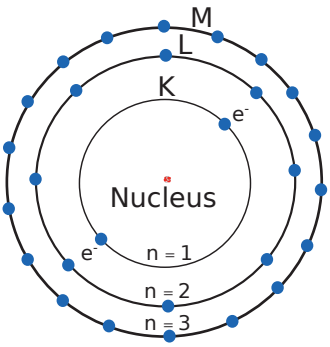

Figure 1.1: The Bohr atomic model with the shell-like electronic structure. The electrons, represented by blue dots, are confined to stable orbits around a nucleus comprised of protons and neutrons.

At the beginning of the 20th century Niels Bohr developed a model from experimental observations revealing that an atom can only radiate light with discrete, distinct energies. This model is in the present day called the Bohr model, and is

built on the postulate that the electron revolves around the nucleus at discrete distances in stable orbits, without radiating any energy. The model predicts that the radius of the stationary orbitals that an electron is confined to in the atom is given by the classical angular momentum of the electron as an integer multiple, n, of the reduced Planck's constant, $\hbar = h/2\pi$. The angular momentum can be described according to the formula $\mathrm{m_e}vr = n\hbar$, where $\mathrm{m_e}$ is the electron mass and v the speed of the electron at a distance r from the nucleus. In quantum mechanics, n is the principal quantum number and can hold the values $n = 1, 2, 3, ...$, where $n = 1$ denotes the orbit closest to the nucleus. In this model the electrons are confined to the atom according to a shell-like structure. Historically, each shell is labelled with letters corresponding to the values of the principal quantum number

n	=	1	2	3	4	$\cdots$
		K	L	M	N	$\cdots$

This notation and the general structure according to the Bohr model is illustrated in Fig. 1.1. The closer an electron is to the nucleus, the stronger the electromagnetic force from the positively charged nucleus acts upon it, and therefore the more strongly it is bond to the atom. An electron that moves around the nucleus in a circular motion will have angular momentum that is related to the radius of its motion within the shell, and therefore also to the specific principal quantum number of the shell. The orbital angular momentum of an electron is described by the azimuthal quantum number, l, which may take the values $l = 0,\ 1,\ 2,\ 3,\ n-1, \cdots$ and follows the notation

l	=	0	1	2	3	$\cdots$
		s	p	d	f	$\cdots$

Electrons within a shell with the principal quantum number n may have l quantum numbers in the range $0 \leq l \leq n - 1$ in integer steps, which are individually sometimes referred to as the sub-shells or orbitals. The n and l quantum numbers together describe the basic shape of the electron orbit around the nucleus. An electron within a specific sub-shell will have its "movement" spread over the shape of the sub-shell, where the direction of the electron's movement is directed within the sub-shell. The direction is described by the magnetic quantum number, m_l, which may take values of $m_l = -l, \cdots, 0\ , \cdots,\ l$ in integer steps.

In the modern picture of quantum mechanics, the electrons are considered to be confined to an atom as standing waves extending over the quantized set of discrete orbitals around the nucleus. This means that the electrons within an orbital can be conceptualized as electron clouds, where the density of the electron cloud defines the probability that an electron appears at a particular position within the orbital

at the time of measurement. This atomic model is illustrated in Fig. 1.2, for an atomic orbital with the quantum number $n = 0$ (and therefore $l = 0$). The shape and orientation of the orbital that an electron cloud is confined to depends on the quantum numbers n, l, and m_l, which can range from spherical and elongated to more exotic shapes.

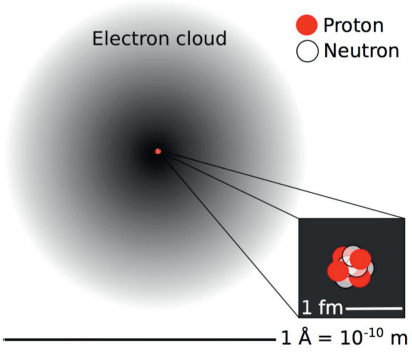

Figure 1.2: Illustration of an s-orbital ($n = 0$) according to quantum mechanics. The electrons within this orbital can be visualized as clouds, with a higher electron density closer to the nucleus.

An electron in an atomic orbital can be described by a unique set of the n, l, and m_l quantum numbers, given from the solution of the *Schrödinger equation*. The Schrödinger equation can be expressed as $\hat{H}\psi(\vec{r}) = E\psi(\vec{r})$, where $\hat{H}$ is the Hamiltonian that defines the set of possible energy eigenstates of the electron in the system. The Hamiltonian can be seen as the sum of the kinetic, $\hat{T}$, and potential, $\hat{V}$, energy operators corresponding to the total energy of the system. In the picture of the Schrödinger equation, the electron is described as a wave, which is confined to an atomic shell, with a wavefunction $\psi(\vec{r})$ that depends on the radial position $\vec{r}$ relative to the nucleus. The Hamiltonian of an electron in three dimensional space is of the form

$$\hat{H} = \hat{T} + \hat{V} = -\frac{\hbar^2}{2\mu}\nabla^2 + V(\vec{r}) \quad , \tag{1.1}$$

where ∇^2 is the Laplacian operator and μ is the reduced mass of the electron and nucleus, thus working in the centre-of-mass of the system. By inserting this expression into the Schrödinger equation one gets

$$\left(-\frac{\hbar^2}{2\mu}\nabla^2 + V(\vec{r})\right)\psi(\vec{r}) = E\psi(\vec{r}) \quad . \tag{1.2}$$

The Schrödinger equation can only be solved exactly for the simplest case of one electron systems, like the hydrogen atom and hydrogen-like ions, i.e. two-body systems. For larger systems, including three-body systems and larger, the Schrödinger equation cannot be solved exactly. Instead it has to be solved by approximative methods. The complexity of the Schrödinger equation for systems where several

electrons are present can be understood from the fact that the electrons within a system will interact via the Coulomb force, which means that the electrons cannot be treated as completely separate entities any more.

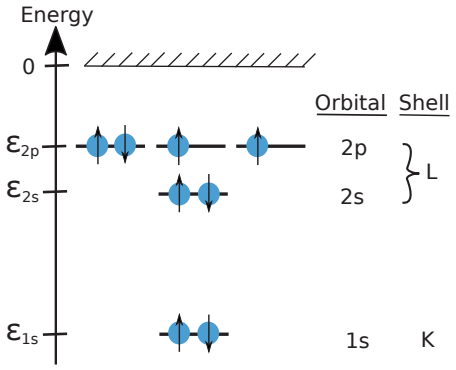

Figure 1.3: Atomic energy levels of an atom containing 8 electrons arranged in the 1s, 2s, and 2p orbitals.

Electrons are also described by an intrinsic property that can be described as an intrinsic angular momentum, which is parametrized by a fourth quantum number s called the spin. The spin quantum number has the value $s = 1/2$, which can have two states, or directions relative to a well defined axis, described by $m_s = \pm 1/2$ or commonly by $\uparrow$ and $\downarrow$ for each respective state. Every electron within an atomic system can be described by a unique set of the four quantum numbers, which means that every atomic sub-shell can be occupied by two electrons with opposite spin states, respectively. This can be seen in Fig. 1.3 where the energy of several shells for specific quantum numbers n, l, and m_l are obtained from the Schrödinger equation. The orbital (or sub-shell) energies are usually defined on the negative scale, and are usually indicated with the n and l quantum numbers as nl, which can be seen from Fig. 1.3.

1.2 Molecules

Two or more atoms may start forming molecular bonds by sharing electrons between them in the form of a covalent bond. This can be understood as the electron density in between the atoms becoming larger as the electron clouds start to overlap, which is illustrated in Fig. 1.4 for the H_2 molecule. In this figure, the darker region in between the two hydrogen atoms indicates a higher electron density that will attract the positively charged nuclei. Because of the complexity required to precisely describe these many-particle systems, approximations are used for the description of molecular systems. One of the most straight forward and intuitive method to describe molecular orbitals is the linear combination of atomic orbitals (LCAO) [4], where the molecular orbitals are described based on atomic wavefunctions. Consider

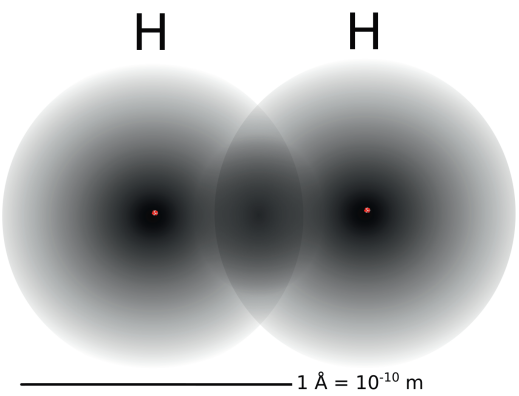

Figure 1.4: Illustration of the bond formation of a hydrogen molecule.

the example of a diatomic molecule AB formed by the atoms A and B, with wavefunctions Ψ_A and Ψ_B, respectively. Within LCAO theory the molecular wavefunction is described by

$$\Psi_{\pm} = C_1\Psi_A \pm C_2\Psi_B \quad , \tag{1.3}$$

where C_1 and C_2 are constants. The + and − signs indicate constructive and destructive interference, respectively, between the atomic wavefunctions. The constructive interference will lead to an increased electron density and will therefore contribute to the formation of molecular bonding orbitals. In contrast, destructive interference will lead to a reduced electron density, which indicates the formation of molecular anti-bonding orbitals.

In the example of the hydrogen molecule, the electrons that form the bond are shared between the two hydrogen atoms, which means that they are free to move in between the atoms and are therefore said to be delocalized over a molecular orbital. The atomic valence (outermost) orbitals are therefore those primarily involved in the formation of the molecular bonds. Atomic orbitals that are not (or very weakly) involved in the molecular bond formation are more localized to the atomic nucleus, which is the case for the deeper core orbitals, which retain much of their atomic-like character. Molecules vibrate and rotate at quantized energy modes by changing the interatomic distance(s), which will add to the energy of the molecular orbitals. Electronic states in molecules may therefore comprise several vibrational and rotational energy levels at energy separations that are much smaller compared to the separations between the orbital energy levels.

The specific approximations and assumptions that are required for molecular quantum mechanical methods do not always produce satisfactory results when compared to the real world, especially for the increased complexity for larger molecular systems. Experimental investigations are therefore of great importance for testing existing models and developing new theoretical models, by providing detailed experimental data of molecular and electronic processes and dynamics by which the multitude of quantum chemical models may be tested and evaluated.

Chapter 2

Electronic processes

An atom or a molecule is normally in a stable state, unless perturbed by an external source, be it an external field or interaction with another particle. While changes to the nuclear motion may require only small amounts of energy, electron perturbations generally require much larger energies. Sufficiently large energy changes may allow electronic transitions between different atomic or molecular states, for example changes of the orbital occupancy in an excitation process, or the removal of one or more electrons from the system into the *continuum* in an ionization process.

This thesis will mainly focus on studies where a single photon of relatively large energy interacts with the electrons in an atomic or molecular system resulting in an ionization event. When a photon is absorbed by an atom or molecule, the system will have an excess of energy that needs to be dissipated. The energy can be transferred to one or several electrons which may gain enough energy to leave the system in an ionization process. The whole process of photon absorption and emission of the electron(s) is a quantum mechanical process that can be seen as a single dynamic process which leaves the system in an energetically excited state. This excited state may then deexcite by processes that will emit additional electrons into the continuum. This thesis will focus, from an experimental perspective, on processes where multiple electrons are emitted upon single-photon absorption.

2.1 Photoionization

The ionization energy, also referred to as ionization potential (IP) or binding energy [5], of an electron is the energy required in order for an electron to overcome the attractive force binding it to an atomic or molecular system. The outermost electrons, i.e. the valence electrons, are the least bound and therefore the easiest to remove, while electrons closer to the nucleus, i.e. core electrons, are more tightly bound, requiring a higher energy to be liberated. The simplest case of ionization is when a single photon transfers its energy to a single electron, resulting in a single ionization event that can be understood from the energy relation

$$\mathrm{E_A} + \mathrm{h}\nu = \mathrm{E_{A^+}} + \varepsilon \quad , \tag{2.1}$$

where $\mathrm{E_A}$ and $\mathrm{E_{A^+}}$ are the total energies of the neutral and singly ionized (cationic) systems, the energy of the photon is given by $\mathrm{h}\nu$, and ε is the kinetic energy of the emitted electron. By slightly rewriting this relation, and remembering that $\mathrm{E_A}$ and

E_{A^+} are usually defined on the negative scale, it is possible to see that the IP of the electron is the energy difference that is required to promote the system from its neutral state to the ionic state

$$\varepsilon = h\nu - (E_{A^+} - E_A) = h\nu - IP \quad . \tag{2.2}$$

The process of single-photon single electron ionization is illustrated in Fig. 2.1 (a). In this figure it is assumed that the energy of the photon is transferred to only one electron in the system. However, the energy may be shared between multiple electrons in the system, resulting in, for example, photoionization of one electron and excitation of a second electron to an unoccupied orbital. The result of this is the formation of what is often referred to as a satellite state. In this process, the satellite electron will gain a particular amount of energy corresponding to the energy difference between its parent orbital and the orbital that it is excited to, which according to conservation of energy means that the liberated electron will obtain a smaller portion of the photon energy compared to pure single ionization. It is worth noting here that the kinetic energy of an emitted electron is not equal to the photon energy minus the orbital energy of the electron. When an electron is ionized from an atomic or molecular orbital, the remaining orbitals will go through relaxation to the new cationic state, simultaneously as the emitted electron is leaving the system, requiring an amount of energy for the redistribution of the remaining electrons.

An excited atomic or molecular system may deexcite by emission of either a photon by fluorescence, or an electron from one of the outer valence-shells in a so called *autoionization* process. The fluorescence mechanism will not be further discussed in this thesis because of its low probability in lower mass atoms [7], which makes it a minor competing process [6] relative to the other relaxation pathways that will be discussed. States that may autoionize are energetically above the ionization limit and are therefore usually very short lived excited states [6]. The *Auger decay*, on which papers IV, V, and VI are based, is a type of autoionization process where a highly excited core state decays. The Auger decay mechanism will be discussed in more detail in section 2.2.2.

A single-electron photoionization spectrum can be presented as a histogram of the binding energies of the electrons to the atoms or molecules in the system, and is a powerful tool providing a probe into the electronic structure of atoms and molecules. Spectra of atomic-like orbitals are usually sharp peaks, due to their discrete nature and well defined energy levels of the orbitals. Ionization spectra involving molecular valence orbitals are usually more complicated because of close lying vibrational energy levels as well as possible dissociation processes (see section 2.3) after the removal of an electron from a binding orbital. Core orbitals in molecules can be assumed to be localized within the molecule retaining essentially their atomic character, and are not involved (or have very little involvement) in the formation of molecular orbitals, typically giving rise to single peaks in the photoelectron spectrum.

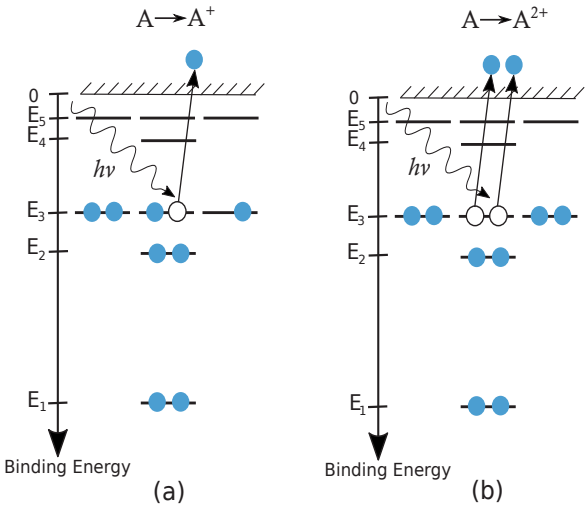

Figure 2.1: Illustration of the (a) single and (b) double (valence) ionization processes.

2.2 Multi-electron ionization

The removal of two or more electrons from a sample atom or molecule is commonly referred to as multi-electron ionization. The most simple case of multi-electron ionization, that requires the least amount of energy, is the double ionization of valence electrons, which is illustrated in Fig. 2.1 (b). The amount of energy that is required to remove two electrons from an atom or molecule is often referred to as the double ionization potential (DIP), which is equivalent to the energy formula

$$\mathrm{E_A} + \mathrm{h}\nu = \mathrm{E_{A^{2+}}} + \varepsilon_1 + \varepsilon_2 \quad , \tag{2.3}$$

where ε_1 and ε_2 are the kinetic energy of the fastest and slowest emitted electrons, respectively, and $\mathrm{E_{A^{2+}}}$ is the energy of the doubly ionized product (dication). The DIP is therefore equal to the photon energy minus the sum of the kinetic energy of the electron pair, i.e. $\mathrm{h}\nu - (\varepsilon_1 + \varepsilon_2)$, and equivalent relations for higher order multi-electron ionization processes.

The minimum amount of energy required to remove two electrons from the outermost valence orbital, i.e. the lowest DIP, in atomic samples can be estimated by an empirical rule-of-thumb [8] that states that the lowest DIP is approximately equal to $\mathrm{E_{DIP}} = 2.8 \cdot \mathrm{E_{IP}}$, where $\mathrm{E_{IP}}$ is the lowest single ionization potential. This formula provides surprisingly good agreement with many experimentally known ionization potentials of many atoms [8], and may be very useful in preparation of experimental measurements where the lowest DIP is unknown but the single IP is well known from previous measurements. A similar empirical formula can be expressed for the energetically lowest DIP in molecules [9], by taking into account the de-localization of the valence electrons over the molecule. Because of the de-localized valence orbitals,

the Coulomb interaction between the two charges in the vacancies created from the double ionization process has to be taken into account, due to the possibility for a wider charge separation in the final dicationic molecular product. According to Molloy et al., the empirical formula for the lowest DIP in molecules is given by

$$\mathrm{E_{DIP}} \approx 2.2 \cdot \mathrm{E_{IP}} + \frac{11.5}{r_{\mathrm{hh}}} \quad , \tag{2.4}$$

where the additional term, $11.5/r_{\mathrm{hh}}$, stems from the Coulomb interaction between two vacancies separated by the interatomic distance r_{hh} (in Å) in the molecular valence orbitals. The parameter 11.5 was found empirically by a fit of data from several relatively small molecules [9]. Formula 2.4 provides satisfactory agreement for experimental measurements of the lowest DIP in diatomic linear, non-linear polyatomic and some cyclic molecules based on the assumption that the charges are separated as far apart as possible within the molecular structure [9].

2.2.1 Knock-out and shake-off

The process of multi-electron ionization by a single photon can be discussed as a *direct process* with two leading mechanisms, i.e. the *knock-out* (KO) and the *shake-off* (SO) mechanism [10]. A direct process in an ionization event can be defined as a non-stepwise process where the kinetic energies of the emitted electrons have a direct linear correlation to a total amount of energy, e.g. $\mathrm{E_{tot}} = \varepsilon_1 + \varepsilon_2$ in the case of direct double ionization, where E_{tot} is the total available kinetic energy for the electron pair.

The KO and SO mechanisms can be understood from the total transition amplitude, $a_{f,i}$, formulated by Pattard et al. [11], for direct double ionization between an initial and a final state

$$a_{f,i} \propto \langle \psi_f | (1 - i \int_0^\infty e^{i\mathrm{H}_0 t}\ \mathrm{T_{ee}}\ e^{-i\mathrm{H}_0 t}\ dt) \mathrm{V_{pe}} | \psi_i \rangle \quad , \tag{2.5}$$

where H_0 is the final state Hamiltonian, the operator T_{ee} is related to the Coulomb interaction in the electron-electron scattering, and the operator V_{pe} is related to the photon-electron interaction in the photoionization process. The wavefunctions ψ_i and ψ_f are for the initial and final state, respectively. Pattard et al. [12] showed that the total transition amplitude in Eq. 2.5 can be separated into two terms as

$$a_{f,i}^{\mathrm{KO}} \propto \langle \psi_f | -i \int_0^\infty e^{i\mathrm{H}_0 t}\ \mathrm{T_{ee}}\ e^{-i\mathrm{H}_0 t}\ dt\ \mathrm{V_{pe}} | \psi_i \rangle \quad , \tag{2.6}$$

for the KO mechanism, and as

$$a_{f,i}^{\mathrm{SO}} \propto \langle \psi_f | \mathrm{V_{pe}} | \psi_i \rangle \quad , \tag{2.7}$$

for the SO mechanism, respectively. The KO process may usually be seen as a quasi-classical mechanism where a primary electron transfers energy to a second electron in a collision-like interaction, corresponding to the T_{ee} operator [10–12]. If the total energy of the electron pair is above the DIP limit, and the transferred

energy exceeds the binding energy of the second electron, the system may end up as a doubly ionized final product with two electrons in the continuum. The SO process is purely a quantum mechanical process, which may be understood from the sudden approximation from a fast removal of a primary electron from the neutral system, e.g. by photoionization. The fast removal of the electron will suddenly change the Hamiltonian of the system, which the remaining electron(s) in the system will have to relax into. In the relaxation process, there is a probability that a secondary electron will relax into an energetically accessible unbound eigenstate of the new Hamiltonian, which can be seen as the second electron being 'shaken off' into the continuum [10–12].

2.2.2 Auger decay

When a core electron is ejected into the continuum, for example by a photon, creating a vacancy deep down in an atomic or molecular system, an almost immediate relaxation mechanism (on the femtosecond scale) may occur where the vacancy decays in an *indirect process* known as *Auger decay*. The Auger decay can be considered as a stepwise process, where an electron from a higher orbital relaxes and fills the vacancy, transferring the energy corresponding to the relaxation to a second electron in the system. In this process the second electron may gain sufficient energy to be emitted, resulting in a doubly ionized final product with a photoelectron and a single Auger electron in the continuum. The process of a single Auger (SA) decay event after photoionization of a core electron is illustrated in Figs. 2.2 (a)-(b). The rate of the single Auger decay, $\mathrm{SA}_{\alpha\beta}$, can be approximated from first-order perturbation theory, expressed as [13, 14]

$$\mathrm{SA}_{\alpha\beta} \propto \left| \left\langle \psi_\beta^{2+} \middle| \sum_{i<j}^{N} \frac{1}{r_{ij}} \middle| \psi_\alpha^{+} \right\rangle \right|^2 \quad , \tag{2.8}$$

where ψ_α^+ is the singly photoionized state containing N electrons, and ψ_β^{2+} is the doubly ionized final state of the system with $N-1$ electrons and one Auger electron in the continuum. The summation term containing $1/r_{ij}$ corresponds to the static Coulomb repulsion between each electron pair in the system.

More than one Auger electron may be emitted into the continuum in a so called multi-Auger decay process. The most basic multi-Auger process is the double Auger (DA) decay that leaves the system in a triply ionized final state and two Auger electrons in the continuum. The process of a direct DA process, i.e. when the Auger electron pair shares arbitrarily the excess energy, can be explained from the picture of the KO and SO mechanisms [15–17]. In this picture the rate of DA decay from the KO mechanism may be expressed as [16, 17]

$$\mathrm{DA}_{\alpha\beta\gamma}^{\mathrm{KO}} \propto \sum_\beta \mathrm{SA}_{\alpha\beta}\ \Omega_{\beta\gamma}(\varepsilon_0) \quad , \tag{2.9}$$

where $\mathrm{SA}_{\alpha\beta}$ is the rate of the SA decay from the initial state ψ_α^+ to the intermediate state ψ_β^{2+}, i.e. according to expression 2.8. The term $\Omega_{\beta\gamma}(\varepsilon_0)$ is the electron-electron collision strength of the inelastic scattering of a SA electron with a kinetic energy

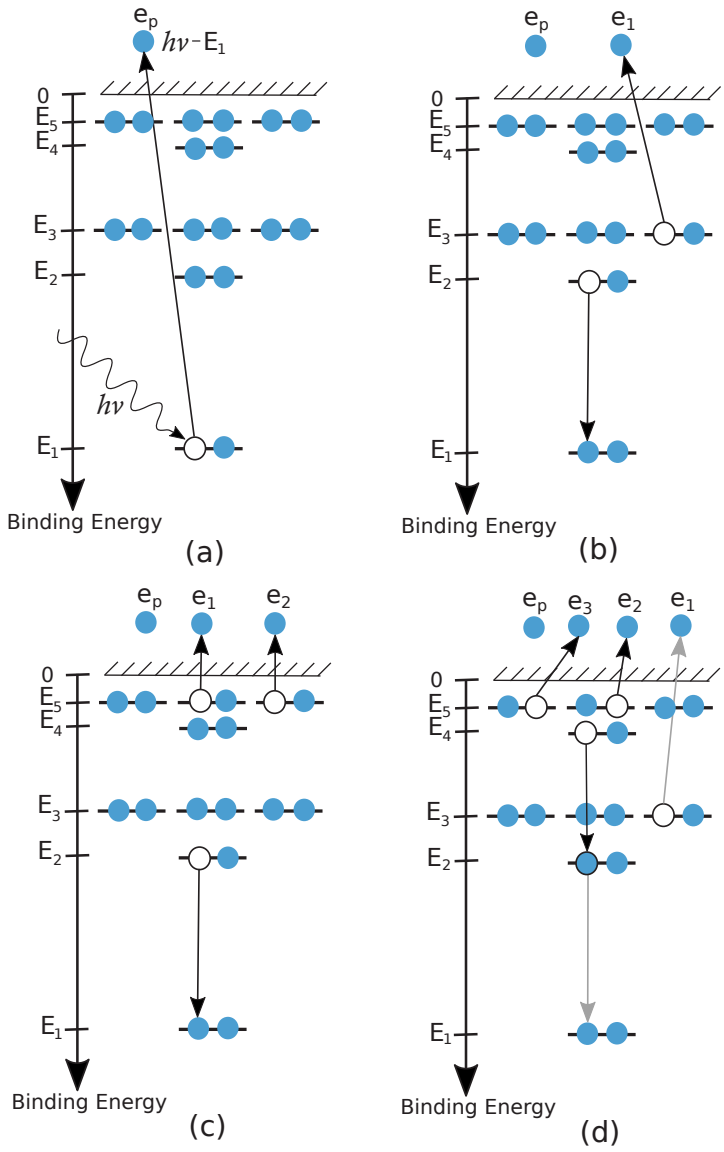

Figure 2.2: Illustration of Auger decay processes after a photoionization process (a) of an electron with a binding energy of E_1. During the decay of the core vacancy either a single Auger (b) or a double Auger decay (c) process emits (an) electron(s) into the continuum. Figure (d) illustrates stepwise multi-Auger decay emitting three electrons into the continuum from two separate (grey and black arrows) Auger processes.

of ε_0, with the ψ_β^{2+} intermediate state. The direct DA decay process through the KO mechanism can be seen as an inelastic collision of a SA electron with another electron in the system, ionizing an electron pair into the continuum leaving the system in the ψ_γ^{3+} final state. The contribution to the DA decay rate from the SO mechanism may be expressed as [16, 17]

$$\mathrm{DA}^{\mathrm{SO}}_{\alpha\beta\gamma} \propto \sum_\beta \mathrm{SA}_{\alpha\beta} \left| \left\langle \psi_\gamma^{3+} \middle| \psi_\beta^{2+} \right\rangle \right|^2 \quad , \tag{2.10}$$

which can be seen as an equivalent process as described for expression 2.7, after a sudden removal of an initial Auger electron. The Auger electron pair emitted from a DA event shares a total kinetic energy corresponding to the states involved in the DA decay process. The process of double Auger decay is illustrated in Fig. 2.2 (c).

From the expression for the Auger rates above it is possible to see that the average probability for an Auger decay event into a specific final state will depend on the Auger rates summed over all possible permutations of Auger decay pathways leading to the final state. The average probability of a multi-Auger event will also depend on possible indirect pathways, where a multiply charged final state may be reached by separate subsequent Auger decay processes, emitting multiple Auger electrons with no energy correlation. The process of step-wise Auger decay is illustrated in Fig. 2.2 (d). Theoretical quantum chemical estimations of multi-Auger processes may therefore be very demanding in terms of a complete picture of the multiple pathways leading to all the possible final states. To stimulate theoretical development in this direction, experimental investigations have been done in Papers IV, V, and VI, where the DA and triple Auger (TA) decay probabilities have been investigated in a series of molecules. In these experimental investigations, both the direct and indirect pathways are included.

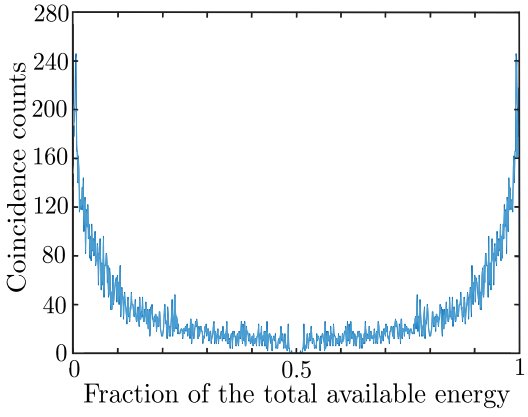

Figure 2.3: Energy sharing of an electron pair from a direct double Auger decay process.

Electrons emitted in a direct (Auger or otherwise) process will usually have an unequal energy sharing between them as they leave the sample (See Refs. [29,30], and Refs. therein). In figure 2.3, the fractions of kinetic energy of one electron relative to the total kinetic energy of the electron pair is plotted, which appears as a U-shaped energy distribution between the Auger electron pair emitted. Such a distribution means that there is a large probability that one of the emitted electrons has a majority of the total kinetic energy while the other electron has just a fraction of the energy. This is similar to what can be seen in direct double photoionization when the electron pair has a total kinetic energy of >100 eV [10]. Interestingly, the energy sharing distribution between three Auger electrons in a direct TA decay process is, according to the theoretical investigation by Liu et al. [18], highly asymmetric similar to the direct DA decay process, with one fast and two slow Auger electrons.

2.3 Molecular dissociation

When a molecular species loses valence electrons, either through photoionization or Auger decay processes, it may dissociate into fragments. This happens when the molecular bonds elongate and weaken, due to a loss of electrons from bonding orbitals, leading to fragmentation of the molecule. If any of the fragments are left in a "semi-stable" excited state from the initial ionization process, they may autoionize during or after the dissociation process. By "semi-stable" it is implied that the autoionization process in a molecule may be on the same time scale as the dissociation process [6]. After the photoionization of the molecule AB, formed by the atoms A and B, the dissociation process may, for example, be expressed as a stepwise process

$$\mathrm{AB} + \mathrm{h}\nu \rightarrow \mathrm{AB}^+ + e^- \rightarrow \mathrm{A}^+ + \mathrm{B}^* + e^- \rightarrow \mathrm{A}^+ + \mathrm{B}^+ + e^- + e^- \quad , \tag{2.11}$$

where the molecule AB dissociates into a positively charged fragment A^+ and an excited neutral fragment B^* after the photoionization. The fragment B^* then autoionizes by emitting a second electron into the continuum, as the molecule fragments.

In the dissociation process of a multiply-charged molecule, the fragments may carry a number of the charges created in the ionization process of the molecule, creating a large repelling Coulomb force between the fragments [19, 20]. The dissociation process of a molecule can be studied for example by photoion-photoion coincidence spectroscopy or a combination of photoelectron(-photoelectron) and photoion(-photoion) spectroscopy (see section 4.4.2) [20].

Chapter 3

Experimental technique

This thesis is primarily based on electron kinetic energy measurements with a time-of-flight (TOF) magnetic bottle spectrometer. This spectrometer can accurately measure the time it takes for electrons to fly a known distance, through a straight flight tube. The electron flight times can then be converted to kinetic energy. This experimental setup requires a pulsed light source that provides well defined timing of the electrons' flight times. The spectrometer is primarily designed for gaseous samples, and the measurements need to be performed in high vacuum suitable for electrons, UV light, and X-ray radiation to travel freely, which are otherwise easily absorbed or deflected by other atoms or molecules in the spectrometer.

This chapter presents a brief introduction to the experimental techniques which this thesis is based on. The time-of-flight technique using a magnetic bottle spectrometer is a highly useful tool used for electron coincidence measurements. Furthermore, the TOF-technique can also be used for ion mass to charge ratio measurements, and may therefore give complementary information about the dissociation of molecules in addition to electron coincidence spectroscopy. In building on that, the combination of electron and ion TOF spectroscopy will be presented in this chapter. Pulsed light sources, in the form of a Helium gas discharge lamp and synchrotron radiation facility, will be presented as a means to initiate the ionization process in the sample gas. Finally, a mechanical chopper will be presented as a means to adjust the light pulse repetition rate for measurements at synchrotron radiation facilities.

3.1 Coincidence measurements

The basic principle of coincidence measurements is to measure two or more originating signals from the same event that are detected within a certain time window. In this thesis, coincidence measurements have been performed on the time-of-flight for electrons as they are emitted from an ionization event after a single photon absorption in a sample atom or molecule. All electrons emitted from an ionization event may be directly correlated by a shared total kinetic energy or indirectly correlated via secondary processes. The time window for coincidence measurements in this thesis is naturally set, by a start signal and ranges until the slowest possible electron reaches the detector. In other words, a clear start-multi-hit-timing is of great importance in this technique, with a very well defined start signal which occurs at the exact same time relative to each photoionization event. This is often achieved

by creating a start signal from each light pulse that may initiate a photoionization event, after which the time window for the multi-electron detection is open. This means that the repetition rate of the light source has to be sufficiently low to allow the slowest electrons to be detected before the subsequent light pulse arrives, i.e. the inverse of the repetition rate has to be longer than the flight time of near zero kinetic energy electrons, which in a 2.2 m long TOF instrument is typically about 4-6 μs. Coincidence measurements may also be performed on ions, resulting from the ionization process, simultaneously to the detection of electrons. The basic principle is the same as for the electrons, and provides crucial information about the dissociation mechanisms of molecules.

The idea with coincidence measurements is to study correlated events, which means that reliable data can only be gathered when the probability to ionize the sample gas on a single light pulse is low, typically less than a few percent. If the probability is higher the chance to ionize more than one target atom or molecule may be high, and electrons from two uncorrelated events may be detected within the same time window. The probability, $\mathrm{P}(n)$, for n photoionization events to occur per light pulse can be described by a Poisson distribution [21]

$$\mathrm{P}(n) = \frac{\lambda^n e^{-\lambda}}{n!} \quad , \tag{3.1}$$

where λ is the average number of photoionization events per light pulse. The average number of photoionization events per light pulse depends on several factors. Most notably on the intensity of the light, i.e. the number of photons, and the number of target atoms or molecules, which is related to the the gas density in the interaction region. These factors can often be adjusted easily such that the probability of photoionizing two or more target atoms or molecules is kept sufficiently low as to not interfere with the real coincidence data. The uncorrelated detection of electrons from different ionization events will hereafter be referred to as "accidental coincidences". In addition to the accidental coincidences, there are other interfering false coincidence signals that come from real, but unwanted, coincidences. A majority of these unwanted coincidences originates from the release of secondary electrons from collisions of stray photons, photo- or Auger electrons on metal surfaces or gas in the spectrometer. The detection rate of these must be minimized, by minimizing the amount of metal surfaces or gas, in the interaction region during the experiments.

Accidental coincidences will have a statistical nature, and therefore most often do not contribute to the random background in the electron spectrum, and can often be partially removed by adding conditions to the data during the analysis. Electrons from two different photoionization events are often faster than expected because two separate photons initiated the different ionization events, thus increasing the total available energy. Therefore these events may be partially removed by energy conservation conditions, where electron data that exceed the energy of a single photon are removed after the measurement. Other false coincidences may have a more random nature, and contribute to the overall background in the electron spectrum. This background can be partially removed by other means in the data analysis, for example by selecting two electrons in coincidence with a third related

photo- or Auger electron from the same ionization event. By these stratagems the effect of the false and accidental coincidences will be minimized from the coincidence data.

3.2 Experimental setup

3.2.1 Electron, ion, and light detectors

The light pulses that initiate the ionization processes in the sample gas are detected by a photomultiplier tube (PMT) [27], which is sensitive to radiation in the UV and X-ray spectrum. In the set-up used in for this thesis, the incident light is detected by a PMT, which creates an electron current by the photoelectric effect upon a photon impinging the surface of a Cu photocathode covered by a BeO layer. The latter increases the photosensitivity of the cathode in the region of UV to soft X-ray radiation. The electrons are accelerated by an electric potential toward a sequential chain of Cu dynodes, which will amplify the current by secondary electron emission at each stage of the chain, resulting in a cascade of electrons through the PMT. The electrons emitted in the PMT are accelerated along the dynode chain by an sequentially increasing electric field created by a voltage divider circuit, giving each dynode about 100 V higher potential than the preceding one. The cascade of electrons are collected by an anode at the end of the dynode chain, and read out for the PMT detector. A simple schematics over a PMT detector can be seen in Fig. 3.1, where an incident photon initiates a cascade of electrons through the dynode chain. The PMT used in this thesis is the model R595 by Hamamatsu, with 20 dynode stages giving a typical electron multiplication gain on the order of 10^6 and a signal rise time of about 14 ns [28].

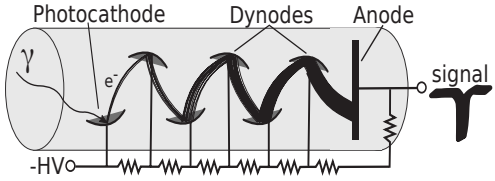

Figure 3.1: Schematics of a photomultiplier tube, where a photon, γ, initiates an electron cascade through the PMT.

For the detection of single particles, i.e. electrons and ions, at the end of their flight path, a microchannel plate (MCP) detector is used. The MCP is a planar detector often made of a highly resistive material, typically a slab of lead glass with a thickness of about 2 mm, densely perforated by microchannels with a diameter of about 10 μm. The MCP functions as an amplifier for particles that release secondary electrons upon impinging on the inside of the microchannels, which are treated in such a way to optimize the semiconductive properties favoring the release of secondary electrons [26]. The released electrons will continue through the microchannels, releasing further secondary electrons from collisions with the wall

inside of the channels, creating a cascade of electrons. The electron current is accelerated through the MCP by an applied voltage difference between the front and back of the plate, and the signals may be read out from an anode located behind the MCP detector. To increase the electron multiplication by the MCP, the microchannels are typically biased at an angle of ~8° relative to the MCP input surface, to increase the probability for electron collisions with the walls inside the microchannels. To further increase the electron multiplication factor from the detector several MCPs can be put in series resulting in a multiplication factor up to 10^7 [26]. The plates in an MCP stack are rotated 180° relative to each other, in a so called chevron (2 plates) or Z-stack (3 plates) arrangement. A schematic picture of a chevron arrangement of two MCPs can be seen in Fig. 3.2. The electron detection efficiency for a MCP detector, is typically on the order of 50-65% [26] for electrons with kinetic energies relevant for this thesis, and is mainly determined by the open area ratio of the microchannels relative to the total area of the glass plate and the kinetic energy of the impinging electron. Each microchannel has a dead time for sequential detection of electrons, i.e. the average time it takes for the channel to recover after the loss of electrons, which can typically be on the order of 10^{-2} s [26]. For the studies in this thesis the dead time for each channel will generally not be a problem because of the high density of microchannels on each MCP and due to the relatively low rate of electrons impinging the detector.

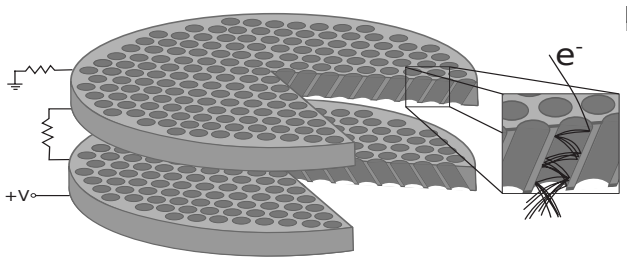

Figure 3.2: Illustrative figure of two MCPs in a chevron arrangement.

3.2.2 Magnetic bottle time-of-flight spectrometer

In this thesis, a magnetic bottle time-of-flight spectrometer has been used for studies on multi-electron ionization processes in atoms and molecules after single photon absorption. The basic operational principle of the magnetic bottle TOF-spectrometer is to determine the kinetic energy of electrons emitted from an ionization event, which is done by measuring the time it takes for the electrons to travel through a long flight tube. The concept of using a magnetic bottle TOF-spectrometer for multi-electron coincidence studies was devised by J. H. D. Eland at Oxford University, England [22]. The basic schematic of the spectrometer setup used for the multi-electron measurements in this thesis can be seen in Fig. 3.3. In this setup an effusive gas needle close to the interaction region introduces the sample gas that may be photoionized by UV or X-ray radiation from a pulsed light source. The gas needle

is mounted onto a xyz-manipulator, which is used to optimize the needle position relative to the electron flight tube and the beam of ionizing radiation. The ionizing radiation from the light source intersects the sample gas in the interaction region perpendicular to the gas needle, and each light pulse is detected by a photomultiplier. Each light pulse will initiate a time window for the detection of the electrons emitted from an ionization event and start the timing of the electrons as they travel though a 2.2 m long electron flight tube. The electrons are detected by a MCP detector at the end of the flight tube, and the flight times are registered relative to the light pulse that initiated the ionization event. The spectrometer is under vacuum during operation so the electrons may travel freely in the spectrometer without being absorbed by stray atoms or molecules in the flight tube. The background pressure is typically in the low 10^{-7} mbar range without a gas load, and typically about $0.8\text{-}2{\cdot}10^{-6}$ mbar with a gas load in the spectrometer during operation. Fully optimized, the spectrometer has a spectral energy resolution of about $\Delta E \approx E/50$, where E is the kinetic energy of the emitted electron. This means that the energy resolution ranges normally from about 50 meV for 1 eV electrons to about 10 eV for electrons of 500 eV.

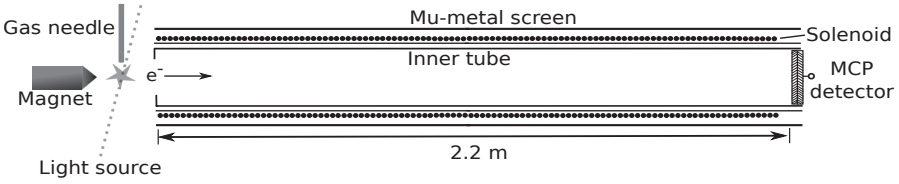

Figure 3.3: Illustration of a magnetic bottle time-of-flight electron spectrometer.

The electrons emitted from the ionization processes in the interaction region have velocities directed into the whole 4π solid angle, so high detection efficiency requires the spectrometer to collect electrons emitted in the whole solid angle. This is achieved by a neodymium-iron-boron permanent magnet, whose magnetic field arrangement consists of a conical shaped pole piece that is located close to the interaction region, creating a magnetic flux density of about 1 T at the tip of the pole piece. The permanent magnet is mounted on a xyz-manipulator that determines the position of the magnet relative to the gas needle and the solenoid field. The magnetic flux density from this magnet arrangement resembles the shape of a bottle neck, hence the name magnetic bottle, with high density close to the tip of the conical pole piece which leads up to a region of weaker magnetic flux density. The magnetic bottle is extended over the entire electron flight path toward the MCP detector by a solenoid wired around the electron flight tube, which creates a homogeneous magnetic field, of a few mT, parallel to the axis of the flight tube. The magnetic arrangement and the bottle neck shaped magnetic field can be seen in Fig. 3.4. The principle of the magnetic bottle can be understood by looking at an electron moving in a magnetic field, $\vec{B}$, which will experience an acceleration according to the magnetic component, i.e. without the presence of an electric field, of the Lorentz force

$$\vec{F} = q(\vec{v} \times \vec{B}) \quad , \tag{3.2}$$

where q is the charge of the electron and $\vec{v}$ its velocity, which has components $\vec{v}_\perp$ and $\vec{v}_{||}$ perpendicular and parallel to the magnetic field, respectively. According to this formula the force working on the electron will point perpendicular to the $\vec{v}_\perp$ velocity component, which will induce a helical motion on the electron's trajectory in the magnetic field.

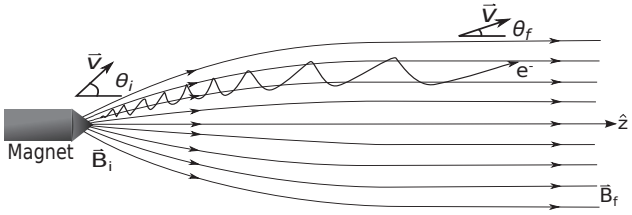

Figure 3.4: Illustration of the magnetic bottle field lines.

An electron with a gyromotion trajectory in a magnetic field has a magnetic moment [23] according to the formula

$$\mu = \frac{\mathrm{m_e}\vec{v}_\perp}{2|\vec{B}|} \quad , \tag{3.3}$$

where $\mathrm{m_e}$ is the electron mass. As the electron travels away from the interaction region, it will make a transition from a region of a strong magnetic flux density to a region with weaker density. For this transition, the magnetic moment will be invariant for small changes of the magnetic flux density experienced by the electron over one helical rotation [23]. This implies that the magnetic moment in the strong field region will be equal to that in the weak field region according to

$$\frac{\mathrm{m_e}\vec{v}_{s\perp}}{2|\vec{B}_s|} = \frac{\mathrm{m_e}\vec{v}_{w\perp}}{2|\vec{B}_w|} \quad , \tag{3.4}$$

where the suffixes s and w refer to the regions with strong and weak magnetic flux densities, respectively. For the equal sign to hold, the velocity perpendicular to the magnetic field lines have to decrease as the electron transits towards a region of weaker magnetic flux density. As the kinetic energy is conserved for an electron moving in a magnetic field, the total magnitude of the velocity will be conserved in its transit in the magnetic field. This means that if the velocity component perpendicular to the magnetic field lines decreases the velocity component parallel to the field will increase an equal amount. Thus an electron with a velocity vector at an initial angle, θ_i, with respect to the axis of the flight tube will start to become more parallel to the magnetic field as it is travelling along the field lines of the magnetic bottle, from the strong field to the weak field region. As the electrons move into the homogeneous magnetic field region, it will reach a final velocity angle, θ_f, along the flight path that is nearly parallel to the axis of the flight tube.

The expressions above imply that an electron with a velocity component towards the permanent magnet will, in accordance with the Lorentz force and the expression for the magnetic moment, turn around and get a trajectory towards the electron

flight tube. The property of this magnetic field arrangement makes it well suited for TOF measurements on electrons emitted at random directions from the interaction region, which was thoroughly investigated by Kruit and Read in the early 1980's [25]. The magnetic bottle collects essentially all electron emitted in the 4π solid angle in the spectrometer, with small electron losses at near zero kinetic energy and at high kinetic energy (>400 eV). This can be seen from the combined collection and detection efficiency that is described in section 3.2.5.

3.2.3 Augmented in-line electron and ion spectrometer

The magnetic bottle TOF-spectrometer set-up designed for multi-electron coincidence measurements, can be modified to measure the atomic and molecular ions and ionic fragments created from the ionization events in the interaction region, either separately or in coincidence with the electrons. The ions created from an ionization process are very interesting for electron coincidence studies, e.g. where they can give information about the final charge states and released energy in molecular dissociation processes initiated by the emission of electrons. The electron spectrometer described in the previous section can e.g. be augmented by an in-line ion TOF-spectrometer, which replaces the conical permanent magnet by a hollow ring magnet at the entrance of the ion flight tube. This modification of the electron spectrometer for multi-electron-multi-ion coincidence studies was first introduced by J. H. D Eland and R. Feifel [31] in 2006, and the schematics of this set-up can be seen in Fig. 3.5. The hollow ring magnet has a pierced conically shaped pole piece on the front that forms the shape of the magnetic bottle for the electrons in the interaction region, with the basic idea of extracting the ions in opposite direction to the electrons. This magnet arrangement creates a slightly weaker magnetic field for the electrons compared to the original arrangement, which creates a smaller gradient of the magnetic $\vec{B}$ field across the interaction region, resulting in a reduced resolving power for the electron kinetic energy to about $E/\Delta E \approx 20$.

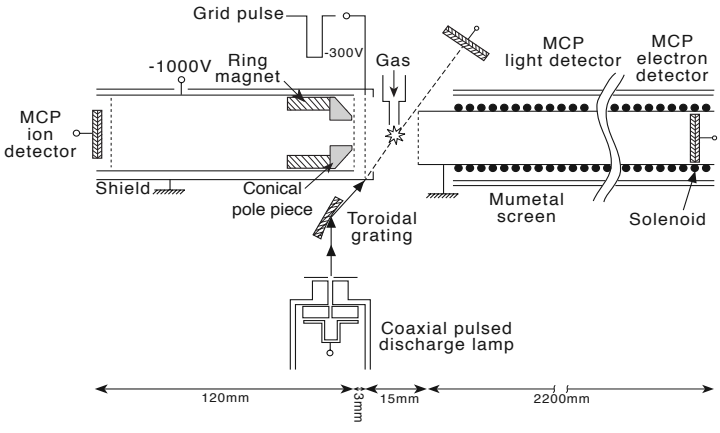

Figure 3.5: TOF PEPEPIPICO spectrometer. Taken from Ref. [33].

The ion set-up is based on a Wiley-McLaren mass spectrometer [32], where the ions are extracted from the interaction region by an extraction voltage of about -300 V on a Cu-grid placed a few millimetres in front of the ion flight tube. The extraction voltage has to be pulsed with a small delay of about 100-200 ns relative to the light pulse to give the slowest electron time to escape into the electron flight tube. The flight tube has a Cu-grid on the front giving the electrons a field-free region inside the flight tube. The principle of a Wiley-McLaren ion TOF-spectrometer is to obtain good time-focusing of the ions at the detector, such that all emitted ions with the same mass/charge ratio (m/q) reach the detector at the same time, independent of their initial positions in the electric field at the point of ionization. To create a uniform electric field in the interaction region for the ions, the gas needle is also pulsed by about 100-200 V, with the exact value highly dependent on the relative position of the needle in the interaction region. After the extraction from the interaction region, the ions are accelerated by a potential of -1000 V on a Cu-grid applied to the front of the ion flight tube. The ions are extracted through the hollow ring magnet inside the ion flight tube giving a field-free region of 120 mm where the ions can travel freely towards a MCP detector at the end of the flight tube. These potential fields with the given flight distance provide a resolving power for the ion mass of about $m/\Delta m \approx 50$.

Besides a reduced electron resolution, in comparison to the original electron spectrometer, the augmented in-line electron-ion spectrometer also introduces possible accidental coincidence counts from secondary electron emission from electron and ion collisions with the Cu-grids. The grids also slightly reduce the collection and detection efficiency, relative to the open area ratio (80-90%) of the grids, for both the electrons and ions. With this set-up the typical collection and detection efficiency is about 45-55% for the electrons and about 15-25% for the ions.

3.2.4 Augmented perpendicular electron and ion spectrometer

An alternative augmentation for the combination of coincidence electron and ion detection was developed during the course of this thesis, which consists of a geometrically perpendicular magnetic bottle and ion spectrometer set-up. This electron-ion spectrometer is schematically illustrated in Fig. 3.6. One advantage of this set-up, compared to the in-line electron and ion detectors, is that in this set-up the same conical permanent magnet as in the electron only set-up can be used. This retains basically the full electron energy resolution of the magnetic bottle as well as the collection and detection efficiency of the electrons. Another advantage of this set-up is the addition of a delay-line behind the ion MCP detector, which gives position imaging possibilities for the ions.

The ion spectrometer devised for this unique electron-ion coincidence set-up is based on the principle of velocity map imaging (VMI) [35]. The extraction and focusing of the ions onto the MCP position sensitive detector is achieved by three electrodes, located before the ion flight tube, in the form of plates with central hole cut-outs. Two of the electrode plates, one located below and one above the

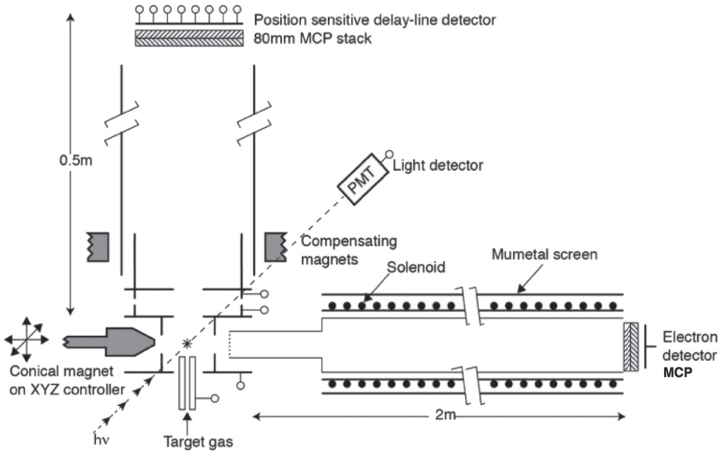

Figure 3.6: TOF PEPEPIPICO spectrometer. Taken from Ref. [34].

interaction region, create an extraction potential across the interaction region for the ions toward the ion flight tube. These plates are therefore referred to as the repeller and extractor plates, respectively. The third plate is located at the entrance of the ion flight tube and further accelerates and focuses the ions towards the detector, and is therefore referred to as the accelerator plate. The sample gas is introduced into the interaction region from below through the repeller plate by a capillary gas needle, which is electrically insulated from the repeller.

A necessary component of the velocity map imaging technique is the position sensitive detector, which in our set-up consists of a set of MCPs arranged in a chevron-stack equipped with a three layer delay-line configuration in a hexagonal geometry behind the MCP stack. By measuring the time delays between the signals produced in the delay-lines by the electron current from the MCP stack, the xy-positions of where the ion hit the detector are obtained. The z-component of the ions movement is related to the time-of-flight of the ions, and by recording all of these components valuable information of the molecular dissociation process can be revealed.

Similar to the original electron-ion spectrometer set-up presented above, pulsing of the ion extraction is necessary in order to not compromise the electron trajectories. The voltages to the repeller, extractor and accelerator plates are applied after a delay that gives even the slowest electrons time to enter the electron flight tube, which is extended closer to the interaction region by a tailor-made rectangular aperture fitted in between the repeller and extractor plates. This extension shields the electrons earlier after the ionization event, which therefore decreases the required delay time between the light pulse and the potentials for the ion extraction. The decreased time delay for pulsing the ions favors the catching of energetic ion fragments that would otherwise have time to escape the interaction region. In this perpendicular set-up, the pulsed potentials on the repeller and extrator plates are about +500 V and -500 V, respectively, with the pulsed potential on the needle determined on its

relative position in between the repeller and extractor plates. The accelerator plate is pulsed at a much higher voltage, of about -5 kV, for a higher acceleration of the ions towards the MCP detector. Furthermore, the ion flight tube is at the same potential as the accelerator plate, but as a static potential, which gives the ions a field free region for their trajectory inside of the flight tube.

The basic principle of VMI is to resolve the different velocities of the ions after a dissociation process. In VMI it is possible to study details of the fragmentation dynamics, because the velocities are determined by the Coulomb forces acting on the fragments over the ionized molecular potential energy surface(s) on which the dissociation takes place. The principle of VMI can be understood by imagining the dissociation of a homonuclear diatomic molecule after double ionization, where both fragments gain equal charge after the dissociation process. These fragments will have velocities in an outward direction from the interaction region in opposite directions from each other. When the extraction potentials are applied, the ions will be accelerated toward the ion flight tube, while still retaining a radial velocity component in perpendicular direction relative to the flight tube axis. The final radial positions of the extracted ions onto the MCP detector are determined by the total energy gained, the mass/charge ratio, and the initial kinetic energy of the ion fragments, and will therefore be proportional to the initial radial velocity component of the ions after the dissociation process. Ions whose velocity have a component in opposite direction to the ion flight tube will be accelerated slightly more than ions emitted towards the flight tube. The velocity-focusing, and therefore also the time-of-flight focusing, of these ions is determined by the ratios of the extraction potentials on the three plates, and are in practice chosen so a specific range of ion m/q ratios are focused for the best time of flight resolution.

An advantage of this set-up is that there are no grids on the extractor and accelerator plates, which is beneficial for the transmission efficiency for the extraction of the ions as well as less secondary electron emissions from ion collisions or from scattering of stray light. The inhomogeneous electric fields produced from the plates work as an Einzel lens that focuses ions with the same initial velocity, independent of their initial positions in the interaction region, at the same spot on the detector, which means that the ion velocity-resolution is less affected by the size of the light-matter interaction region. A disadvantage of this set-up is the disturbance of the ion trajectories in the interaction region from the permanent magnet, which is mostly affecting the lighter ions such as hydrogen and deuterium. The disturbance can be counteracted by the introduction of compensating permanent magnets placed along the ion flight tube, shifting the ions back towards the center of the MCP detector.

3.2.5 Collection and detection efficiency

One of the most important properties of the magnetic bottle TOF-spectrometer is the high collection and detection efficiency for the electrons emitted in the light-matter interaction region after (single) photon absorption by the sample. This makes the experimental technique well suited for studies on single photon multi-electron processes, where a good combined collection-detection efficiency significantly reduces

the data acquisition time. The magnitude of the collection-detection efficiency is determined by two aspects of the magnetic bottle TOF-spectrometer; the efficiency with which the emitted electrons are collected in the interaction region and guided into the electron flight tube, and the efficiency with which the electrons are detected by the MCP detector at the end of the flight tube. The detection efficiency of the MCP detector is inherently 50-65% from the working principle of the detector, as explained in a previous section. The collection efficiency of the electrons in the interaction region is mainly determined by the optimization of the experimental set-up, including the position of the conical permanent magnet relative to the magnetic field generated by the solenoid, and to the position of the gas needle. The strength of the magnetic field from the solenoid as well as potential electric fields applied to the interaction region will also determine the collection efficiency of the electrons, where the extraction of slow near zero kinetic energy electrons may require a small accelerating voltage, typically less than a volt, across the interaction region. The collection-detection efficiency will also depend on the kinetic energy of the emitted electrons, where very fast electrons may escape the magnetic bottle field arrangement. Detected electrons, and light signals may also be lost in the electronics if they are too weak or if signal thresholds are set too high in the conversion from analogue to digital signals.

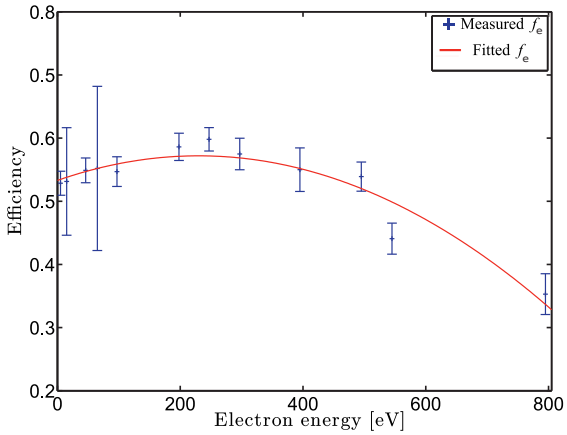

Figure 3.7: Combined collection and detection efficiency as a function of electron kinetic energy of the magnetic bottle TOF-spectrometer. Obtained from our study on single and double Auger decays presented in Paper IV of this thesis.

A well known collection-detection efficiency as a function of electron kinetic energy is essential to reliably determine the probability of multi-electron processes. The combined collection-detection efficiency for a magnetic bottle TOF-spectrometer may accurately be determined from single Auger decay measurements on noble gas atoms, e.g. neon, argon, and krypton, after an initial core hole photoionization, as explained in detail in Ref. [29]. The absolute collection-detection efficiency may be determined from the expression of the total detected single Auger coincidences

(C_{SA}) where both the Auger and photo-electron are detected

$$C_{SA} = N_{SA} f_e^A f_e^P \quad , \tag{3.5}$$

and from the expression for the Auger electron (A_{SA}) being detected without the photoelectron from the single Auger event

$$A_{SA} = N_{SA} f_e^A (1 - f_e^P) \quad , \tag{3.6}$$

where f_e^A and f_e^P are the combined collection-detection efficiencies for the Auger and photo-electron, respectively, and N_{SA} is the true number of single Auger events in the interaction region. By taking the ratio between these two quantities, the collection efficiency for the photoelectron may be determined as

$$f_e^P = \frac{C_{SA}}{C_{SA} + A_{SA}} \quad . \tag{3.7}$$

The quantities C_{SA} and A_{SA} can be obtained from the electron pair and single electron data, respectively. The collection-detection efficiency of the Auger electron can be obtained if the expression for the detected single Auger electron is expressed as $A_{SA} = N_{SA} f_e^P (1 - f_e^A)$ instead. A typical collection-detection efficiency as a function of electron kinetic energy obtained for the magnetic bottle TOF-spectrometer used for this thesis can be seen in Fig. 3.7. The figure was obtained from single Auger decay measurements on Ne and Kr over a relatively large electron energy interval. This figure shows that the collection-detection efficiency is approximately 55-60% for electron energies close to zero up to electrons with a kinetic energy of about 450 eV. The inherent detection efficiency for a MCP detector is about 50-65%, which implies that the magnetic bottle has an electron collection efficiency close to 100% over a relatively large kinetic energy interval. The collection efficiency is typically lower for fast electrons that may escape the magnetic bottle, which can be seen in Fig. 3.7.

3.3 Light sources

Two light sources were used for the coincidence studies carried out in this thesis, a pulsed Helium gas discharge lamp and synchrotron radiation facility. There are mainly two requirements on the light when performing coincidence measurements on atoms and molecules. First, the light needs to be monochromatic with sufficient energy to remove more than one electron from the sample system, either via direct photoionization or some indirect process, e.g. Auger decay. This typically requires photons with energies greater than several tens of eV, which is obtained from light in the vacuum ultraviolet (VUV), extreme ultraviolet (XUV), or the soft X-ray wavelength spectrum. The energy regions for the photons in VUV and XUV light ranges from about 6-10 eV up to about 120 eV, while the soft X-ray energy region ranges from about 100 eV up to a few keV. The second requirement is that the light must be pulsed, with a pulse length that is considerably shorter than the flight time of the electrons, and with a repetition rate of the light that gives the slowest electrons time to reach the detector before the next pulse alights the interaction region.

3.3.1 Helium gas discharge lamp

The basic principle of the Helium gas discharge lamp [22, 37] is, as implied by the name, operated by induced discharges in He gas inside a capillary made of a ceramic insulator (Macor). A schematic figure of the He gas discharge lamp is presented in Fig. 3.8, with a simplified electronic circuit. The lamp is driven by a high voltage (HV) power supply, typically applying 7-9 kV, that charges a capacitor connected to a hollow cathode. The lamp is fired by a fast HV switch, that can either be of a hydrogen Thyratron [38] type or a fast high voltage solid state switch based on MOSFET technology [39]. The switch rapidly connects the HV supply side of the capacitor to ground, resulting in a rapid rise of the cathode's potential. The high potential on the cathode will cause a discharge through a He gas filled capillary, exciting and ionizing the He gas, which will then deexcite by photon emission at several discrete energies. The typical firing rate of the lamp is around 3-5 kHz, producing light pulses of approximately 10 ns duration.

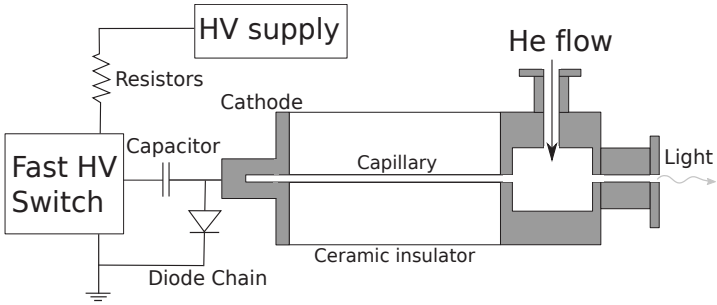

Figure 3.8: Schematic figure of the He gas discharge lamp, with a simplified electronic circuit.

The single specific wavelength of the light of interest is selected by a toroidal grating monochromator. The helium emission lines interesting for the studies in this thesis are listed in Table 3.1, with the He I lines interesting for single photoionization and the He II lines interesting for double photoionization studies, due to their respective energies. The pulse shape of the light coming from the lamp consists of a short and intense main pulse, followed by a less intense broad afterglow pulse. The shape of the pulse is dependent on several factors, where the supplied HV voltage and the He gas flow are the largest factors, and by varying these factors the shape and afterglow effect on the pulse can be optimized. The light pulse can be monitored by either an antenna placed close to the cathode, picking up an electromagnetic signal from the discharge, or by a optical fibre inside of the lamp that picks up the visible part of the light from the discharge.

Table 3.1: Main helium emission lines [36] in the UV spectral region that are of interest for the studies of this thesis.

Helium line	Electronic transition	Wavelength [Å]	Energy [eV]
He Iα	1s2p $^1P_1 \rightarrow$ 1s^2 $^1S_0$	584.33	21.22
He Iβ	1s3p $^1P_1 \rightarrow$ 1s^2 $^1S_0$	537.03	23.09
He IIα	2p $^2P\rightarrow$ 1s $^2S_{1/2}$	303.78	40.81
He IIβ	3p $^2P\rightarrow$ 1s $^2S_{1/2}$	256.32	48.37
He IIγ	4p $^2P\rightarrow$ 1s $^2S_{1/2}$	243.03	51.02

3.3.2 Synchrotron radiation

Photoionization of inner shell electrons or higher order multi-ionization requires higher photon energies than the He gas discharge lamp can deliver. For this reason it typically is necessary to have photons in the soft X-ray spectral region, which ranges from about 100 eV up to a few keV. For this purpose synchrotron radiation facilities based on electron storage rings are used, as they are capable of delivering tunable, monochromatic light in the soft X-ray region. The studies in this thesis that required X-ray radiation were performed at the BESSY II synchrotron radiation facility [40] in Berlin, Germany.

A synchrotron radiation facility takes advantage of the phenomenon where charged particles (electrons) emit radiation upon relativistic acceleration by magnetic fields. In a synchrotron radiation facility, electrons are accelerated to relativistic energies (1.7 GeV at BESSY II [40]), i.e. near the speed of light, and inserted into a storage ring. The storage ring consists of several straight sections (16 at BESSY II [40]) with bending magnets, at the intersection of the straight sections, directing the electrons trajectory around the ring in an approximate circular orbit. The BESSY II storage ring has a circumference of about 240 m, with a period time of about 800.5 ns for the electrons travelling in the storage ring. The straight sections are equipped with insertion devices such as undulators [41], which are arrays of alternating magnetic fields (alternating south and north poles) in the vertical plane. The electrons enter the alternating magnetic field, with a perpendicular velocity to the field lines, which will accelerate then sideways in the horizontal plane in a "wiggle" motion according to the alternation of the field. During the acceleration, which is mainly at the turning points in the wiggle motion, the electrons will emit electromagnetic radiation in the direction of motion. The radiation consists of photon energies corresponding to the magnetic field strength and electron velocity [41].

In the storage ring, the electrons are collectively travelling together as short packets, so called "electron bunches", which ultimately means that the emitted light from the electron path in the undulator will arrive in short pulses separated in time according to the distance between the electron bunches. The light pulse from the undulator is just a few tens of picoseconds long, which is negligible compared to the timing accuracy of the electron time-of-flight in the studies performed in this thesis. The two basic operational electron bunch modes of a storage ring are multi-bunch and single bunch mode, respectively. In multi-bunch mode, the electron

beam current may be divided into several hundred electron bunches circulating the storage ring, resulting in a repetition frequency for the light of hundreds of MHz separated in time by a few ns. In single bunch mode, there is only one electron bunch circulating the storage ring every 800.5 ns, giving a repetition frequency of about 1.25 MHz for the light.

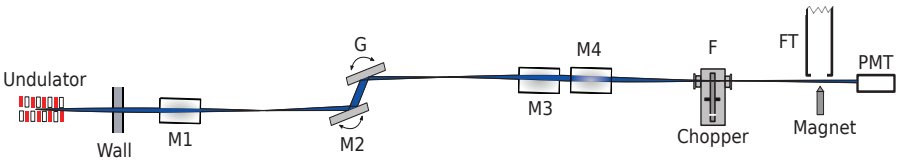

Figure 3.9: Schematic figure of beam line UE52-SGM [42,43] and our experimental set-up at BESSY II. The equipment size, length scales, and angles for the light path are exaggerated for clarity. The mechanical chopper is placed in the focus, F, of the light beam before the interaction region, with the electron flight tube, FT, and photomultiplier tube, PMT.

From the undulator, the light is transported to the experimental set-up by a so-called beamline extended tangentially from the electron storage ring. In this thesis, three different beamlines at BESSY II, providing soft X-ray radiation in the energy range of about 80-1500 eV, have been used for the experiments: UE52 SGM [42,43], U49-2 PGM-1 [44], and UE56-2 PGM-2 [45]. In Fig. 3.9, the schematic layout of a beamline is illustrated, with the most important optical components displayed. When the light from the undulator exits the wall enclosing the storage ring it is collimated by a cylindrical mirror, indicated as M1 in Fig. 3.9, before it is monochromized by a section consisting of a rotatable plane mirror (M2) and rotatable spherical grating (G). The monochromatic light is then focused in the vertical and horizontal planes by a cylindrical (M3) and plane elliptical (M4) mirror, respectively. In our experimental set-up, a mechanical chopper (see section 3.4) is placed at the focus point (F) of the light, to maximize the intensities of the light through to the magnetic bottle TOF-spectrometer. The flux of the light that reaches the experimental set-up, which is directly related to the rate of ionization, may be varied by a adjustable exit slit of the monochromator.

3.4 Mechanical chopper

In coincidence experiments it can often be disadvantageous to have a high repetition rate from the light source, cf. section 3.1. In the case of a several meter long magnetic bottle spectrometer, good conditions for coincidence measurements are obtained at repetition rates of several kHz up to a few tens of kHz, i.e. a frequency below the inverse time-of-flight for near zero kinetic energy electrons. In cases where the repetition rate is too high, e.g. at synchrotron radiation facilities (even in single bunch mode), it may be beneficial to reduce the number of light pulses that reaches

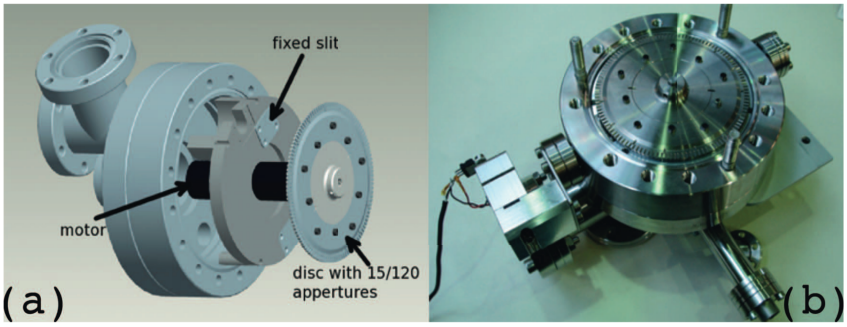

Figure 3.10: Exploded view (a) and photograph (b) of the chopper used in this thesis. Reproduced from Ref. [46], with the permission of AIP Publishing.

the interaction region. In some of the studies in this thesis this was done by a mechanical chopper, which consists of a set of rotating circular discs to chop away a large fraction of the light pulses from the synchrotron radiation storage ring.

The mechanical chopper used in this thesis can be seen in Fig. 3.10 and was originally designed and constructed by S. Plogmaker; the operational principle of the chopper is explained in detail in Ref. [46]. Briefly, this chopper consists of two discs mounted back to back, with a diameter of 100 mm, mounted onto the axis of a small DC motor, operated in vacuum. The light from the storage ring is let through the discs by 110 μm wide apertures, which are milled at fixed intervals around the discs. The number of milled slits determines the final repetition rate of the transmitted light. The present chopper discs has 120 slits on an outer diameter of the discs, and a second set of 15 slits located slightly further in the discs. These two sets of slits gives a light repetition rate of about 80 KHz and 10 KHz, respectively, at a disc rotational frequency of 650 Hz at BESSY II during single bunch mode. The two discs can be rotated, manually by hand, with respect to each other to vary the opening time of the apertures, which in turn affects the amount of light that passes through the chopper. The opening time of the aperture has to be determined by the time between the light pulses from the electron storage ring where the experiment is being conducted at. The opening time should be slightly lower than the time delay between two consecutive light pulses. At a rotational frequency of 650 Hz, the opening time of the aperture is usually about 750 ns [46] while operating at BESSY II, which is a slightly shorter time than a ring cycle for the electrons in the storage ring. Inside the chopper housing, a 40 μm wide fixed slit and a 2 mm round aperture is mounted on the motor housing. The fixed slit partially determines the opening time for the light passing through the chopper [46], and the circular aperture may be used to bypass the chopper obtaining the full 1.25 MHz repetition rate of the light (single bunch mode) at BESSY II.

The entire chopper housing is mounted onto a movable manipulator that can adjust the position of the chopper discs perpendicular to the light beam, which makes it possible to switch between the different slits and the fixed circular aperture. Another important property of this chopper is that it can be phase-locked to the

frequency of the storage ring, which greatly improves the practically achievable duty cycle and thus the consistency of the intensity of the light that gets through the chopper. In a non-phase-locked chopper, only light pulses that randomly arrive at the same time as the opening time of the slits get through, and the opening will not always be central with respect to the light beam, only letting through a fraction of the light pulse intensity.

Chapter 4

Data analysis

The step following measurements is the analysis of the obtained data. The data is structured in such a way that the flight times of all detected electrons or ions, following the absorption of a photon, are listed together as an ionization event. Listing all electrons from an event together makes it possible to study the final products created, and the pathways that lead to them, initiated by the photoabsorption of the sample atom or molecule. Before the time-of-flight data of the electrons can be fully analyzed they need to be converted to electron kinetic energy, which can directly be related to the energy structure of the sample. The first subject this chapter will present deals with the process of converting the raw data from the time-of-flight domain to the kinetic energy or ion mass domain, from calibration measurements using well known samples. The second subject presented in this chapter is an overview of coincidence data analysis used for the studies in this thesis.

4.1 Time to energy conversion

The raw data from the magnetic bottle TOF-spectrometer are obtained as electron flight times relative to the pulses of the ionizing radiation. These data can easily be converted from the time to the energy domain, given that the kinetic energy of an electron trajectory is conserved in a magnetic field. To convert the flight time of an electron to the energy domain, the expression for the kinetic energy is used

$$\mathrm{E}_{kin} = \frac{\mathrm{m_e} v^2}{2} \quad , \tag{4.1}$$

where $\mathrm{m_e}$ is the electron mass and v is the velocity of the electron. The velocity can be written as $v = d/t$, where d is the distance travelled by the electron during the flight time t, which inserted into the expression for the kinetic energy gives the expression

$$\mathrm{E}_{kin} = \frac{\mathrm{m_e} d^2}{2t^2} \quad . \tag{4.2}$$

In reality this expression has to be corrected for experimental factors, such as adjustments due to time delays in the electronics for the recording of the flight times, and for possible energy variations due to electrical potentials present in the interaction region and in the flight path of the electrons. By taking these into account the

expression can be written as

$$\mathrm{E}_{kin} = \frac{\mathrm{m_e}d^2}{2(t-t_0)^2} + E_0 = \frac{D^2}{(t-t_0)^2} + E_0 \quad , \tag{4.3}$$

where t_0 is the correction for time delays in the electronics and cables, and E_0 is the correction to the energy from possible electrostatic potentials that may introduce a positive or negative acceleration to the electrons. The parameter $D^2 = m_e d^2/2$ is introduced to simplify the expression. The parameters D, t_0, and E_0 can be accurately determined for a specific set-up of the spectrometer, by least square fits to measurements of very well known samples.

4.2 Calibration of electron spectra

As mentioned, calibration of the electrons' flight times is obtained from measurements on very well known samples. Typically, noble gases (Ne, Kr, Ar, Xe) and simple molecular samples, such as O_2, N_2, and CO_2 are used. The calibration samples are chosen based on the range of electron kinetic energies that are of interest in the specific study, and if a large energy range is of interest, calibration with several samples may be necessary over a large range of photon energies. The basic principle of the calibration is to match peaks in the time-of-flight data with their respective known kinetic energy values. In the following sections this procedure is exemplified for a few samples, which have been widely used for calibration of the data included in this thesis.

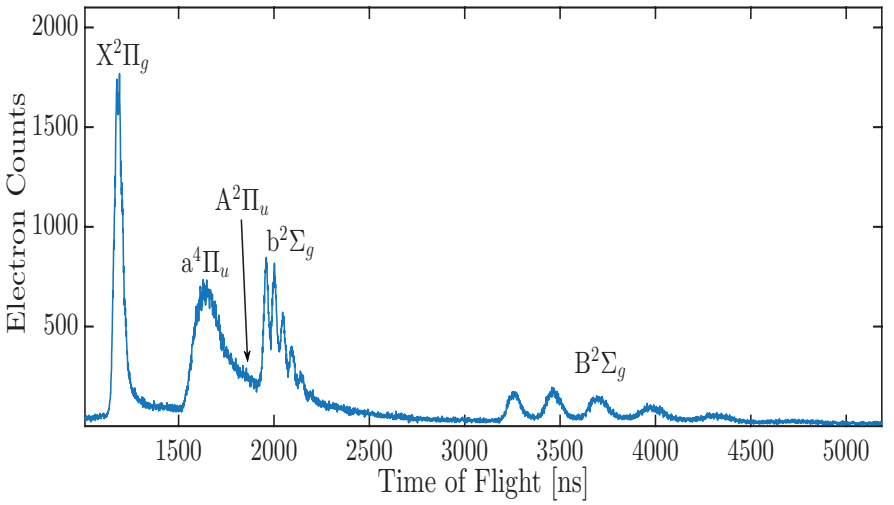

Figure 4.1: Valence photoelectron spectrum of molecular oxygen at a photon energy of 21.22 eV.

4.2.1 Calibration with oxygen

The oxygen (O_2) valence photoelectron spectrum [47] is well known and contains resolvable vibrational structures, which makes it a well suitable sample for both resolution optimization and calibration utilizing the He Iα emission line (21.22 eV) from the He gas discharge lamp. The binding energies for the valence states, that are reachable by the He Iα line, in singly ionized O_2 ranges from about 12 eV for the singly ionized ground state up to about 21 eV for the $B^2\Sigma_g$ excited state [47]. The O_2 spectrum in the time domain recorded with the electron only set-up (see section 3.2.2), at the He Iα line, is displayed in Fig. 4.1.

The most intense peaks in the states that can be seen in Fig. 4.1, which usually are used for the calibration with oxygen, are listed in Table 4.1. The time-of-flight calibration to the energy domain is performed by plotting the time-of-flight values of the peaks in the spectrum versus their respective kinetic energy, which are obtained from the photon energy minus the binding energy of these states [47]. This can

Table 4.1: Kinetic energies and binding energies of the most intense peaks in the valence photoelectron spectrum of molecular oxygen shown in Fig. 4.1, following the literature values of Ref. [47].

State	vibrational level	Binding energy (eV)	Kinetic energy (eV)
$X^2\Pi_g$	1	12.3	8.92
	2	12.5	8.72
$a^4\Pi_u$	3	16.47	4.75
	4	16.59	4.63
	5	16.70	4.52
	6	16.82	4.40
	7	16.93	4.29
	8	17.03	4.19
	9	17.14	4.08
	10	17.24	3.98
$b^4\Sigma_g$	0	18.17	3.05
	1	18.32	2.90
	2	18.45	2.77
	3	18.59	2.63
	4	18.72	2.50
	5	18.85	2.37
$B^2\Sigma_g$	0	20.30	0.92
	1	20.43	0.79
	2	20.57	0.65
	3	20.69	0.53
	4	20.82	0.40
	5	20.93	0.29

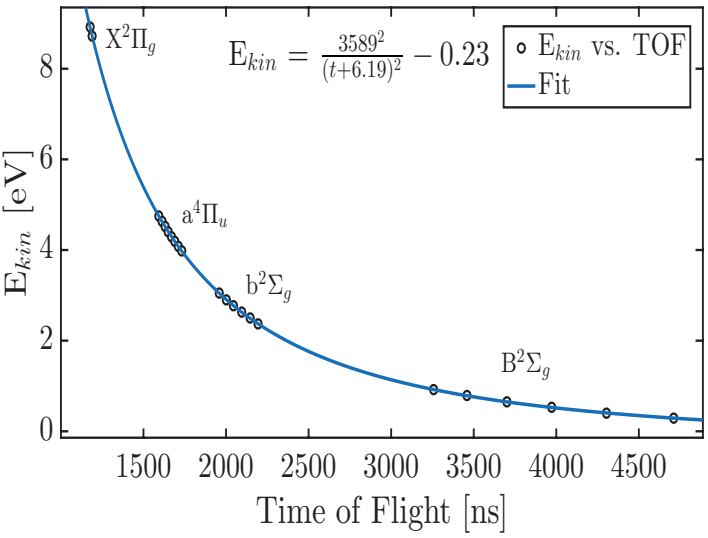

Figure 4.2: Calibration with molecular oxygen at 21.22 eV.

be seen in Fig. 4.2 for the O_2 spectrum displayed in Fig. 4.1. The values of the calibration parameters D, t_0, and E_0 are obtained from the figure by least square fitting of Eq. 4.3 to the peak values. Typical values for the calibration parameters of the 2.2 m long instrument used in this thesis are $D \approx 3600$, t_0 equal to a few tens of nanoseconds, and E_0 that is between -1 to 0 eV.

4.2.2 Calibration with noble gases

For calibration of electrons with higher kinetic energies, for example at synchrotron radiation facilities, it is usually not sufficient to use only valence ionization. Instead, photoionization of inner-valence and core orbitals in noble gas atoms resulting in Auger decay may be more suitable for calibration reference spectra. For example when photoionizing the krypton $3d_{5/2}$ and $3d_{3/2}$ orbitals at 93.79 eV and 95.04 eV [49, 50], respectively, a well known Auger spectrum is produced when the 3d vacancy decays [48]. This is presented in Fig. 4.3, in the time domain, for an ionization spectrum of Kr recorded at a photon energy of 110 eV. The kinetic energies of the numbered peaks in Fig. 4.3 are obtained from the known state energies in Refs. [48–50], and are presented in Table 4.2. At a photon energy of 110 eV, the photoelectrons from the 3d orbitals (lines 15 and 16) will have a kinetic energy of 16.21 eV and 14.96 eV, respectively, and the Auger electrons (lines 3-14) will have kinetic energies ranging from about 24 eV up to about 54 eV. At 110 eV, the ^{2}P (line 1) and ^{2}S (line 2) valence states with a binding energy of about 14.6 eV and 27.51 eV [49, 50] are also present in the ionization spectrum with kinetic energies of about 95.8 eV and 82.49 eV, respectively.

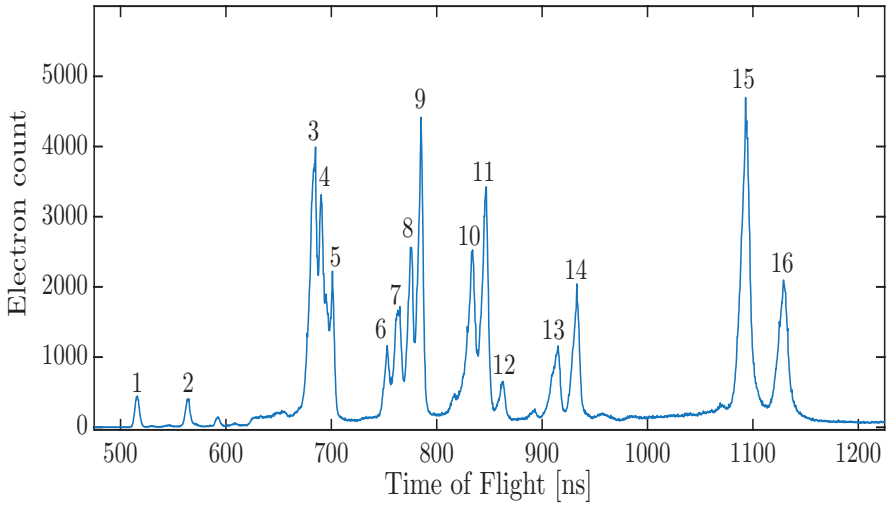

Figure 4.3: Krypton Auger and photoelectron lines recorded at 110 eV photon energy. The best resolved lines are numbered and listed in Table 4.2.

Table 4.2: Krypton Auger and photoelectron lines [48]. Lines from Fig. 4.3 with their respective electron kinetic energy.

Line	Energy (eV)	Line	Energy (eV)
1	95.80	9	37.84
2	82.49	10	32.35
3	54.85	11	31.11
4	53.61	12	29.60
5	51.33	13	25.45
6	42.31	14	24.20
7	41.07	15	16.21
8	39.08	16	14.96

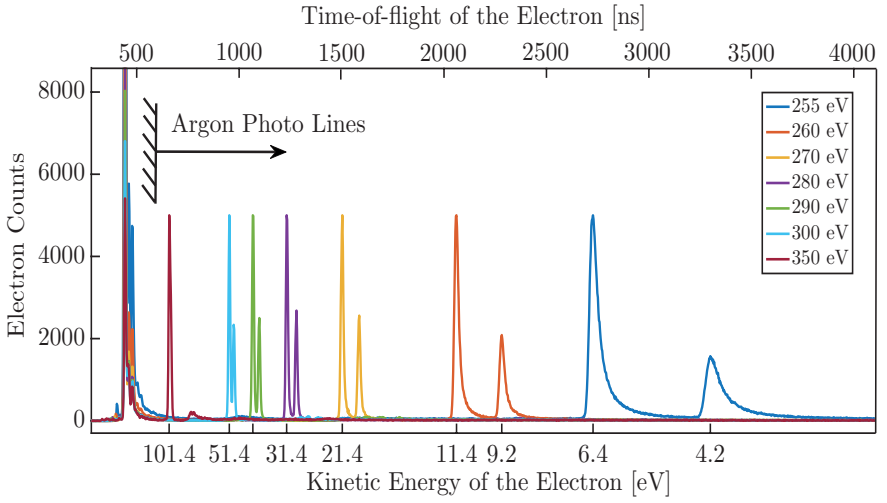

Figure 4.4: Argon 2p photoelectron lines at photon energies in the range 255-350 eV. The top horizontal axis shows the TOF scale and the bottom horizontal axis shows the kinetic energy scale for the electron.

Another sample that may be used for calibration is argon ionized from its $2p_{3/2}$ and $2p_{1/2}$ orbitals with ionization energies of 248.63 eV and 250.78 eV [49,50], respectively. By increasing the photon energy step-wise, several photoionization spectra can be recorded with the photoelectron lines at different kinetic energies. This can be seen in Fig. 4.4, where the 2p photoelectron lines have been recorded at seven different photon energies between 255 to 350 eV.

4.3 Ion mass/charge calibration

Similar to the raw data of the electrons, the raw ion data are recorded as flight times of the ions, which often need to be converted to a more useful quantity before a full analysis can be made. The flight times depend on the mass and charge of the ions, which can be understood from the potential energy, $E_p = qU$, of an ion with charge q in an electric field U. The potential energy of the ion is converted to kinetic energy, E_k, as it is accelerated into the flight tube, which means that the expressions for the kinetic and potential energy can be set as being equal

$$\mathrm{E_p} = \mathrm{E_k} \Rightarrow qU = \frac{mv^2}{2} \quad , \tag{4.4}$$

where v is the velocity after acceleration, and m is the mass of the ion. Writing the velocity as $v = d/t$, where d is the distance travelled, during the time t, through the field-free region in the flight tube, gives the relation

$$q\mathrm{U} = \frac{m}{2}\left(\frac{d}{t}\right)^2 \Leftrightarrow t = \frac{d}{\sqrt{2\mathrm{U}}}\sqrt{\frac{m}{q}} \quad . \tag{4.5}$$

This is the expression for the flight times for an ion with a specific mass and charge, accelerated by an electric potential. This can be simplified by the introduction of the constant $k = d/\sqrt{2U}$, and possible time delays in the electronics and cables can be taken into account by adding a parameter t_0, resulting in the final expression

$$t = t_0 + k\sqrt{\frac{m}{q}} \quad . \tag{4.6}$$

This expression assumes that the ions have zero initial velocity after the dissociation process. To calibrate the flight times of the ions to their respective mass/charge ratio, the parameters k and t_0 have to be determined. The calibration parameters can be determined from least square fitting of ion time-of-flight peaks of known ion species, according to their respective mass and charge.

4.4 Coincidence analysis

4.4.1 Electron coincidence analysis

The basic objective of coincidence analysis of data from ionization events is to find correlated events, and to identify the underlying processes. Examples of processes that may be revealed in multi-electron coincidence analysis are the kinetic energy relations between the electrons released from the sample atom or molecule. The coincidence data can be seen as a multidimensional function, where the arguments are the detected electrons with a multifold of time-of-flight or energy values. In this view, the multidimensional function will represent the coincidence counts in a so called *coincidence map*. The most basic type of coincidence map is in the case of a three dimensional coincidence function, which can be represented in a two dimensional coincidence map. An example of a two dimensional coincidence map can be seen in Fig. 4.5, where a data set of two electrons have been plotted against each other in the time-of-flight (a) domain and in the kinetic energy (b) domain, respectively. The coincidence maps are plotted with the first arriving electron to the detector on the x-axis and the second arriving electron on the y-axis. Plotting the data of two electrons in this way will show intensity fluctuations in the map, which may reveal the underlying processes in the ionization event.

In Fig. 4.5 (a), the raw time-of-flight data of electron pairs have been plotted in form of a coincidence map. From such a plot it is possible to get a first preliminary understanding of the processes happening at a specific photon energy. Electron pairs with nearly the same flight time, and therefore also nearly the same kinetic energy, will end up somewhere along the diagonal line cutting the coincidence map at an approximate 45° angle relative to the horizontal axis, given that the axes are symmetric. The angle is only approximately 45° because of a small "dead time" in the MCP detector where overlapping electron signals are indistinguishable, and will therefore be registered as only one electron arriving at the detector. The dead time is usually 10-50 ns from when the first electron hits the detector. For an unequal amount of kinetic energy between the electrons, which was discussed in section 2.2, they will end up further away from this diagonal. In the case of direct double electron

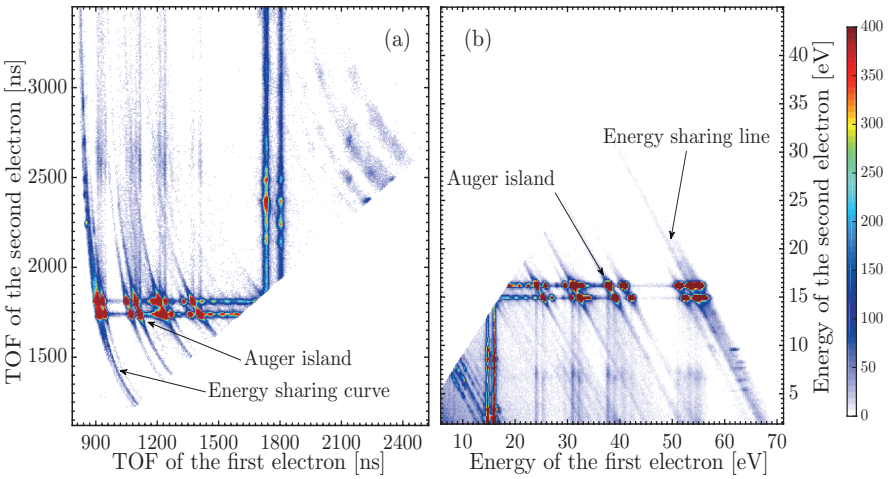

Figure 4.5: Coincidence maps of Kr in the time (a) and kinetic energy (b) domain, measured at 110 eV photon energy. The color scale is in the units of coincidence counts.

processes, an electron pair will share a total amount of kinetic energy released in the direct process, which will constitute hyperbolic curves representing the direct ionization event. The hyperbolicity of the energy sharing curves comes from the inverse square relation of the time-of-flight and kinetic energy in equation 4.3. The hyperbolic energy sharing curves can be seen in Fig. 4.5 (a), where each curve represents a doubly ionized final state in the sample. Indirect processes will end up as straight lines or as "islands", in the coincidence map. For example electrons from a single Auger decay event will have well defined kinetic energy related to the specific orbital it was emitted from, and they will always be in coincidence with a photoelectron with a well defined kinetic energy determined by the photon energy. This will result in "islands" of coincidence counts in the map with well defined flight times for both the first and second arrival electron. In Fig. 4.5 (a), so called "Auger islands" can be seen as high intensity areas in the coincidence map revealing the indirect nature of these processes.

The coincidence map in Fig. 4.5 (b) is in the kinetic energy domain, where the electron pair time-of-flight data have been converted to energy according to formula 4.3 in section 4.1. The processes that are revealed in Fig. 4.5 (a) are also revealed in the coincidence map in (b), but can now be directly correlated to the kinetic energy of the electrons and therefore also directly to the energy structure in the atomic or molecular system. The energy sharing between two electrons will, instead of hyperbolic curves, now be displayed as diagonal lines due to the $E_{kin} \propto 1/t^2$ relation of the kinetic energy. A result from the non-linear conversion between the time and energy domain is that there will be a squeezing effect in the energy domain for electrons at longer flight times, and the opposite for electrons at shorter flight times. This can be seen in Fig. 4.5 where the energy sharing curve at the shortest

flight times (of the first electron) in (a) is broadened as it is converted to energy in (b). At short flight times this will result in a squeezing effect, of not only the real coincidence counts, but also the background noise giving the appearance of a higher background level at shorter flight times, which can be seen in Fig. 4.5 (b) below a kinetic energy of 10 eV for the first electron.

Coincidence maps can represent the data in various other forms. For example, the maps can represent the excess energy of the electrons, which is the kinetic energy sum of both electrons in the electron pair, on one of the axes, and the energy of any of the electrons on the other axis. In this type of map, straight lines will correspond to particular dicationic final states formed by direct photoionization. Coincidence maps may also be used to analyze higher order multi-ionization processes, in multiple permutations of different coincidence maps that may reveal how all electrons from an ionization event correlate. In this way it is possible to also select an energy interval of, for example, a photoelectron and plot the spectrum of the correlated electron(s) from processes directly related to the photoelectron. This method is highly useful while analysing, for example, double Auger decay data, where the selection of a coincident photoelectron is expected to result in a cleaner double Auger spectrum.

4.4.2 Ion coincidence analysis

Ion data may reveal information on fragmentation dynamics upon dissociation of molecules in multiparticle coincidence experiments [51], for example, as the result of the decay of a core vacancy. In this thesis, ion fragmentation data have been used to complement the electron data in some of the studies. As an example in Paper II ion fragmentation data provided information on the electron spectra in coincidence with the respective fragments upon dissociation of D_2O from photoionization of valence and inner-valence states. These kinds of studies are usually referred to as photoelectron-photoion-coincidence (PEPICO) studies in the case of single ionization, and can, for example, be expanded to higher order photoelectron-photoion-photoion-coincidence (PEPIPICO) in the case of double ionization etc. [20].

In higher order PEPIPICO studies coincidence maps are very useful in the analysis of the coincidence data, including both electrons and ion fragments upon dissociation. In these processes, the spread of flight times and the shape of the islands in the coincidence map produced by ion pairs may reveal valuable information on the fragmentation dynamics [20, 51]. Ions in coincidence with electron data can be used to eliminate the number of false coincidences, and to separate overlapping electron processes that are known to be related to a specific ion fragment(s). A drawback of this method is that the collection-detection efficiency of ions are usually much lower than for electrons (see section 3.2.3), which requires substantially longer acquisition times for reasonable electron and ion coincidence statistics.

Chapter 5

Results

5.1 Double valence ionization of methyl halides

Studies of multiple ionization of molecules in the gas-phase by photons with energy below the threshold for inner shell ionization, where Auger decay processes are energetically impossible, provide valuable information on ionization processes that are highly relevant to electronic structure theory. The double ionization processes in the valence region of molecules provide important information on dissociation mechanisms in high-energy environments, with direct relevance to mass spectrometry experiments, and environments of astrophysical and atmospheric significance. The most basic parameter determining the rates and occurrence of molecular dissociation processes is the lowest double ionization potential (DIP), while the whole DIP spectrum is vital for the interpretation and understanding of the details and mechanisms driving the dissociation. The results presented in Paper I are based on measurements of single-photon double valence ionization of methyl halides (CH_3F, CH_3Cl, and CH_3I), and the interpretation of the spectra obtained relies on previous ionization data, Auger electron spectra, and theoretical investigations.

All of the methyl halides have the same spatial structure and symmetry (the C_{3v} point group), which means that the ground state electron configuration will be similar to the form: [inner atomic orbitals]$1a_1^2 2a_1^2 1e^4 3a_1^2 2e^4$ ($^1A_1$), where the HOMO has a more dominant lone-pair character as the mass of the halogen moiety increases. The outermost orbital character is slightly different for CH_3F than for the other methyl halides because the outermost atomic p-orbital in fluorine has a higher binding energy than the outermost atomic p-orbital in carbon, whereas the opposite is true for the other methyl halides. This means that the outermost orbital in CH_3F has a stronger methyl (CH_3) character than the other methyl halides.

5.1.1 Methyl fluoride

The measured double valence photoelectron spectra of CH_3F are displayed in Figs. 5.1 and 5.2. In Fig. 5.1, the coincidence signal intensity is plotted versus the double ionization energy measured at 48.37 eV photon energy, and in Fig. 5.2 related spectra are plotted for the photon energies of 100 eV and 130 eV. The lack of structure in the DIP spectrum in Fig. 5.1 is expected due to the lack of lone-pair character of the HOMO, which is evident form the broad ionization bands in the single ionization

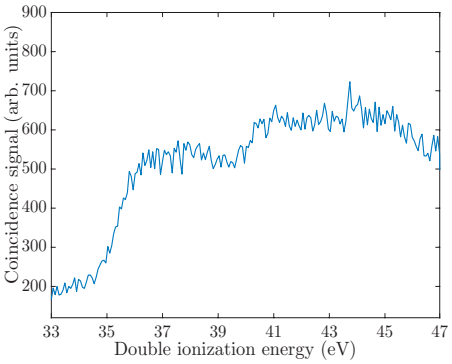

Figure 5.1: Double photoionization spectrum of CH_3F at 48.37 eV photon energy.

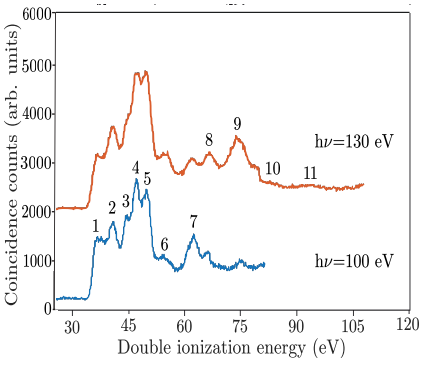

Figure 5.2: Double photoionization spectrum of CH_3F at 100 eV (blue) and 130 eV (red) photon energy.

spectrum of CH_3F [52]. The lack of vibrational structure in the DIP spectrum may also indicate that methyl fluoride has no bound or metastable doubly charged states accessible by photoionization, which is confirmed by the lack of doubly ionized parent ions in the mass spectrum of CH_3F [55]. One of the main results from Fig. 5.1 is an estimate of the lowest double ionization energy of around 35.0 eV by interpolation of the slope of the spectrum down to the base level of the background coincidence signal. Another feature that can be seen in the spectrum is the broad band between 35 eV and 39 eV, which can be interpreted with the help of theoretical calculations by Liegener [53] who found two states with the leading $2e^2$ electron configuration in this energy region. The leading $2e^2$ electron configuration, in the C_{3v} symmetry, formally produces the states $^3A_2$, ^1E and $^1A_1$. Liegener calculated the two singlet states to be at ionization energies of 35.8 eV and 36.3 eV, respectively. The triplet state will be close to the singlet states and probably lower in energy. The next broad

Table 5.1: Double ionization energies of CH_3F.

State	Ionization energy (eV) This work	Others	Leading configuration[d]
Onset	35.0[a] ±0.19	35.2[b]	
$^3A_2$, ^1E, $^1A_1$	36.0	35.8[c]	$2e^2$
		36.3[c]	
	40.7	39.7[c]	$5a_1^1 2e^3$
		41.4[c]	$1e^3 2e^3$

[a] Onset value for the lowest double ionization from Fig. 5.1, and the estimated standard deviation for the onset.
[b] Onset value for the lowest double ionization from Ref. [54].
[c] Obtained from theoretical calculations presented in Ref. [53] with their numbering of the orbitals.

peak that can be interpreted by the calculations is the one centred around 41 eV. This peak may stem from states associated with the two configurations $5a_1^1 2e^3$ and $1e^3 2e^3$ with the energies 39.7 eV and 41.4 eV, respectively.

Table 5.2: Ionization energies (in eV) for the peaks numbered in the CH_3F^{2+} spectra recorded at 100 eV and 130 eV shown in Fig. 5.2.

Peak:	1	2	3	4	5	6	7	8	9	10	11
Energy:	36.4	40.7	44.2	46.4	49.3	54.2	62.1	65.7	73.6	82.2	98

The DIP spectra in Fig. 5.2 show more broad structures as they range to higher lying doubly charged states. The peaks numbered in the spectra are listed in Table 5.2. A heavy mixing of electron configurations at energies above 41 eV makes a simple identification of more states difficult with exception of the weak broad peak that can be seen at about 98 eV, which is understood in terms of double ionization of almost pure F 2s orbital [56].

5.1.2 Methyl chloride

The measured double valence photoelectron ionization spectra of CH_3Cl at the photon energies 40.81 eV and 48.37 eV are presented in Fig. 5.3. The lowest double ionization energy in CH_3Cl may be estimated to about 30.6 eV, most evidently from the spectrum recorded at 40.81 eV photon energy. The remaining part of the CH_3Cl spectra shows broad structures with peak maxima at 31.8 eV, 35.1 eV, 39 eV, and 41 eV, which can be interpreted from the previous experimental and theoretical work by Grant et al. [57]. The ionization energies of the valence states and the leading electron configurations of these peaks are summarised in Table 5.3.

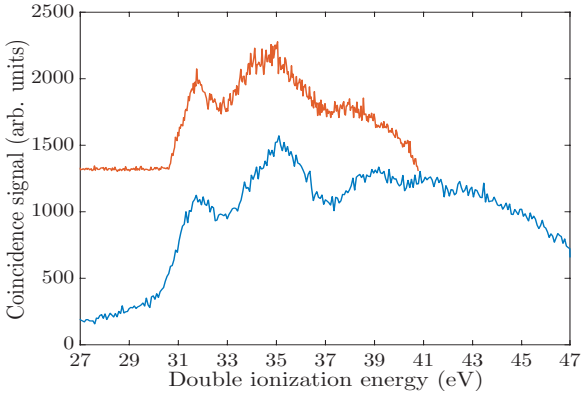

Figure 5.3: Double photoionization spectra of CH_3Cl at 40.81 eV (red) and at 48.37 eV (blue) photon energy.

Table 5.3: Double ionization energies of CH_3Cl.

State	Ionization energy (eV)		Leading configuration[a]
	Others[a]	This work	
Onset		30.6[b] ±0.14	
$^3A_2$	31.5 ±0.2	31.8[c]	$2e^2$
^1E	32.2 ±0.2		
$^1A_2$	33.6 ±0.3	35.1[c]	$1e^3 2e^3$
^3E	34.1 ±0.2		
^1E	35.4 ±0.3		$3a_1^1 2e^3$
$^3A_2$	35.5 ±0.3		$1e^3 2e^3$
^1E	38.5 ±0.3		$1e^3 2e^3$
^3E	39.0 ±0.3	39[c]	$1e^3 3a_1^1$
$^3A_2$			$1e^2$
^1E	40.4 ±0.3	41[c]	$1e^2$
^3E	41.0 ±0.3		$2a_1^1 2e^3$

[a] Experimental values and leading configurations from Ref. [57].
[b] Onset value for the lowest double ionization energy from Fig. 5.3. The standard deviation is estimated from the 40.8 eV measurement.
[c] Features in Fig. 5.3 with peak maxima at the energies given.

5.1.3 Methyl iodide

TOF-PEPECO measurements on CH_3I have previously been carried out by Pilcher-Clayton and Eland [58], at a photon energy of 40.8 eV. In paper I, the spectrum of CH_3I at 40.8 eV is complemented by additional measurements at 48.37 eV, which are in turn interpreted by previous theoretical investigations of Pernpointner et al. [59]. The double ionization spectra of CH_3I measured at 40.81 eV and 48.37 eV

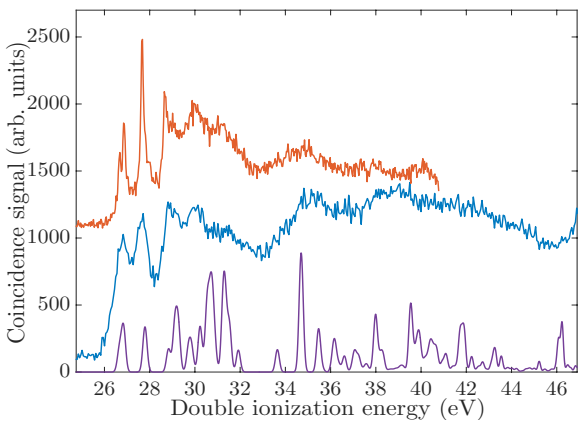

Figure 5.4: Double photoionization spectra of CH_3I at 40.81 eV (red) and 48.37 eV (blue) photon energies. The purple line is a theoretical spectrum explained in the main text.

Table 5.4: Values for the double ionization of CH_3I.

State			Ionization energy (eV)		Relative peak intensity	
Term		Level	Others	This work	40.81 eV	48.37 eV
$^3A_2$	A_1	$v = 0$	26.664[a]	26.67 ± 0.20[c]	39	64
	E	$v = 0$	26.846[a]	26.85	55	72
		$v = 1$	26.998[a]			
^1E		$v = 0$	27.656[a]	27.68	100	85
		$v = 1$	27.778[a]			
		$v = 2$	27.9[b]			
$^1A_1$		$v = 0$	28.679[a]	28.68	72	92
E[b]				29.05	58	88
Mainly I character				30.0[d]	65	88
I and CH_3 character				31.2[d]	54	76
Mainly CH_3 character				34.8[d]	43	100

[a] Experimental values from Ref. [58].
[b] Suggested in Ref. [59].
[c] Estimated standard deviation for the 40.8 eV measurement.
[d] Maximum of the broad bands in Fig. 5.4.

photon energy are displayed in Fig. 5.4. The spectra of CH_3I show more structural features than the other two methyl halides due to the high lone pair character of the outermost valence orbital [52]. The states and vibrational levels represented by the first features of the double ionization spectrum of CH_3I were previously interpreted in Ref. [58] from the measurement at 40.81 eV, and are given in Table 5.4. The states above 29 eV have highly mixed configurations as suggested by the theoretical calculations of Pernpointner et al. [59]. From these calculations it is possible to interpret the broad peak centred at 30.0 eV to be of mainly iodine character, and as the energy increases the spectrum starts to show a more CH_3 character. This is seen from the broad peaks at 31.2 eV and 34.8 eV, which show a mixture of I and CH_3 character and mainly CH_3 character, respectively. At even higher double ionization energies, there are heavily mixed states and the bands in the spectra are too diffuse for a simple classification of the final states observed.

The purple line in Fig. 5.4 is a convolution of Gaussian curves with the theoretical spectrum calculated by Pernpointner et al. [59]. The Gausian curves in the spectrum have a varying full width half maximum as a function of the electron kinetic energy, which is chosen to match the instrumental kinetic energy resolution of $E/\Delta E \approx 50$ (see section 3.2.2). The calculated spectrum has been shifted to higher energies by 0.84 eV, to align the first peak in the theoretical spectrum with the experimental spectrum. It has to be noted that the intensities in the theoretical spectrum can not be compared to the experimental spectrum, only the energy values of the peaks may be compared. The calculated spectrum shows a good agreement in terms of energies with the experimental spectrum, which is seen in more detail in Ref. [59].

5.1.4 Coulomb repulsion between the double vacancies

The methyl halides are interesting systems to test the empirical rule-of-thumb for the lowest DIP in molecules of Molloy et al. [9], $E_{DIP} \approx 2.2 \cdot E_{IP} + 11.5/r_{hh}$ (see section 2.2). They possess similar symmetry but with a changing character of the outermost valence orbital from bonding character in methyl fluoride to lone-pair character in methyl iodide. The rule-of-thumb was originally conceived for molecules with distinct atomic sites, without any spin-orbit splitting at which the vacancies may be located. The large spin-orbit splitting in CH_3I makes it inappropriate to use the first peaks for the calculation of the vacancy distance from the rule-of-thumb. The lowest vertical single ionization energy is therefore taken as the average energy between the spin-orbit splitting [60], and the ^1E state is taken as the lowest vertical double ionization energy as it best represents the configuration, that for the ionization energy discounting the spin-orbit splitting (see Paper I for more details).

The intercharge distances deduced from the rule-of-thumb are consistent with the expectation that the charge separation in the dication will be more marked than the orbital delocalization in the neutral molecule, due to Coulomb repulsion. Table 5.5 lists the vertical single and double ionization energies used for testing the rule-of-thumb, and the corresponding vacancy separations obtained. By comparison of the charge separation in the methyl halides to the interatomic distances [61] between the carbon and halogen atoms it is apparent that the distance is 113% of the C-F bond length in CH_3F, 97% of the C-Cl bond length in CH_3Cl, and only 89% of the C-I bond length in CH_3I. The lower percentage in the case of CH_3I may be because of the strong localization of the outermost electrons for the neutral molecule. Although the application of the rule-of-thumb to the methyl halide systems may not be completely justified, it still gives reasonable results which seem to agree with the character of the outermost orbital in the methyl halides.

Table 5.5: Values for the vertical single (IP_v), and double (DIP_v) ionization energies used in the calculations of the rule-of-thumb. The onset values of the lowest double ionization potentials (DIP_{on}) for the methyl halides are also listed. The vacancy distance, r_{hh}, obtained from the rule of thumb may be compared to the neutral molecular bond distance, r_{c-x}.

Sample	IP_v (eV)	DIP_v (eV)	DIP_{on} (eV)	r_{hh} (Å)	r_{c-x} (Å)
CH_3F	13.04[a]	36.0	35.0	1.57	1.39[b]
CH_3Cl	11.29[a]	31.5	30.6	1.73	1.78[b]
CH_3I	9.85	27.66	26.5	1.91	2.14[b]

[a] Values for the vertical single ionization energy from Ref. [60].
[b] Interatomic distances from Ref. [61], rounded to two decimals.

5.2 Dissociation upon valence or core photoionization

The dissociation processes of molecules upon ionization are closely related to the energy that is added to the system in the ionization event. To obtain a complete understanding of the processes, both experimental and theoretical investigations are needed. Some of the interesting questions regarding the dissociation dynamics are: What fragments are formed by the dissociation process? At what ionization energies are specific fragments formed and to what extent? Which pathways do the dissociation processes go through? In Paper II, these questions are investigated for outer valence and inner-valence photoionization of heavy water (D_2O), from energy selected and mass-resolved electron-ion coincidence measurements. In this work, the dissociation of heavy water from the B- and C-states are examined with the in-line tandem electron-ion coincidence spectrometer (see section 3.2.3). This allows us to reveal minor fragmentation pathways of the B-state and to examine the fragmentation of the C-state more comprehensively than what was achieved in previous studies.

For multiply charged molecular systems that are created upon core photoionization, there are further questions concerning the dissociation dynamics: Are there any molecular neutrally charged fragmentation products? How are the charges transferred between the atoms in the molecule as it dissociates? To what extent does the location of the initial core hole play a role? These questions are investigated in Paper III, where the dissociation of multiply charged iodine cyanide (ICN) by Coulomb explosion has been studied by multi-electron-multi-ion coincidence spectroscopy with the perpendicular electron-ion coincidence spectrometer set-up (see section 3.2.4).

5.2.1 Dissociation of D_2O upon valence ionization

Water (and heavy water) cations have mainly four valence and inner-valence electronic states, X^2B_1, A^2A_1, B^2B_2, and C^2A_1, with the vertical ionization energies of 12.6, 15, 19, and 32 eV above the ground state of the neutral molecule [62–65]. In Paper II the decay of the B^2B_2 and C^2A_1 states in D_2O^+ are investigated by mass-resolved photoelectron spectra measured at 21.22 eV and 40.81 eV, for the different states. The dissociation patterns of H_2O and D_2O are, despite the isotopic discrepancy, considered to be essentially the same, which may be seen from previous studies comparing the two [66, 67]. The photoionization of neutral D_2O to the B-state ranges from 17.3 eV to 20.5 eV, which can be seen in Fig. 5.5 displaying the mass-resolved photoelectron spectrum of the B-state. This energy range encompasses the enthalpy of formation (0 K) of $OD^+(X^3\Sigma^-)$ at 18.07 eV, $D^+ + OD(X^2\Pi)$ at 18.67 eV, and $O^+(^4S) + D_2$ at 18.71 eV [67]. Further decay pathways may be reached in the extended tail above the main energy region of the B-state, with thresholds at 20.26 eV for $OD^+(a^1\Delta)$ [68], at 20.61 eV for $D_2^+ + O(^3P)$ [70], and at 21.6 eV for $OD^+(A^3\Pi)$ [69]. From Fig. 5.5 it can be seen that the ionic fragments appear at or very near the thermodynamic thresholds. The dynamics of the dis-

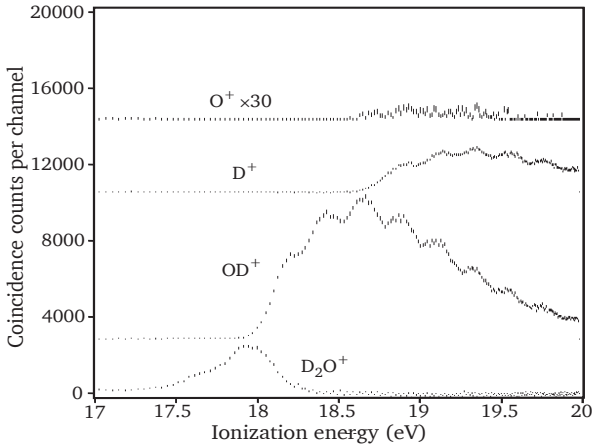

Figure 5.5: Photoelectron spectra of the B^2B_2 state of D_2O, taken at 21.22 eV photon energy, in coincidence with product ions.

sociation of D_2O from the B-state have been thoroughly investigated and discussed theoretically several times [71–75], and it has been shown that the fragmentation channels $OD^+ + D$ and $OD + D^+$ are strongly coupled to specific dissociation pathways, going through the A- and X-states. From these investigations it is clear that the B-state has a very short lifetime of possibly 10 fs [75], before it decays to either the A-state, via a conical intersection between the potential energy surfaces of the B- and A-states, or directly to the X-state. The B-state may also indirectly reach the X-state, through Renner-Teller coupling between the A- and the X-state, which is directly correlated to the dissociation pathways that leads to the creation

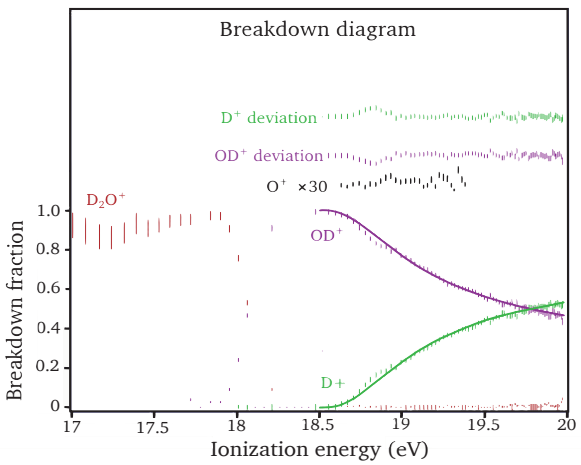

Figure 5.6: Breakdown diagram derived from the data shown in Fig. 5.5.

of OD^+ + D [71–75]. The formation of OD^+ + D may also be reached by spin-orbit transition from the B-state to a highly dissociative quartet a-state through another conical intersection [75]. The dissociation pathways leading to the creation of OD + D^+ are directly correlated to the A-state in an adiabatic picture [71–75]. The lowest vibrational levels in the B-state may survive as an intact D_2O^+ ion, with a lifetime of about 198 μs [76].

Measurements with photon energies at the HeIβ, HeIIα, and HeIIβ emission lines show, consistently, a relative ion production with the intensities: D_2O^+ 10±2%, OD^+ 70±3%, D^+ 19±2%, O^+ 0.15±0.05%, and D_2^+ 0.1±0.05%. These intensities are in good agreement with the values for the dissociation of the B-state in H_2O [75, 77]. The data shown in Fig. 5.5 are represented as a breakdown diagram in Fig. 5.6. The breakdown for the OD^+ and D^+ fragments are contrasted by smooth curves generated by the simplest form of Rice-Ramsperger-Kassel (RRK) theory [78] for the rate constant for competing dissociations, j, with threshold energies E_{0j},

$$k_j = R_j \left(1 - \frac{E_{0j}}{E}\right)^{s-1} \quad , \tag{5.1}$$

where E is the total energy, R_j is a characteristic rate constant for each reaction, and s is an effective number of harmonic oscillators present in the molecule (classically the number of vibrational modes). A good fit of the RRK theory to the data is obtained with $R_D = 3R_{OD}$ and s = 3.8 (solid lines in Fig. 5.6). The deviation curves in Fig. 5.6 are obtained from subtraction of the theoretical from the experimental curves. The shape of the breakdown diagram is the same as previously reported [67, 79, 80], but with some important differences; the statistics are substantially improved which reveals the clear existence of modulations in the breakdown curves for OD^+, D^+, and O^+. The clearest modulation in the D^+ deviation from the smooth curve can be seen at 18.8 eV ionization energy, with a corresponding dip in the fraction of OD^+. A second weak modulation in the deviation curves may be discerned at about 19.25 eV. The modulation in the O^+ breakdown curve has a first peak maximum at 18.9 eV. The modulation corresponds to a lower cross-section for the formation of OD^+ at the specific vibrational level located around 18.8 eV, either because of a hindered coupling between the A- and X-state at this particular vibration level or because of a smaller coupling between the B- and a-state. The existence of these modulations leads to the main conclusion that the fragmented system retains some memory of the original vibrational excitation before the dissociation pathway is irreversibly chosen.

The photoionization of D_2O to the C^2A_1 state starts at about 30 eV photon energy, which can be seen in Fig. 5.7 displaying the mass-resolved photoelectron spectra of the C-state. We observe here that the D_2O^+ ion in the C-state dissociates into D^+ and O^+ fragments, but also into OD^+ ions to a considerable extent, which was not observed in the previous study on H_2O by Tan et al. [77]. The OD^+, O^+, and D^+ ionic fragments formed in the dissociation of the C-state are released with a relatively high kinetic energy, most probably because of the high excess energy available (~9-14 eV) for the forming of the ground-state singly charged ionic products. The high kinetic energy release may suggest that O^+ and D^+ are products of sequential dissociation pathways of initial OD or OD^+, formed from the first O-D

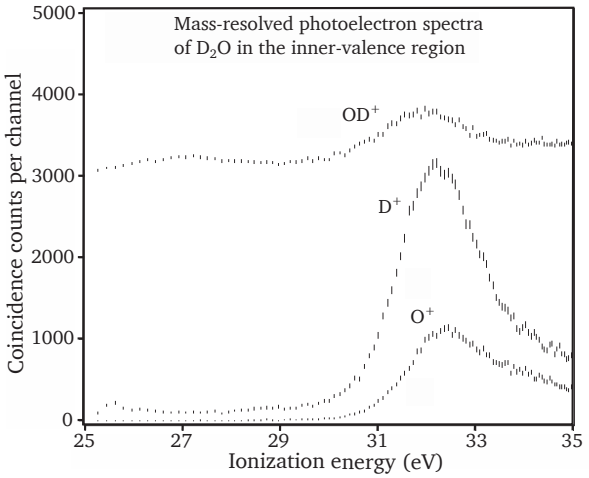

Figure 5.7: Photoelectron spectra of the C^2B_2 state of D_2O, taken at 40.81 eV photon energy, in coincidence with product ions.

bond breakage. Further clues for the mechanism may be given by the Cold target recoil ion momentum spectroscopy (COLTRIMS) study of Sann et al. [81] on dissociation of water into doubly charged products. The estimated relative abundance of the fragment branching from the dissociation from the C-state are 16% for OD^+, 24% for O^+, and 60% for D^+. The fragmentation branching ratios are given in Table 5.6, together with the kinetic energy release (KER) and the maximum available energy for the formation of the singly charged products. The complete lack of D_2^+ dissociation products in the ion mass spectrum may indicate that the O^+ fragments are not formed in conjunction with molecular D_2.

Table 5.6: Dissociation pathways of D_2O from the C^2A_1 state near 32 eV.

Ion	Relative abundance (%)	KER (eV)	Maximum available energy (eV)
D^+	60	4	13.5 (2-body), 9 (3-body)
O^+	24	3	13.3 (2-body), 9 (3-body)
OD^+	16	5	14

5.2.2 Dissociation of ICN upon Coulomb explosion

Multiply ionized molecules, created upon an initial photoionization involving a core orbital may quickly dissociate into charged and neutral fragments from the rapid loss of binding electrons. The multiple charges, spread over the molecule, may lead to Coulomb repulsion between the moieties, which will result in a fast dissociation called *Coulomb explosion*. The work in Paper III, investigates the dissociation of the triatomic molecule ICN, by multi-electron-multi-ion coincidence spectroscopy, induced by inner-shell (core orbital) photoionization. ICN is a relatively simple, linear, triatomic molecular system, which means that the released kinetic energy for the ionic fragments is mostly along the symmetry axis of the molecule. Therefore, it is an interesting system to investigate the dissociation from high charge systems by Coulomb explosion. Another advantage of a triatomic sample is that the detection of three atomic ions means that no neutral fragments are present after the dissociation process, which simplifies the analysis.

The multi-electron-multi-ion measurements were conducted at several photon energies above the binding energies of single vacancy creation in the core orbitals of ICN; I 4d at 59.2 eV and 60.8 eV, I 4p at 132 eV, I 4s at 194 eV, C 1s at 295 eV, N 1s at 400 eV, I 3d at 632 eV and 643 eV, and I 3p at 885 eV and 940 eV. The mass spectra of ICN measured in coincidence with different core electrons can be seen in Fig. 5.8 and Fig. 5.9. From these figures it is evident that the degree of ionization increase as deeper lying shells are photoionized. As the amount of

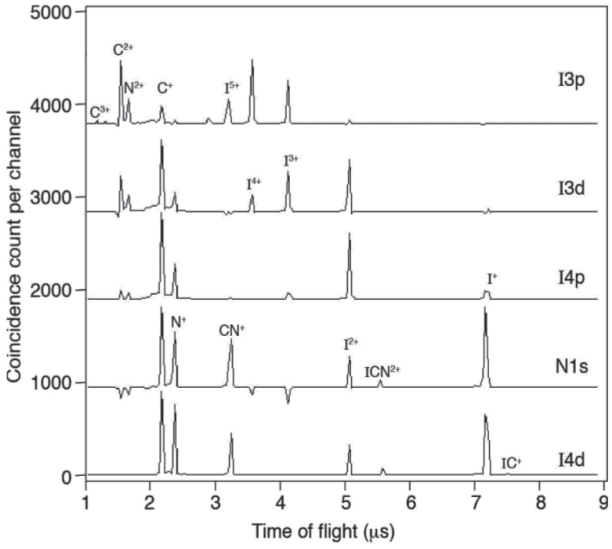

Figure 5.8: Mass spectra of ICN in coincidence with the specific photoelectrons indicated. Accidental and background signal from false coincidences have been subtracted.

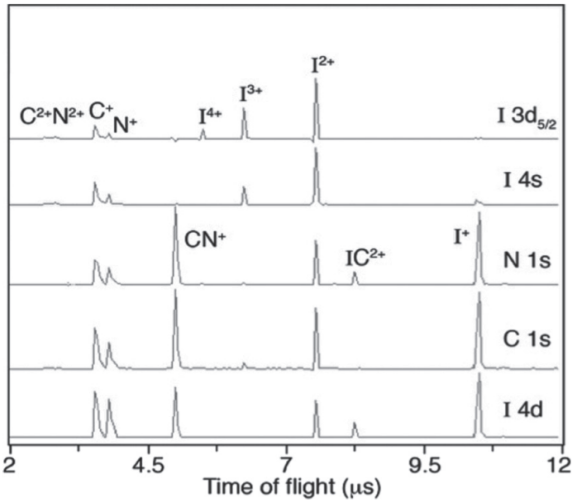

Figure 5.9: Mass spectra of ICN in coincidence with the specific photoelectrons indicated. Accidental and background signal from false coincidences have been subtracted. The measurements in this figure have a comparatively higher sensitivity for heavier ions than in Fig. 5.8.

more highly charged moieties increases, less of the singly charged NC^+ and IC^+ remains in the mass spectra. This is most evident in the mass spectrum obtained in coincidence with the I 4p photoelectron, where the charge build up from Auger cascades becomes the dominant dissociation pathway. The Auger cascade results in the build up of more highly ionized charge states as the molecule dissociates.

When the I 4d shell is ionized only doubly and triply ionized fragments may be formed, as it is above the triple ionization energy at about 55 eV but still below the thermodynamic threshold for total fourfold charged fragments ($I^{2+} + C^+ + N^+$ at 66.2 eV) and the estimated quadruple ionization energy of about 90 eV. From the measurements at photon energies above the I 4d orbital it is possible to extract the energy thresholds and relative intensities for the possible dissociation channels created from the I $4d^{-1}$ ionization, and which are displayed in Table 5.7. The most obvious observation from this data is that the amount of triply ionized fragments are just a few percent of the total decay channels, which may be expected from the small energy difference between the binding energy of the I 4d shell and the triple ionization energy. This means, at this energy, only a few levels of the triply charged ion can be populated by double Auger decay, which decreases the ratio between the amount of double and single Auger decay. The relative intensities for the different channels that are given in Table 5.7 are in line with those produced in double ionization by 48.37 eV photon energy [82]. The threshold values given in the table are for products that are formed with zero kinetic or internal energy. The actual threshold values need to be corrected by at least a minimum kinetic energy

Table 5.7: Relative strengths of decay channels from $4d^{-1}$ ionized ICN.

Channel	Threshold (eV)	Intensity ($\Sigma = 1000$)
ICN^{2+}	29	21
$CN^+ + I^+$	27.8	276
$N^+ + IC^+$	∼30	9
$C + N^+ + I^+$	33	254
$C^+ + N + I^+$	33	354
$C + N + I^{2+}$	35	77
$CN^+ + I^{2+}$	47	18
$C^+ + N^+ + I^+$	47	5
C^+ or $N^+ + I^+$	52	4

that may be estimated, from the data, as about 3.5 eV in the case of two singly charged moieties, and about 7 eV for the case of one doubly and one singly charged moiety.

The ion mass spectra obtained upon C 1s and N 1s photoionization in Fig. 5.9, show a similar degree of ionization as was obtained upon I 4d photoionization, despite the higher ionization energy for the C 1s and N 1s orbitals. The most likely explanation is that extended Auger cascades are not possible from these atoms, but only single, double, and to a small extent triple Auger decay. This is shown to an extent in the measurements presented in Paper IV of this thesis, and further from the measurements in Papers V and VI, where it is shown that double and triple Auger decay have a typical abundance of 10% and 1%, respectively, from C 1s and N 1s photoionization. Further observations from Fig. 5.9 are the effect of charge localization depending on whether the initial vacancy is in the C 1s or on the N 1s shell. A vacancy in the N 1s (or I 4d) shell produces IC^{2+} fragments, which is almost absent in the case of C 1s, suggesting that the I-C bond is most likely to be broken from an initial vacancy on the C atom. Similarly, the I^{3+} ion is formed more strongly after a C 1s vacancy than after a N 1s vacancy, which suggests that the charge transfer is governed by a nearest neighbour effect.

Furthermore, from Figs. 5.8 and 5.9 it is possible to see that as the vacancy is created in deeper shells on the iodine atom, the leading and dominant decay processes are Auger cascades creating predominantly fragments with higher charge states. This can be seen from the almost complete disappearance of the I^+ and CN^+ ions upon photoionization of the I 4p or I 4s shell. The dominant ion fragments upon I $4p^{-1}$ (and also upon I $4s^{-1}$) ionization are fourfold charge states, which can be seen in Table 5.8. From the data in the table it is possible to see that the most abundant channel is the $C^+ + N^+ + I^{2+}$ triple fragment dissociation. One of the main conclusion that can be drawn from the values in Table 5.8 is that the second strongest decay channel is threefold ionization, which contains no neutral atomic or molecular fragments. This is apparent from the relative intensities showing negative

Table 5.8: Relative strengths of decay channels from $4p^{-1}$ ionized ICN.

Channel	Threshold (eV)	Intensity ($\Sigma = 100$)
$C + N^+ + I^+$	33 + KER	-3±6
$C^+ + N + I^+$	33 + KER	3±6
$C^+ + N^+ + I^+$	47 + KER	16±3
$C^+ + N + I^{2+}$	52 + KER	12±20
$C + N^+ + I^{2+}$	52 + KER	-1±3
$C^+ + N^+ + I^{2+}$	67 + KER	61±6
$C^{2+} + N^+ + I^+$	71 + KER	6±1
$C^+ + N^{2+} + I^+$	76 + KER	8±2
$C + N^+ + I^{3+}$	76 + KER	3±4
$C^+ + N + I^{3+}$	76 + KER	3±2

values after the subtraction of false coincidences. The actual energy threshold values in Table 5.8 need to be corrected by at least a minimum kinetic energy, as previously mentioned.

The mass spectra in coincidence with the two I $3d_{5/2}$ and $3d_{3/2}$ orbitals are identical, showing a large production of highly charged atomic fragments. The dissociation processes involving these highly charged fragments lead to high kinetic energy releases in the other fragments, which is evident from the detailed mass spectra for the lower-mass fragments shown in Fig. 5.10. From the width of the

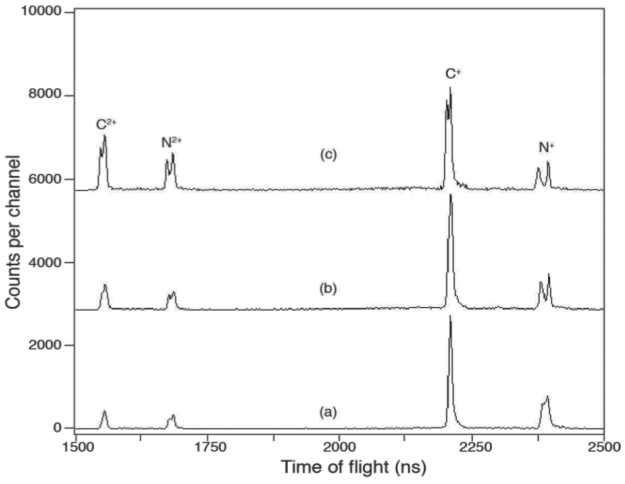

Figure 5.10: Part of the mass spectra of ICN, showing the effect on the peak shape from the high kinetic energies for the lower mass ions. (a) Ions coincident with I^+ at 945 eV, (b) ions coincident with I^{2+} at 945 eV, and (c) ions coincident with I^{4+} at 1200 eV photon energy.

Table 5.9: Apparent relative intensities ($\Sigma = 100$) of ion triples coincident with an I 3d photoelectron.

With	I^+	I^{2+}	I^{3+}	I^{4+}
$C^+ + N^+$	9	42	11	2
$C^{2+} + N^+$	3	2	2	···
$C^+ + N^{2+}$	7	8	9	2
$C^{2+} + N^{2+}$	···	1	2	···

mass peaks in the figure, it is evident that the nitrogen ions have a higher kinetic energy release than the carbon congeners. The mass spectra coincident with the different charge states of the iodine ions show the presence of total initial charge states of the ICN molecule ranging from 3+ to 7+, which is in agreement with the work presented in Ref. [83]. The relative intensities of ion triples of the different charge states can be seen in Table 5.9. From this table it is possible to see that the most abundant charge state is 4+, with fivefold ionization second most abundant, which is characteristically the same as seen for 3d ionization of atomic xenon [83]. From Table 5.9, it is also possible to see that the most abundant light ion pair is $C^+ + N^+$ and the second most being the $C^+ + N^{2+}$. Also, the production of the $C^+ + N^{2+}$ ion pair is found to be stronger than the $C^{2+} + N^+$ production, which most likely is related to the charge separation from the Coulomb repulsion within the ICN molecule.

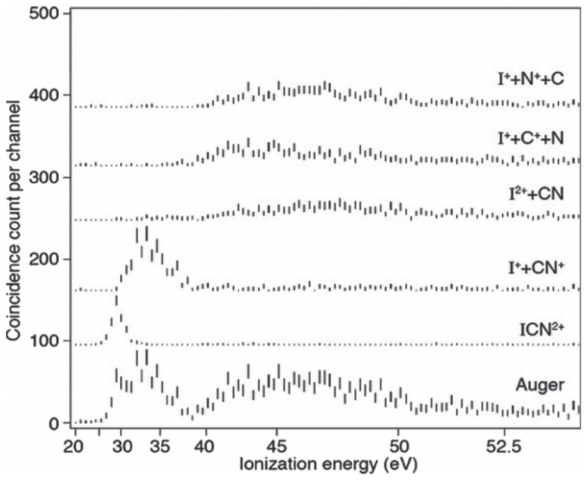

Figure 5.11: Double Auger decay spectra, with partial Auger electron spectra in coincidence with doubly charged ion products following the decay of a I 4d vacancy at 110 eV photon energy.

From the mass spectrum in Fig. 5.8 in coincidence with the 3p photoelectron, an extensive ionization is evident with a large production of very high charge states. The most abundant charge state is the 6-fold ionization, with 7-fold ionization as a close second, and some 8-fold ionization also being present in the mass spectrum. These high charge states have to be produced by Auger cascades as the leading mechanism, involving the 10 4d or 18 n=4 electrons in the atomic iodine orbitals before the delocalized valence electrons get involved. The lowest degree of ionization present in the breakdown of detected triple ions is the 4-fold ionization.

In Fig. 5.11, the double Auger decay spectrum of ICN and the partial Auger spectra in coincidence with doubly charged fragments after I 4d photoionization are shown. The partial Auger spectra show that the most probable decay channel at energies below 40 eV is the production of $I^+ + CN^+$, which is in agreement with the work in Ref. [84]. Above an ionization energy of about 40 eV no molecular ionic fragments are correlated with the Auger spectra. The main products at ionization energies above 40 eV are $I^+ + C^+ + N$, which are formed by the intermediate fragmentation of CN and CN^+ products [84]. The channels forming the $I^+ + N^+$ ion pair are not present in the 40.81 eV photoelectron spectrum [84], which means they are formed by ionization energies above 41 eV. Furthermore, the presence of doubly ionized states in ICN at the low ionization energies means that there are stable non-dissociative dicationic states in the lower energy region of the Auger spectrum.

5.3 Multiple Auger decay in molecules

The dominant consequence of a core vacancy in comparatively light atoms and molecules is known to be the Auger decay mechanism, with the single Auger (SA) decay being often assumed to be the dominant decay channel. The less abundant channel leading to double Auger (DA) decay is also known to exist, but knowledge of its relative abundance is limited to a few cases in atoms where it can be investigated quite easily by mass spectroscopy. In contrast, such investigations are normally not possible in the case of molecules, whose doubly ionized states are often highly dissociative. Earlier works have generally ignored the occurrence of triple ionization through the DA decay process [85–89], on the assumption that it is of negligible abundance. More recent works [90–92] in this area have suggested though that, in at least some specific cases, this may not be the case.

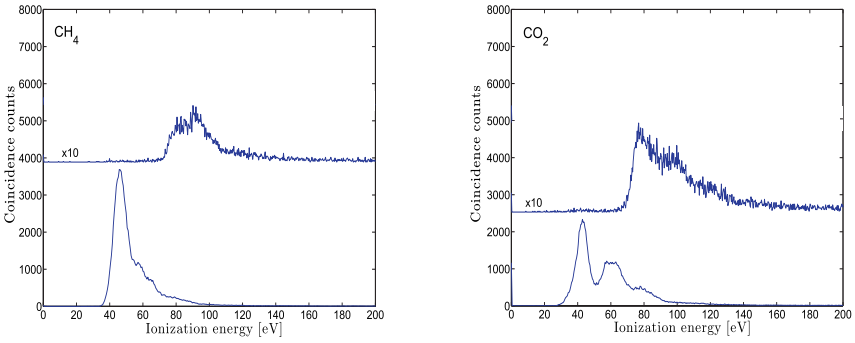

(a) (b)

Figure 5.12: Final state spectra for single (bottom) and double (top) Auger decay of a C 1s vacancy in (a) CH_4 and (b) CO_2, respectively.

Therefore, Paper IV and V were dedicated to investigating the relative abundance of DA decay in molecules. Paper IV is the first systematic study in this area, which focuses on the relative abundance of DA decay compared to SA decay in small molecules containing C, N, and O atoms. Paper V builds further on the results from Paper IV, by a substantially extended investigation covering a large number of molecules containing C, O, F, Si, S, and Cl atoms. The main question considered in these investigations is whether the abundance of DA decay varies as the initial vacancy is created on different atomic sites within a molecular system, or on the same type of atom but in different molecular environments. And, in building on that, Paper VI focuses on the relative abundance of triple Auger (TA) decay in CO and CO_2 after C 1s and O 1s vacancies induced by photoionization. Understanding the relative abundance of double and triple Auger decay is of importance in fields such as plasma physics [93, 94] and astrophysics [95, 96].

5.3.1 Relative extent of double Auger decay in molecules

To begin with, the relative abundance of DA decay was derived from measured single and double Auger spectra of molecules containing C, N, and O atoms. Example Auger spectra of single and DA decay in CH_4 and CO_2 upon the relaxation of a C 1s vacancy can be seen in Figs. 5.12 (a) and (b), respectively. These spectra have previously been measured and interpreted in Refs. [97] and [98]. Thus, in this study we were primarily interested in the amount of coincidence counts in the corresponding spectra. A first interesting and important characteristics that can be noted on the DA decay is that the distributions of energy sharing between the DA electrons are strongly asymmetric, with one fast and one slow electron emitted into the continuum. This can be seen in Fig. 5.13 for three examples of energy sharing of Auger electron pairs in Ne, CH_4, and C_2H_2.

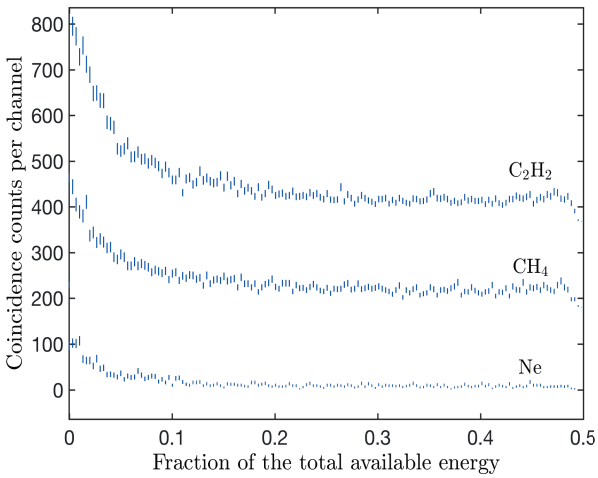

Figure 5.13: Distributions of the energy sharing of double Auger electron pairs initiated by a 1s core vacancy in Ne, CH_4, and C_2H_2.

The inherently low spectral resolution makes a full state-by-state characterization of the possible stepwise Auger decays effectively impossible. It is highly possible that indirect pathways are present in molecular DA processes, just as it does for atoms. However, it is not the purpose of this study to investigate this in detail. In other words, the amount of DA decay obtained in this study will include both direct and indirect pathways, which is the amount that must be taken into account when interpreting, for example, ion pair data from Auger decay.

The relative abundance of DA decay is obtained by taking double and triple ionization data in coincidence with a selected photoelectron from a specific core hole (C 1s, N 1s, O 1s). The DA/(SA + DA) ratios obtained upon C 1s, N 1s, or O 1s photoionization are shown in Table 5.10, as well the ratio obtained for Ne upon Ne 1s photoionization. The amount of DA in Ne is determined as a benchmark

Table 5.10: Relative ratios of overall SA and DA decay following single photoionization of C 1s, N 1s, and O 1s core orbitals.

System	**SA** [%]	**DA** [%]	**Error**[a]
Ne	94.7	5.3	±0.9
Carbon 1s			
CH_4	93.7	6.3	±0.6
C_2H_2	91.8	8.2	±0.8
C_2H_4	91.5	8.5	±0.8
C_2H_6	91.2	8.8	±0.8
CO	90.8	9.2	±0.8
CO_2	85.7	14.3	±1.3
Nitrogen 1s			
N_2	90.6	9.4	±0.9
NH_3	91.8	8.2	±0.8
Oxygen 1s			
O_2	92.9	7.1	±0.7
CO	90.8	9.2	±0.9
CO_2	90.3	9.7	±0.9
H_2O	93.4	6.6	±0.7

[a] Standard error.

in order to relate our findings more easily to previous works. From the tabulated ratios, it can be seen that the relative amount of DA approaches or surpasses 10% for each type of core photoionization. The value obtained for Ne can be compared with the previously obtained value in Ref. [99], of 6% of Ne^{3+} from K^{-1} photoionization, which is in agreement (within the error bars) with the value of 5.3±0.9% obtained in this study. The clearest trend among the molecules is that the larger molecules have a higher ratio of DA to SA decay, which may be attributed to the increasing number of valence electrons that is available for the Auger decay process.

For the time being, a full theoretical quantum mechanical treatment of the abundance of DA in the molecules listed in Table 5.10 is not available. However, the abundance of DA may be understood in first approximation using Fermi's golden rule. All the possible Auger pathways will have partial rates that are proportional to the density of final states available for each specific Auger pathway. The density of final states will in first approximation depend on the number of two- and three-hole configurations of the doubly and triply ionized final states. From this assumption a "zeroth-order" model may be based only on the number of available valence electrons in the molecular system. A first test of this zeroth-order approximation can be seen in Fig. 5.14, where the percentage values for the amount of DA in Table 5.10 are plotted versus the number of valence orbitals, N_{vo} in each molecule. In this figure, the DA percentages have been fitted with a linear line, which shows the general trend of increasing DA decay as the number of valence orbitals increases

in the molecules. While this simplistic approximation may help in estimating the abundance of DA in other molecules, it will most likely not reproduce every detail, which can be seen in the apparent difference of the percentage of DA decay in CO_2 depending on if the initial core vacancy involved the C 1s or O 1s orbital. Therefore, this approximation should primarily be regarded as a motivation for further theoretical quantum chemical investigations on this subject.

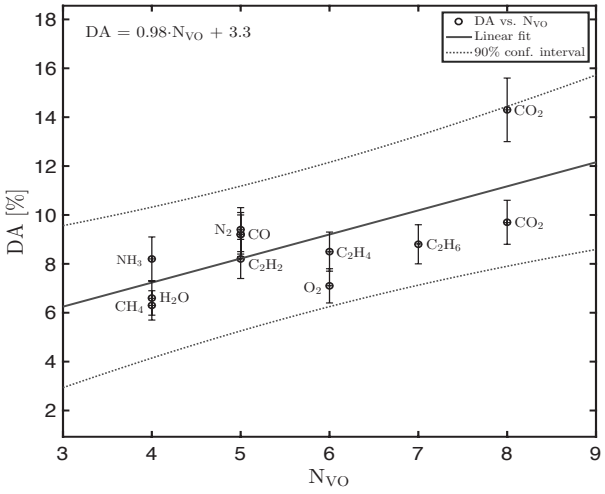

Figure 5.14: Relative abundance of double Auger decay as a function of the number of available valence orbitals for the Auger decay channels. The solid line fitted shows the apparent trend for the series of molecules listed in Table 5.10, with a 90% confidence interval (dashed line).

The work in Paper V builds on the results obtained in Paper IV, by substantially expanding the number of molecular systems investigated as well as by including core vacancy formation in not only 1s, but also 2p orbitals. In this paper the abundance of DA decay upon creation of a single core vacancy in the C 1s, O 1s, F 1s, Si 2p, S 2p, or Cl 2p orbital was studied for a large numbers of molecules. Measurements were done on both Ne and Ar as benchmarks of the experimental method for the determination of the abundance of DA. The new value of 5.7% DA obtained for Ne after 1s photoionization is close to the previous value of 5.3% obtained in Paper IV, and both are in line with the value of 6% of Ne^{3+} obtained in Ref. [99]. The value of 9.0% DA in Ar after 2p photoionization is also in very good agreement with the values of 9.1% and 9.4% obtained in Ref. [101] from photoionization of the Ar $2p_{3/2}$ and $2p_{1/2}$ orbitals, respectively. Furthermore, the value of 9% is in reasonably good agreement with the value of 10% obtained in Ref. [102].

Table 5.11: Percentages of double to single Auger decay in a comparatively large number of molecules, where the number of available valence electrons (N_{ve}) covers a large range (8-56).

System	**DA** [%]	$\mathbf{N_{ve}}$
Ne 1s	5.7 ± 1.7	
Ar 2p	9.0 ± 1.2	
Carbon 1s		
CH_4	6.3[a] ± 0.6	8
C_2H_2	8.2[a] ± 0.8	10
C_2H_4	8.5[a] ± 0.8	12
C_2H_6	8.8[a] ± 0.8	14
CO	9.2[a] ± 0.8	10
CO_2	14.3[a] ± 1.3	16
CH_3Cl	16.5 ± 2.1	20
CF_4	15.8 ± 2.0	32
CS_2	22.8 ± 3.0	32
CCl_4	29.1 ± 3.7	56
Nitrogen 1s		
NH_3	8.2[a] ± 0.8	8
N_2	9.4[a] ± 0.9	10
Oxygen 1s		
H_2O	6.6[a] ± 0.7	8
O_2	7.1[a] ± 0.7	12
CO	9.2[a] ± 0.9	10
CO_2	9.7[a] ± 0.9	16
SO_2	13.7 ± 2.0	26
Fluorine 1s		
CF_4	9.6 ± 1.7	32
SF_6	11.9 ± 2.1	56
Sulphur 2p		
D_2S	8.8 ± 1.1	8
CS_2	12.7 ± 1.6	16
C_4H_4S	13.2 ± 1.7	26
SO_2	16.6 ± 2.1	18
SF_6	23.1 ± 2.9	48
Chlorine 2p		
HCl	9.0 ± 1.1	8
CH_3Cl	10.2 ± 1.3	14
CCl_4	13.5 ± 1.7	32
$SiCl_4$	14.6 ± 1.9	40
Silicon 2p		
$SiCl_4$	18.1 ± 2.3	32

[a] Obtained in our previous study in Paper IV.

The percentages obtained for the abundance of DA in the molecules investigated are listed in Table 5.11, which also includes the previously obtained values from the study in Paper IV. To further test the zeroth-order model introduced in Paper IV, the percentage values in Table 5.11 are plotted in Fig. 5.15 versus the number of valence electrons in the corresponding molecules, similarly as in Fig. 5.14. The main observation from this figure is that the majority of the DA percentage values follows a linear trend, as was expected from the previous study, with a few of the new data points deviating from the trend. This is particularly obvious for the values obtained where the initial core vacancy was created in the F 1s orbital. This means that the zeroth-order model is too simplistic to use as a model of the abundance of DA decay in these molecules, which could be due to several reasons. One reason may come from the inverse energy dependence for the DA decay rate as discussed in the complex analysis by Amusia et al. [15]. The inverse energy dependence can most easily be seen from the difference in the percentage of DA decay in Ne and Ar, where the number of valence electrons are exactly the same for the Ne 1s and Ar 2p core orbitals, but there is considerably more excess energy available in the decay of the Ne 1s vacancy compared to the Ar 2p vacancy. However, a quantitative estimate of the effect that the inverse energy dependence could give rise to is very difficult, mainly because of the continuous energy sharing between the electron pair emitted from the (direct decay channels) in the DA decay process.

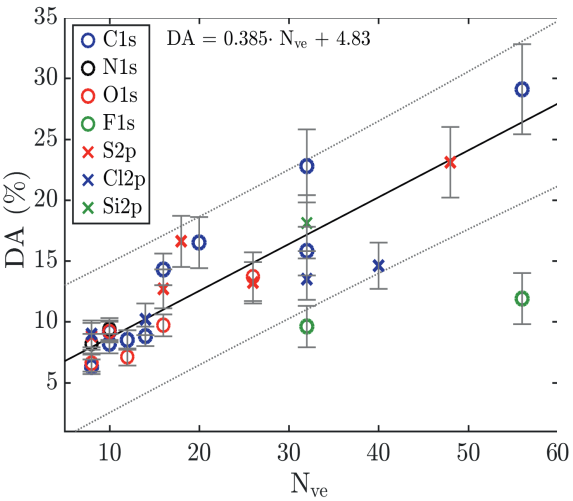

Figure 5.15: Percentage of double Auger decay for the molecules listed in Table 5.11 as a function of the number of valence electrons.

Another factor that may cause the divergence of the data points from the linear trend in Fig. 5.15 is the number of available valence electrons and to what degree they contribute to the Auger decay process. This raises the question if all valence electrons in the molecules are participating in the Auger decay process, or if the contribution of some electrons can possibly be neglected. This question may be

answered by the theoretical work of Wormester et al. [103], where it is suggested for the case of O_2 that the contribution to the Auger process of electrons from the neighbouring oxygen atom decreases as the O-O inter-atomic distance increases, and may even be considered to be negligible at an inter-atomic distance of 2 Å. From these calcuations it appears that the bond distance might be one of the key factors to the (double) Auger decay rate. This is explored in Fig. 5.16, where the percentage of DA decay is plotted as a function of the number of valence electrons on the atom with the initial core vacancy and on the closest neighbouring atoms within an equilibrium distance shorter than 2 Å, akin to the O-O distance where the contributions to the inter-atomic transitions from neighbouring electrons may be neglected [103].

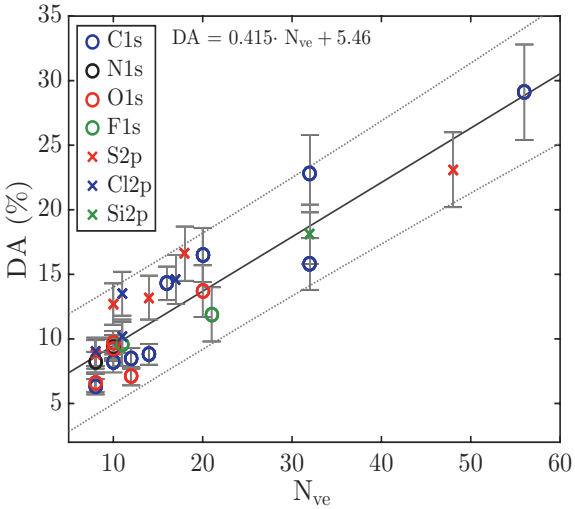

Figure 5.16: Percentage of double Auger decay for the molecules listed in Table 5.11 as a function of the number of closest neighbouring valence electrons.

As can be seen in Fig. 5.16, this aspect improved the zeroth-order model, with the DA percentages now more closely adhering to a linear trend. The fitted linear trend follows the form DA[%] = 0.415·N_{ve} + 5.46, where N_{ve} is the number of valence electrons including the neighbouring electrons on atoms within an inter-atomic distance of 2 Å. This trend may be used as a means to obtain a first estimate for the amount of DA decay in molecules not included in this study. It should, of course, be noted that this model does not include all decay pathways, as it only includes electrons within a 2 Å inter-atomic distance of the initial core vacancy. This distance may for example be too short in conjugated molecules, where the electrons may be strongly delocalized in the valence region. This model anticipates the higher amount of DA decay for initial core vacancies being created at a centrer location in a molecular structure relative to an off-centrer location. As this empirical model can not provide any detailed predictions of the percentage of DA decay in molecules, it should be seen as motivation for new investigations, both in form of quantum

chemical calculations and additional experiments. One interesting observation that can be made from Fig. 5.16 is that the percentage of DA decay upon 1s and 2p core vacancy formation follows the same linear trend, which may indicate that the identity of the initial core vacancy is not a crucial factor for the abundance of DA decay.

5.3.2 Relative extent of triple Auger decay in molecules

Studies on TA decay are even more limited than the case of DA decay, with just a few experimental [104–106] and theoretical [107, 108] investigations on atoms. Estimates of the TA decay rate in atoms can be obtained from ion-mass [102] and multi-electron spectroscopy [104,106], but, to the best of our knowledge, the relative abundance of TA decay in molecules have never been studied before, theoretically or experimentally. Thus, for demonstration, Paper VI focuses on the investigation of the abundance of TA decay (TA/(SA + TA)) in the CO and CO_2 molecules, from measurements of the TA decay spectra obtained in coincidence with the C 1s and O 1s photoelectron, respectively.

The recorded TA decay spectra, after background subtraction, for CO and CO_2 upon C 1s and O 1s photoionization can be seen in Fig. 5.17 and 5.18, respectively. From these spectra it is possible to estimate the onset for quadruple ionization of CO and CO_2 by TA decay upon the removal of a C 1s electron to about 125 eV and 115 eV, respectively. Upon an O 1s core vacancy the onset is estimated to about 105 eV and 95 eV for CO and CO_2, respectively. These onsets are marked in Figs. 5.17 and 5.18 by red arrows. The dissociation mechanism of CO and CO_2 following or leading

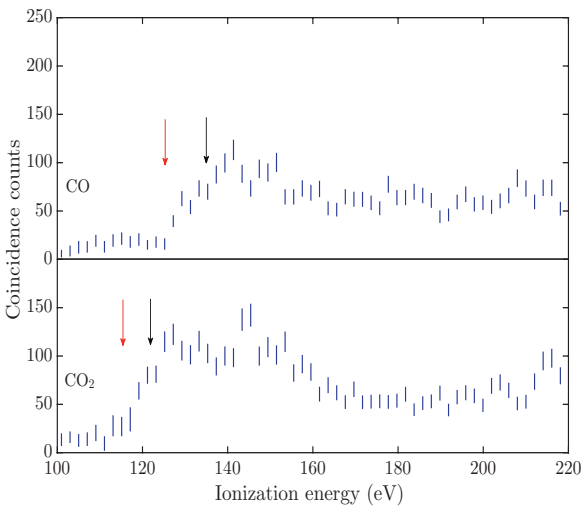

Figure 5.17: Triple Auger electron spectra of CO and CO_2 upon a C 1s core vacancy. The red and black arrows mark the estimated onset and lowest vertical quadruple ionization energies, respectively.

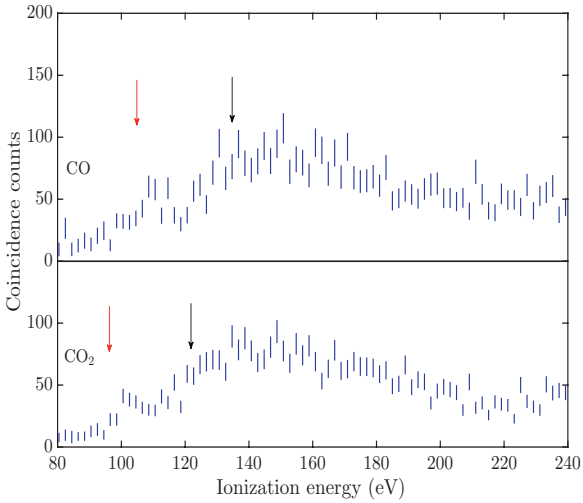

Figure 5.18: Triple Auger electron spectra of CO and CO_2 upon an O 1s core vacancy. The red and black arrows mark the estimated onset and lowest vertical quadruple ionization energies, respectively.

up to quadruply ionized final states have not been investigated in detail, which means that the mechanisms of the direct and indirect decay channels are mostly unknown. Two known dissociation channels in CO upon quadruple ionization are: $CO^{4+} \rightarrow C^{2+} + O^{2+}$ and $CO^{4+} \rightarrow C^{3+} + O^{+}$ [109–111]. The threshold energy for the lowest vertical quadruple ionization for CO can be estimated to about 135 eV from the enthalpy of formation [112, 113] and the KER [109, 111] for theses dissociation channels. Also two dominant dissociation channels are known for quadruply ionized CO_2, namely $CO_2^{4+} \rightarrow C^{2+} + 2O^{+}$ [114] and $CO_2^{4+} \rightarrow CO^{2+} + O^{2+} \rightarrow O^{+} + C^{+} + O^{2+}$ [115]. The threshold energy for the lowest vertical quadruple ionization for CO_2 may be estimated as about 122 eV from the enthalpy of formation [112, 113] and the KER [116] for these dissociation channels. The values for the vertical transitions obtained from these estimates are marked in Figs. 5.17 and 5.18 by black arrows. The conclusions drawn from these values of the vertical transitions are that the values fit reasonably well to the shoulders rising from the onset of TA decay upon C 1s photoionization, whereas the onsets are significantly lower than the estimated values upon O 1s photoionization. Hence, the dissociation channels leading to CO^{4+} and CO_2^{4+} following O 1s photoionization may include a significant number of indirect pathways, with lifetimes greater than a few nanoseconds. In what follows, we shall focus on the total quantity of TA decay in CO and CO_2 from all possible pathways.

Similar to the two previous studies on the relative amount of DA decay, measurements of the Auger decay in Ne and Ar were carried out as benchmarks to previously obtained values. The percentages of DA decay in Ne and Ar upon 1s and 2p photoionization, respectively, are in line with the previously measured values in

Table 5.12: Percentages of double and triple Auger decay compared to the amount of single Auger decay in CO and CO_2. The corresponding percentages for the cases of Ne 1s and Ar 2p ionization are also included.

Sample	**DA** [%]	**TA** [%]
Ne 1s	5.7 ± 0.5	0.38[a] ± 0.05
		0.3[b]
Ar 2p	9.7 ± 0.8	0.4 ± 0.12
		0.35[b]
Carbon 1s		
CO	10.9 ± 1.6	0.82 ± 0.17
	9.2[c] ± 0.8	
CO_2	17.1 ± 2.4	1.44 ± 0.30
	14.3[c] ± 1.3	
Oxygen 1s		
CO	9.4 ± 1.3	0.89 ± 0.19
	9.2[c] ± 0.9	
CO_2	10.5 ± 1.5	1.00 ± 0.21
	9.7[c] ± 0.9	

[a] Values obtained from Ref. [99].
[b] Values obtained from Ref. [117].
[c] Values obtained from Ref. [30].

Paper IV and V. As a further benchmark, the percentage of 0.4% TA decay in Ar was obtained for initial 2p photoionization, which is in good agreement with the value of 0.35% of Ar^{4+} upon 2p ionization that was obtained in Ref. [102].

The values for the relative amount of DA and TA decay obtained in this investigation are listed in Table 5.12. The percentages of TA to SA decay in CO and CO_2 upon C 1s photoionization are 0.82% and 1.44%, respectively, and upon O 1s photoionization the percentages are 0.89% and 1.0%, respectively. Comparing these values to the percentages of DA decay in these molecules suggests that a general tend for the relative Auger decay rates is $1 : 10^{-1} : 10^{-2}$ for SA:DA:TA decay. This finding is larger than what was found in Ref. [105], where Auger decay rates on the order of 1: $10^{-2} : 10^{-4}$ were found for atomic carbon after a 1s core vacancy, which is also supported by the theoretical work of Ref. [107]. This comparatively large difference may not be surprising as the C atom is the smallest system where the production of TA decay upon formation of a K-shell vacancy is possible, and is only about 0.0129% [105].

For a better visualization of the tabulated values, and to see the trend of TA to SA decay, the percentages of the molecules and atoms given in Table 5.12 are plotted in Fig. 5.19 versus the closest neighbouring valence electrons available for the Auger process. The treatment of the data in this way was previously explained in Papers IV and V. Similar to these studies, a linear trend can be seen for the

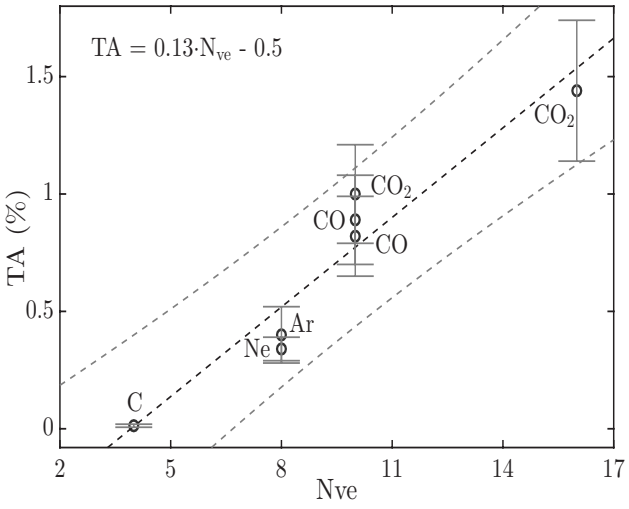

Figure 5.19: Percentage of triple Auger decay for the values in Table 5.12 as a function of the number of closest neighbouring valence electrons.

percentage of TA decay when plotted against the number of nearest neighbouring valence electrons. This linear trend may be used to obtain indicative values of the percentage of TA decay in other atoms and molecules, and is of the form TA[%] = $0.13 \cdot N_{ve}$ - 0.5. An interesting aspect that can be observed is that the value at zero percentage TA decay is at $N_{ve} = 3.8$ that fits well with the fact that the C atom has $N_{ve} = 4$, with a TA percentage value very close to zero. It should, however, be noted that the amount of data on TA decay is still very limited, with many more experimental and theoretical investigations needed to further explore the trend and mechanisms of TA decay in atoms and molecules. From the linear trend in Fig. 5.19, the importance of further investigations can be seen especially for larger molecular systems. The percentage of TA decay may be insignificant for small systems such as the C atom, but according to the linear trend obtained in this study, the percentage of TA decay may be expected to reach a few percent for larger molecules. It may even go up to or surpass 6% for molecular systems with a number of valence electrons of about $N_{ve} = 50$.

Chapter 6

Conclusions and outlook

6.1 Conclusions

This thesis is based on experimental investigations of multi-electron and multi-ion coincidence measurements of samples in the gas phase with a versatile time-of-flight magnetic bottle spectrometer. Investigations on multiply ionized atomic and molecular systems provide valuable information on, and understanding of, the electronic ionization dynamics, electronic structure theory, and dissociation mechanisms of charged systems. In Paper I of this thesis, the magnetic bottle spectrometer was used with a He resonance light source to perform double valence ionisation studies of three methyl halides (CH_3F, CH_3Cl, CH_3I). The double ionization spectra of the methyl halides were interpreted using previous experimental and theoretical works for these systems. From these studies the lowest onset and vertical double ionization energies were obtained, and were used to test an empirical rule-of-thumb for the double ionization of molecules. The conclusion from this investigation is that the intercharge distance may be derived by applying the rule-of-thumb to molecules similar to the methyl halide structure group.

In Paper II of this thesis, the dissociation of heavy water (D_2O) was investigated by photoelectron-photoion coincidence measurements, again using a He resonance line source, with photon energies above the B^2B_2 and C^2A_1 electronic states. These measurements yielded ion mass-selected photoionization spectra and dissociation breakdown diagrams, with improved statistics compared to previous studies. The improved statistics allowed for minor fragments to be detected and the observation of modulations in the yields of the O^+, OD^+, and D^+ ions in the breakdown diagram of the vibrationally resolved B^2B_2 state. These modulations imply that the fragmented system retains some memory of the original vibrational structure before the dissociation pathway is irreversibly chosen. Investigation of the C^2A_1 state revealed high kinetic energy OD^+ fragments in addition to the already known O^+ and D^+ fragments.

Paper III focused on studies performed at the BESSY II synchrotron radiation facility concerning the dissociation mechanisms upon photoionization of deep core orbitals in iodine cyanide (ICN). In this study, the relative strength of the fragmentation channels were obtained upon initial core vacancies produced in the I 4d, I 4p, I 4s, C 1s, N 1s, I 3d, and I 3p core orbitals. The partial Auger spectra were obtained

in coincidence with the doubly charged final products after an initial core vacancy in the I 4d orbital, which reveals the relative extent of the different fragmentation channels in the complete single Auger spectrum of ICN between 25 eV and 55 eV.

Papers IV and V were focused on the relative abundance of double Auger decay in molecules containing first and second row atoms, after core vacancy formation. The investigation in Paper IV found that the relative amount of double to single Auger decay approaches or surpasses 10% in some molecules, which is more than has typically been assumed in the past, and that the amount of double Auger decay from the C 1s, N 1s, or O 1s orbitals follows a linear trend as a function of the number of valence electrons above the core vacancy. These results serve as the foundation for the studies in Paper V, where the relative amount of double to single Auger decay was studied for a large group of molecules upon an initial core vacancy in the C 1s, O 1s, F 1s, Si 2p, S 2p or Cl 2p orbital. The amount of double Auger decay was found to surpass 20% in some of the heavier molecules, which is a significant amount and undoubtedly contradicts the past assumption that such processes are negligible. The linear model for the amount of double Auger decay was improved by correlating the amount of double Auger decay to the number of available valence electrons on the atom with the initial core vacancy and the near neighbouring atoms, which suggests that the inter-atomic distance is one of the main factors determining the amount of double Auger decay in molecules. It was also found that the 1s or 2p nature of the initial core vacancy had no significant effect on the amount of double Auger decay in the molecules studied.

Paper VI investigated the relative amount of triple Auger decay in CO and CO_2 upon C 1s and O 1s photoionization. The ratio of triple Auger to single Auger decay in CO and CO_2 upon an initial C 1s core vacancy was determined as being 0.82% and 1.44%, respectively, and upon a O 1s vacancy to 0.89% and 1.0%, respectively. By comparing these values to previously obtained percentages of triple Auger decay in atoms, it was found that the amount of triple Auger decay also follows a linear trend coupled to the number of available valence electrons, as in the study presented in Paper V.

6.2 Outlook

Multi-electron studies of molecules in the gas phase upon photoionization of valence, inner-valence, and core electrons give insight on the chemical and physical properties of the sample. By way of example, in high-energy environments, including astrophysics, atmospheric physics, and plasma physics, multiply-ionized molecular species are formed at specific rates governed by the electronic structure and dissociation rates of the neutral molecules and highly reactive species created within the environments. By carefully studying these stable and reactive molecular components in the gas phase in the laboratory, an overall physical and chemical picture of high-energy environments may be obtained. Furthermore, experimental studies on molecules are critical for testing quantum chemical models and stimulating their further development. The next step following the studies in this thesis may be to investigate multi-ionization and dissociation processes in highly reactive and

transient molecular species [118], most often found as reactive intermediates in, for example, atmospheric physics [119] and combustion processes [120, 121]. To date, spectroscopy on transient species has been mainly done with (single) photoelectron spectroscopy [118], hence multi-electron and multi-ion coincidence spectroscopy would serve to further build upon the knowledge in this field.

Papers IV, V, and VI demonstrate the possibility to accurately determine the amount of double and triple Auger decay in relatively small molecules containing second and third row atoms. Further, expansion of similar studies on even larger molecular systems, which also contain heavier atoms may be helpful in understanding and interpreting complex deexcitation mechanisms following highly excited systems initiated by intense Free-Electron Laser (FEL) pulses. Investigations of multi-Auger decay processes and their abundance in molecules containing, for example, carbon, nitrogen, oxygen, and sulphur atoms may also improve the understanding of the degree of sample damage in large biomolecular systems exposed to X-rays and other high energy radiation. Radiation damage is a limiting factor in biomolecular imaging with intense X-ray pulses [122], with Auger decay as one of the leading factors causing the damage. By understanding the amount of (multi-) Auger decay and the lifetimes of the core vacancies, which is highly related to the atom with the core vacancy [123] as well as the neighbouring atomic species [124], a more detailed understanding of radiation damage may be achieved. Further theoretical and experimental investigations on double Auger decay in molecules may reveal the main contributing factors, and improve the empirical model presented in Papers IV and V.

Studies of Auger decay rates involving dissociation mechanisms by multi-electron-ion coincidence spectroscopy may reveal how the dissociation mechanisms are connected to the quantity of the different orders of multi-Auger decay processes. In multi-electron-ion coincidence measurements, improved detection-collection efficiency for both electrons and ions would be necessary for effective measurements of multiple electrons and ions in coincidence. Currently, the most limiting factor for the combined detection-collection efficiency is the opening area ratio (OAR) of about 60% for the MCP, which, in turn, limits the detection efficiency. Switching from the standard OAR to a funnel type MCP with a OAR of about 90% [125] should improve the detection efficiency, which would make the data analysis easier potentially obtaining more accurate results. It would also drastically decrease the required acquisition time for the coincidence measurements.

More recent developments in the field of attosecond duration light sources open up the possibility to study the ultrafast (sub-femtosecond) temporal dynamics of electron processes, e.g. tracking the electron motion following the absorption of a photon. Time resolved pump-probe studies using attosecond pulses make it possible to study electron correlations such as relaxation processes of excited atomic and molecular states (see Ref. [126], and refs. therein). This development may open up the possibility to follow the Auger decay process by tracking (in time) intermediate states, as excited atomic or molecular systems relax via, for example, direct or sequential Auger decay processes. The magnetic bottle technique is known to offer,

in principle, the possibility to separate the direct and indirect multi-Auger processes including the determination of their abundances, which may make it a well suited experimental technique for this kind of studies.

Acknowledgements

Five years is a long time, but looking back on my time as a PhD student it does not feel like is has been that long. This is greatly due to the many wonderful colleagues, and new friend I have meet during my time as a PhD student at the University of Gothenburg. First, I would like to give my largest gratitudes to professor Raimund Feifel, for your excellent supervision during these five years of my studies. During the work in your research group, I have learnt more than I can fit into this thesis, but I can also see how much more there is to explore. For all of this knowledge, I would like to thank you once more. I would also like to give my largest gratitudes to professor John H. D. Eland, for all of the valuable knowledge you have given me. It has been a great pleasure working with you during these five years, which has given me more knowledge than I could have imagine, and inspired me to become a better scientist.

I would like to thank the colleagues at the Department of physics at GU, and level 8 of Forskarhuset. I would especially like to thank you for the nice moments during the Friday Fika, and for creating such an inspiring work environment. A few people should have extra thanks for their help during my time at the Department of Physics and for being there a large part of my studies: Ray, Raj, Sergey, Vasyl, Vitali, Jakob, and Dag, it has been a great pleasure working in the same corridor as you. I would also like to thank Jan-Åke Wiman, you have saved me a lot of time by creating simple (but excellent) engineering solutions to the problems I have had in the lab. When it comes to the administrative work concerning my teaching at GU and Chalmers, I would like to thank Jonathan Weidow for his excellent planing skills. I would also like to thank the administrative staff (past and present) at GU physics, especially Bea Transfeld, Maria Siirak, Clara Wilow Sundh, Pernilla Larson, and Marlena Härdelin for all of your help.

I would really like to thank the Helmholtz Zentrum Berlin for the allocation of synchrotron radiation beam time, and the staff of BESSY II for making each beam time a pleasant experience.

Concerning the printed version of the thesis, I would like to thank Raimund, John, Richard, and Måns for helping me to spot all of the mistakes I made during the writing of the thesis. Your comments and suggestions on how to improve the thesis were invaluable.

Now when the acknowledgement is almost to its end, there might be some people that thinks that I have forgotten to mention them. But, I would never forget you guys! I would like to dedicate this part of the acknowledgement to thank the guys that I have been working with daily during the whole or parts of my time as a PhD student. I would like to start with my PhD mirror image, Jonas. Thank you so much for all of the physics related discussions in our office (I will miss them), they are one of the main reasons for my improved physics knowledge today compared to five years ago. I would also like to thank the two guys I already meet during my masters in Uppsala; Dimitris and Richard thank you for the excellent times at and outside the university. Cheers and γεια μας! Omid, I would especially like to thank

you for the time we spent in the lab (damn oven), your company made it much more enjoyable. I will never forget our trips to Berlin and Paris with the lorry, they were interesting (in a good way). I would also like to thank Måns, the newest member to the group, many thanks for reading and spotting the typos and mistakes in the thesis. The main reasons why you all made these five years pass by in no time are because of all the interesting discussions and jokes (yes Richard, even the puns...). I would also like to wish you all a good luck on your new and present adventures.

I have only used the word "thank" in total 16 times so far, but I would like to use it one last time to thank my family. Your support has meant a lot for me, not only during my PhD studies, but also for my five year of undergraduate studies at Uppsala university. Without your support in life, I would not be where I am today.

Andreas Hult Roos

Bibliography

[1] H. Hertz, Ann. der Physik **267**, 983 (1887).

[2] A. Einstein, Ann. der Physik **322**, 132 (1905).

[3] L. de Broglie, Ann. de Physique **3**, 22 (1925).

[4] J. E. Lennard-Jones, Tans. Faraday Soc. **25**, 668 (1929).

[5] K. Siegbahn, et al., *ESCA Applied to Free Molecules*, North Holland, 1969.

[6] Y. Hatano, Y. Katsumura, A. Mozumder, *Charged Particle and Photon Interactions with Matter: Recent Advances, Applications, and Interfaces*, CRC Press, 2010, Ch. 2.

[7] W. Bambynek, et al., Rev. Mod. Phys. **44**, 716 (1972).

[8] B. P. Tsai and J. H. D. Eland, Int. J. Mass Spec. Ion. Phys. **36**, 143 (1980).

[9] R. D. Molloy, A. Danielsson, L. Karlsson, J. H. D. Eland, Chem. Phys. **335**, 49 (2007).

[10] T. Schneider, P. L. Chocian, and J.-M. Rost, Phys. Rev. Lett. **89**, 073002 (2002).

[11] T. Pattard and J. Burgdörfer, Phys. Rev. A **64**, 042720 (2001).

[12] T. Pattard, T. Schneider, and J.-M. Rost, J. Phys. B: At. Mol. Opt. Phys. **36**, L189 (2003).

[13] M. F. Gu, Can. J. Phys. **86**, 675 (2008).

[14] S. Fritzsche, Comp. Phys. Comm. **183**, 1525 (2012).

[15] M. Ya. Amusia, I. S. Lee, V. A. Kilin, Phys. Rev. A **45**, 4576 (1992).

[16] J. Zeng, P. Liu, W. Xiang, J. Yuan, Phys. Rev. A **87**, 033419 (2013).

[17] F. Zhou, Y. Ma, and Y. Qu, Phys. Rev. A **93**, 060501(R) (2016).

[18] P. Liu, J. Zeng, and J. Yuan, J. Phys. B: At. Mol. Opt. Phys. **51**, 075202 (2018).

[19] T. A. Carlson and R. M. White, J. Chem. Phys. **44**, 4510 (1966).

[20] J. H. D. Eland, Mol. Phys. **61**, 725 (1987).

[21] J. A Rice, *Mathematical Statistics and Data Analysis*, Brooks/Cole, Cengage Learning, 2007, 3rd ed.

[22] J. H. D. Eland et al., Phys. Rev. Lett. **90**, 053003 (2003).

[23] G. Beamson, H. Q. Porter, and D. W. Turner, J. Phys. E: Sci. Instrum. **13**, 64 (1980).

[24] J. D. Jackson, *Classical Electrodynamics*, J. Wiley, cop., 2nd edition, 1975.

[25] P. Kruit and F. H. Read, J. Phys. E: Sci. Instrum. **16**, 313 (1983).

[26] J. L. Wiza, Nucl. Instr. and Meth. **162**, 587 (1979).

[27] Hamamatsu, *Photomultiplier Tubes, Basics and Applications*, Hamamatsu Photonics K. K., 2007, 3rd ed. [online] `https://www.hamamatsu.com/resources/pdf/etd/PMT_handbook_v3aE.pdf` [Accessed 8 Apr. 2019].

[28] Hamamatsu, *Electron multipliers*, [online] `https://www.hamamatsu.com/resources/pdf/etd/EMT_TPMH1354E.pdf` [Accessed 21 Feb. 2019].

[29] A. Hult Roos, et al., Scientific Reports **8**, 16405 (2018).

[30] A. Hult Roos et al., Phys. Chem. Chem. Phys. **18**, 25705 (2016).

[31] J. H. D. Eland and R. Feifel, Chem. Phys. **327**, 85-90 (2006).

[32] W. C. Wiley and I. H. McLaren, Rev. Sci. Inst. **26**, 1150-1157 (1955).

[33] A. Hult Roos, J. H. D. Eland, J. Andersson, R. J. Squibb, and R. Feifel, J. Chem. Phys. **149**, 204307 (2018).

[34] J. H. D. Eland, et al., J. Chem. Phys. **145**, 074303 (2016).

[35] A. T. J. B. Eppink and D. H. Parker, Rev. Sci. Inst. **68**, 3477-3484 (1997).

[36] A. S. Giunta, et al., Astrophys. J. **803**, 66 (2015).

[37] P. Choi and M. Favre, Rev. Sci. Instrum. **69**, 3118 (1998).

[38] D. Turnquist, et al., IEEE Trans. Plas. Sci. **8**, 185 (1980).

[39] Behlke, *Product Lines: HV switch, variable on-time, low coupling capacitance, MOSFET*, Product code: HTS-201-40-LC2, [online] `http://www.behlke.com/separations/separation_c3.htm` [Accessed 1 Mar. 2019].

[40] Helmholtz Zentrum Berlin, *Electron Storage Ring BESSY II*, [online] `https://www.helmholtz-berlin.de/quellen/bessy/index_en.html` [Accessed 1 Mar. 2019].

[41] D. T. Attwood, *Soft X-rays and Extreme Ultraviolet Radiation*, Cambridge University Press, 1999.

[42] Beam line UE52-SGM, [online] `https://www.helmholtz-berlin.de/pubbin/igama_output?modus=einzel&sprache=en&gid=1639&typoid=35512` [Accessed 1 Mar. 2019].

[43] P. Miedema, W. Quevedo, M. Fondell, J. large-scale research facilities JLSRF. **2**, A70 (2016).

[44] Beam line U49-2 PGM-1, [online] `https://www.helmholtz-berlin.de/pubbin/igama_output?modus=einzel&sprache=en&gid=1655&typoid=35512` [Accessed 1 Mar. 2019].

[45] Beam line UE56-2 PGM-2, [online] https://www.helmholtz-berlin.de/pubbin/igama_output?modus=einzel&sprache=en&gid=1633&typoid=35512 [Accessed 1 Mar. 2019].

[46] S. Plogmaker, et al., Rev. Sci. Instrum. **83**, 013115 (2012). https://doi.org/10.1063/1.3677329.

[47] O. Edqvist, et al., Phys. Scr. **1**, 25 (1970).

[48] H. Aksela, S. Aksela, and H. Pulkkinen, Phys. Rev. A **30**, 2456 (1984).

[49] A. Kramida, Yu. Ralchenko, J. Reader and NIST ASD Team (2016), [online] http://physics.nist.gov/asd [Accessed 8 Mar. 2019].

[50] V. Schmidt, *Electron Spectrometry of Atoms using Synchrotron Radiation*, Cambridge University Press, 1997.

[51] J. H. D. Eland, Laser Chem. **11**, 259 (1991).

[52] K. Kimura, *Handbook of HeI photoelectron spectra of fundamental organic molecules: ionization energies, ab initio assignments, and valence electron structure for 200 molecules*, Japan Scientific Societies Press, 1981.

[53] C.-M. Liegener, Chem. Phys. Lett. **151**, 83 (1988).

[54] W.E Moddeman, *Auger spectroscopy of simple gaseous molecules*, Dissertation, University of Tennessee. Oak Ridge National Laboratory Report No. ORNL-TM-3013 (1970).

[55] T. Masuoka and I. Koyano, J. Chem. Phys. **95**, 1619 (1991).

[56] R. Feifel et al., Phys. Rev. Lett. **116**, 073001 (2016).

[57] R. P. Grant et al., Int. J. Mass Spec. **192**, 111 (1999).

[58] A. Pilcher-Clayton, J. H. D. Eland, J. Elec. Spec. Rel. Phen. **142**, 313 (2005).

[59] M. Pernpointner, J. P. Zobel, E. Fasshauer, A. N. Sil, Chem. Phys. **407**, 39 (2012).

[60] L. Karlsson et al., Physica Scripta. **16**, 225-234 (1977).

[61] L. Sutton, *Tables of interatomic distances and configuration in molecules and ions*, London: The Chemical Society, Burlington House (1965).

[62] M. I. Al-Jobory and D. W. Turner, J. Chem. Soc. B **0**, 373 (1967).

[63] S. Y. Truonget al., Chem. Phys. **355**, 183 (2009).

[64] H. Lew and I. Heiber, J. Chem. Phys. **58**, 1246 (1973).

[65] P. C. Hariharan and J. C. Pople, Mol. Phys. **27**, 209 (1974).

[66] J. E. Reutt, L. S. Wang, Y. T. Lee, and D. A. Shirley, J. Chem. Phys. **85**, 6928 (1986).

[67] K. Norwood, A. Ali, and C. Y. Ng, J. Chem. Phys. **95**, 8029 (1991).

[68] S. Katsumata and D. R. Lloyd, Chem. Phys. Lett. **45**, 519 (1977).

[69] A. J. Mereret al., Can. J. Phys. **53**, 251 (1975).

[70] B. Ruscicet al., J. Phys. Chem. A **108**, 9979 (2004).

[71] F. Fiquet-Fayard and P. M. Guyon, Mol. Phys. **11**, 17 (1966).

[72] D. Dehareng, Chem. Phys. **110**, 375 (1986).

[73] D. Dehareng et al., J. Chem. Phys. **78**, 1246 (1983).

[74] A. G. Sage, T. A. A. Oliver, R. N. Dixon, and M. Ashfold, Mol. Phys. **108**, 945 (2010).

[75] J. Suárez, L. Méndez, and I. Rabadán, J. Phys. Chem. Lett. **6**, 72 (2015).

[76] L. S. Harbo et al., Phys. Rev. A **89**, 052520 (2014).

[77] K. H. Tan, C. E. Brion, Ph. E. van der Leeuw, and M. J. van der Wiel, Chem. Phys. **29**, 299 (1978).

[78] H. M. Rosenstock, M. B. Wallenstein, A. L. Wahrhaftig, and H. Eyring, Proc. Natl. Acad. Sci. U. S. A. **38**, 667 (1952).

[79] J. H. D. Eland, Chem. Phys. **11**, 41 (1975).

[80] I. Powis and D. J. Reynolds, J. Chem. Soc. Faraday Trans. **87**, 921(1991).

[81] H. Sannet al., Phys. Rev. Lett. **106**, 133001 (2011).

[82] J. H. D. Eland, Chem. Phys. Lett. **203**, 353 (1993).

[83] M. Simon, M. Lavollée, M. Meyer, and P. Morin, J. Chim. Phys. Phys.-Chim. Biol. **90**, 1325 (1993).

[84] J. H. D. Eland and R. Feifel, Chem. Phys. **327**, 85 (2006).

[85] E. Itälä et al., J. Phys. B: At. Mol. Opt. Phys. **46**, 215102 (2013).

[86] D.T. Ha, et al., J. Phys. Chem. A **118**, 1374 (2014).

[87] J. Laksman, et al., J. Phys. Chem. B **118**, 11688 (2014).

[88] D. Céolin, et al., J. Chem. Phys. **123**, 234303 (2005).

[89] E. Itälä et al., J. El. Spec. Rel. Phen. **184**, 119 (2011).

[90] J.H.D. Eland, et al., J. Chem. Phys **132**, 014311 (2010).

[91] S. Zagorodskikh, et al., Chem. Phys **463**, 159 (2015).

[92] J.H.D. Eland et al., J. Chem. Phys. **132**, 104311 (2010).

[93] P. Zimmerer, N. Grün and W. Scheid, Phys. Lett. A **148**, 457 (1990).

[94] S. M. Vinko et al., Phys. Rev. Lett. **104**, 225001 (2010).

[95] D. L. Mitchell et al., Res. Lett. **27**, 1871 (2000).

[96] C. Mendoza, T. R. Kallman, M. A. Bautista and P. Palmeri, A&A **414**, 377 (2004).

[97] J.H.D. Eland et al., Chem. Phys. Lett. **485**, 21 (2010).

[98] J.H.D. Eland et al., J. Chem. Phys. **135**, 134309 (2011).

[99] B. Kanngiesser et al., Phys. Rev. A **62**, 014702 (2000).

[100] T.A. Carlson, W.E. Hunt, and M. O. Krause, Phys. Rev. **151**, 41 (1966).

[101] Lablanquie, P. et al., J. Elec. Spec. Rel. Phen. **156,** 51-57 (2007).

[102] N. Saito and I. H. Suzuki, J. Phys, Soc. Jpn. **66**, 1979 (1997).

[103] Wormeester, H., Borg, H. J. and Silfhout, A. van, Surf. Sci. **258,** 197-209 (1991).

[104] P. Lablanquie, et al., J. Elec. Spec. Rel. Phen. **156**, 51 (2007).

[105] A. Müller, et al., Phys. Rev. Lett. **114**, 013002 (2015).

[106] P. Lablanquie, et al., J. Elec. Spec. Rel. Phen. **220**, 125 (2017).

[107] F. Zhou, Y. Ma, and Y. Qu, Phys. Rev. A **93**, 060501(R) (2016).

[108] P. Liu, J. Zeng, and J. Yuan, J. Phys. B: At. Mol. Opt. Phys. **51**, 075202 (2018).

[109] J. Rajput and C. P. Safvan, Phys. Rev. A **75**, 062709 (2007).

[110] C. Tian and C. R. Vidal, Phys. Rev. A **59**, 1955 (1999).

[111] P. Kumar and N. Sathyamurthy, Pramana-J. Phys **74**, 49 (2010).

[112] B. Ruscic, R. et al., J. Phys. Chem. A **108**, 9979 (2004).

[113] B. Ruscic, J. Phys. Chem. A **119**, 7810 (2015).

[114] C. Wu, et al., J. Chem. Phys. **142**, 124303 (2015).

[115] A. Khan, L. C. Tribedi, D. Misra, Phys. Rev. A **92**, 030701(R) (2015).

[116] E. Wang, et al., Phys. Rev. A **92**, 062713 (2015).

[117] N. Saito and I. H. Suzuki, Phys. Scr. **49**, 80 (1994).

[118] J. M. Dyke et al., Mol. Phys. **40**, 1177 (1974).

[119] J. M. Dyke, *Photoionization of reactive intermediates of importance in the atmosphere*, In: G. Bhowon et al., Ponnadurai (eds.), Chemistry for Sustainable Development, Springer Dordrecht, pp. 34-56, 2012.

[120] R. W. Walker, *Free radicals in combustion chemistry*, Sci. Progress **74**, 163 (1990).

[121] A. C. Baldwin and D. M. Golden, Chem. Phys. Lett. **55**, 350 (1978).

[122] R. Neutze et al., Nature **406**, 752 (2000).

[123] M. O. Krause et al., J. Phys. Chem. Ref. Data **8**, 329 (1979).

[124] E. Kokkonen et al., J. Chem. Phys. **148**, 174301 (2018).

[125] Hamamatsu, *MCP (microchannel plate) and MCP assembly*, [online] `https://www.hamamatsu.com/resources/pdf/etd/MCP_TMCP0002E.pdf` [Accessed 11 Apr. 2019].

[126] F. Calegari et al., J. Phys. B: At. Mol. Opt. Phys. **49**, 062001 (2016).